# Modelling CdTe thin film growth over realistic time scales

by

Miao Yu

A Doctoral Thesis
Submitted in partial fulfillment of the requirements for the award of
Doctor of Philosophy of Loughborough University

April 2015

I would like to dedicate this thesis to my loving parents...

# Acknowledgements

I am heartily thankful to my supervisor, Professor Steven Kenny, whose encouragement, guidance and support from the initial to the final level enabled me to develop an understanding of the subject. I am also thank Professor Roger Smith for his kindly guidance, and Professor Mike Walls and his group for their hard works and kindness of providing experimental results.

I would also like to show my gratitude to my colleagues Chris Scott and Tomas Lazauskas who developed the LKMC codes for the simulations together with me. In addition, Chris also wrote a useful tool, the atomic visualiser, which is used frequently throughout this thesis. And also Sabrina Blackwell and Zainab Al Tooq, for the help getting started with the project.

I want to thank Loughborough University for giving me a place of research and the financial support.

I owe my deepest gratitude to my parents, Dezhu Yu and Xueying Feng, who have supported my studies throughout these years.

b

# Abstract

Cadmium Telluride (CdTe) is an excellent material for low-cost, high efficiency thin-film solar cells and holds the record for watts/cost performance. The laboratory record efficiency of CdTe solar cells lags significantly behind the theoretical maximum for the material. This discrepancy is often attributed to defects such as grain boundaries and dislocations. Thus it is important to do research on how these defects are formed during the growth process.

Atomistic simulations, such as Molecular Dynamics (MD) and on-the-fly Kinetic Monte Carlo (OTF-KMC), are widely used in partnership with experiments in addressing problems in materials science. In this work we use computer simulation to predict the growth of the sputter deposited CdTe thin film.

At the first stage, MD studies of small cluster energetic impacts were carried out by repeatedly depositing $\mathrm{Cd}_x\mathrm{Te}_y$ $(x, y = 0, 1)$ clusters onto different CdTe surfaces with different energies at random positions. The impacts were simulated on Cd- and Te-terminated (100) surfaces and Cd- and Te-terminated (111) surfaces with typical industrial energies varies from 1 to 40 eV at a temperature of 350 K. More than 1,000 simulations have been preformed for each of these cases so as to sample the possible deposition positions and to collect sufficient statistics. The behaviour of deposited clusters under different conditions are studies.

To simulate the process of thin film growth is the next stage in this work. We use different techniques to simulate the growth process on different surfaces. OTF-KMC simulations are performed to simulate the thin film growth process on the (111) CdTe surfaces. Starting with several ad-atoms deposited on the surfaces, in each step, the OTF-KMC method searches for all possible atomic movements (transitions) and randomly selects a transition or deposition to execute based on their corresponding

rates. The thin film grows with more and more clusters to be deposited onto the surface with numerous ad-atom diffusions.

The growth process on the dimerised Te-terminated (100) surface is very interesting. Knowledge of how the Te dimers on the surface split during the growth is gained in the simulations. MD is used to simulate the growth process with an accelerated deposition rate. Several simulations with different deposition energies are performed to see the differences of dissociation of the surface Te dimers. Post-annealing at different temperatures are applied after the growth simulations to find the optimal annealing temperature.

e

# Contents

# List of Figures

# List of Tables

# Chapter 1

# Introduction and Background

Energy consumption is increasing every year. Energy security and supply has become a key problem all around the world. More and more energy is required, while reserves in coal, oil, natural gas and other non-renewable resources become smaller due to human consumption. The usage of traditional non-renewable resources also produces large amount of greenhouse gases, such as $CO_2$ and $N_2O$, which greatly affect the temperature of the Earth. Recent studies show that the concentration of $CO_2$ has increased 40% since the beginning of the Industrial Revolution, and the Earth's average surface temperature rose by $0.74 \pm 0.18$°C over the last century.[1;2] The use of renewable resources, such as sunlight, wind, tides, waves and geothermal heat, are much more environmentally friendly than the conventional non-renewable ones. Governments invest huge amount of money in renewable technologies all around the world. Solar power is one of the most promising renewable energies.

Electricity is one of the most common sources of energy for daily use. Nowadays most electricity is generated by non-renewable sources, such as coal, gas and nuclear. Governments are making efforts in developing renewable electricity generators. In the UK, the renewables share of electricity generation was a record 19.4% in 2014 Q1, up 6.9 percentage points on the share in 2013 Q1[3] and solar photovoltaics (PVs) have an important role to play in this[4].

Solar PVs is now the third most important renewable energy source in terms of globally installed capacity. In 2013, its capacity increased by 38 percent to a running total of 139 GW worldwide[5]. By far, the most prevalent material for solar cells is crystalline silicon (c-Si). But thin film PVs devices have great potential and are a cheaper technology than conventional c-Si based photovoltaic devices[6].

Cadmium Telluride (CdTe) is an excellent material for low-cost, high efficiency thin film solar cells, and it is the only thin film photovoltaic technology to surpass c-Si PVs in the watt/cost measure and have promising efficiency[7;8]. However the laboratory record efficiency of CdTe solar cells lags significantly behind the theoretical maximum for the material. This discrepancy is often attributed to defects such as grain boundaries and intra-grain dislocations[9]. Thus it is important to do research on how these defects are formed during the growth process and therefore reduce them.

## 1.1 Research Goals

In the production of thin film PVs, several thin film layers are applied to a glass base. Most techniques of applying thin films to a surface control layer thickness within a few tens of nanometres[10]. Understanding the thin film growth process is helpful to find proper growth conditions and therefore to reduce the possible defects during the production. The CdTe thin film PVs are the main focus throughout this work.

Thin films are produced by using thin-film deposition techniques to deposit a chosen material onto a substrate or onto previously deposited layers. Different deposition techniques usually lead to different morphology, quality and properties to the produced films. Even for the same deposition technique, the changes of experimental conditions may also resulting in huge differences to the films produced. The aim of this work is to simulate the growth of CdTe thin films under certain conditions and to understand the differences of produced thin films with different conditions, therefore find the proper conditions for producing thin films of better quality.

The goal of this work is achieved in two stages. At the first stage, thousands of single molecule deposition tests are performed by the molecule dynamics (MD) for each condition. The statistical results give the distribution of the deposited molecules' behaviours. This information is helpful when choosing the proper deposition conditions for the long time scale dynamics (LTSD) simulations. At the second stage, we use the on-the-fly kinetic Monte Carlo (OTF-KMC) method, one of the LTSD techniques, to simulate the growth process over realistic time scales.

## 1.2 CdTe Thin Film Photovoltaics

The thin film solar cells, also called the thin film photovoltaic (PV) cells, are the second generation solar cells. They are made by depositing multiple thin layers, or thin films of PV material onto a substrate. The film thickness varies from a few nanometres to tens of micrometers. Comparing to the first generation solar cells, which are made of crystalline silicon (c-Si), the thin film technologies reduce the amount of active material in a cell.[11]

Figure 1.1 shows the best research cell efficiencies over years. The efficiency of thin film PVs significantly improved over the years, but are still less efficient than conventional c-Si based solar cells. The CdTe thin film PV is the only thin film PV technology to surpass c-Si solar cells in the watt/cost measure and have promising efficiency[7;8]. The CdTe thin film PVs have great potential and plenty of researchers are working on it. In the laboratory, the cell efficiency for CdTe thin film PVs reaches a record of 21 percent in 2014[13], which is not very far from the records of mono c-Si cells ($\sim$25%)[14] but still a third way to the theoretical limit for all single-junction solar cells ($\sim$34%)[15].

Throughout this work, the material we focus on is the CdTe. As stated, the CdTe thin film PVs have great potential and are cheaper than c-Si solar cells. CdTe is the predominant thin film technology, with 5 % of worldwide PV production, and accounts for more than half of the thin film market[14].

Figure 1.2 illustrates the structure of a CdTe thin film solar cell. The substrate is glass, with an optional anti-reflective (AR) coating in the front. The CdTe thin film solar cell consists of multiple layers or thin films, the front contact - layer of transparent conducting oxide (TCO), the window layer - layer of CdS, the absorber - layer of CdTe, and the back contact - layer of buffer and metal. The thickest and the most important layer is the CdTe layer.

In the laboratory, to get the optimal conditions for producing the CdTe thin film cells, the quality of the produced CdTe layers need to be examined. In materials science, transmission electron microscopy (TEM) is a widely used technique for analysing the quality of produced thin film solar cells. The TEM images have significantly higher resolution than light microscopy images. They are capable to examine details of the materials in atomic scales, such as voids, grain boundaries and even stacking faults. Figure 1.3 shows the TEM image of a CdTe thin film solar cell sample. Figure 1.4 shows high resolution TEM images of stacking faults

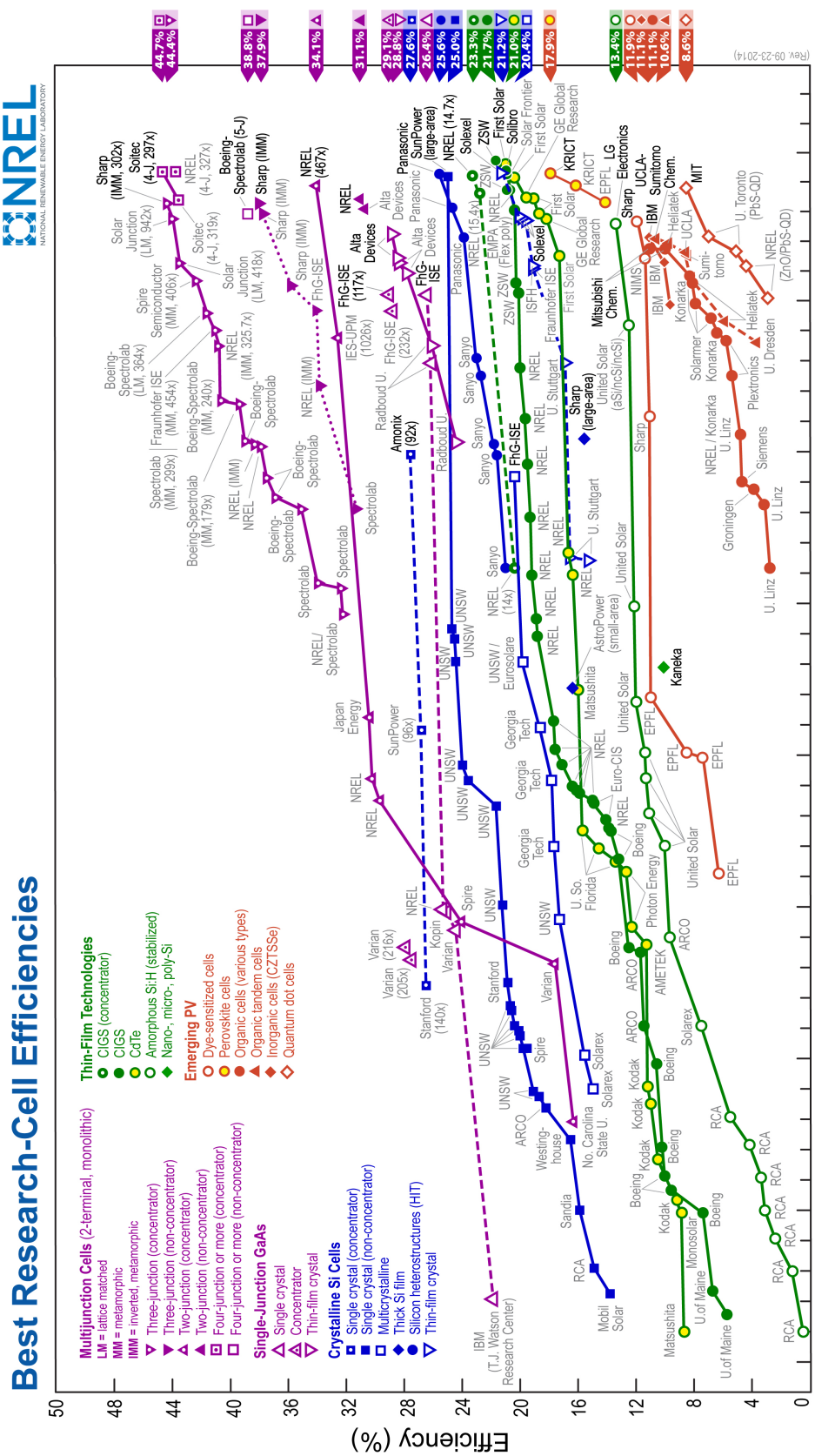


**Figure 1.1:** Chart of research cell efficiency records over years. Blue curves represent efficiency records of c-Si cells, and green curves the efficiency records of thin-film technologies. Yellow dots with green boundaries represent for the efficiency records of the CdTe thin film cells. The efficiencies improved over the years, but thin-film PVs are still less efficient than c-Si cells. Chart taken from [12]. See Appendix A for a large print of this chart.

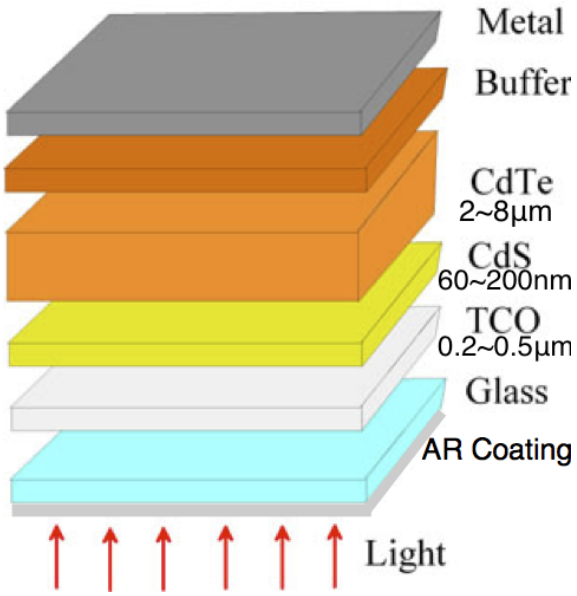


**Figure 1.2:** Illustration of a CdTe thin film solar cell structure. The graph is modified based on the one taken from [16]. Thickness data from [17].

in CdTe thin films.

## 1.3 Experimental Techniques

The action of applying thin films onto a substrate or onto previously deposited layers is called thin-film deposition. There are two broad categories for the deposition techniques: the chemical deposition and the physical deposition.

The thin films are generated through a series of chemical reactions. Usually the final material of the desired thin films is generated by series of chemical reactions from other raw materials. There are various chemical deposition techniques, currently two groups of techniques dominate the field. The first group includes chemical vapour deposition (CVD) and atomic layer deposition (ALD). These techniques use a gas phase to transport the material to the substrate in a vacuum environment. The raw materials are vaporised via thermal conversion and react with other volatile chemicals or reactive gases such as oxygen or hydrogen [20;21;22]. The other group of techniques is called chemical solution deposition (CSD) or sol-gel processing. These techniques use a liquid phase as the transfer media. The main difference from the first group of techniques is that the chemical transformations are in solution and

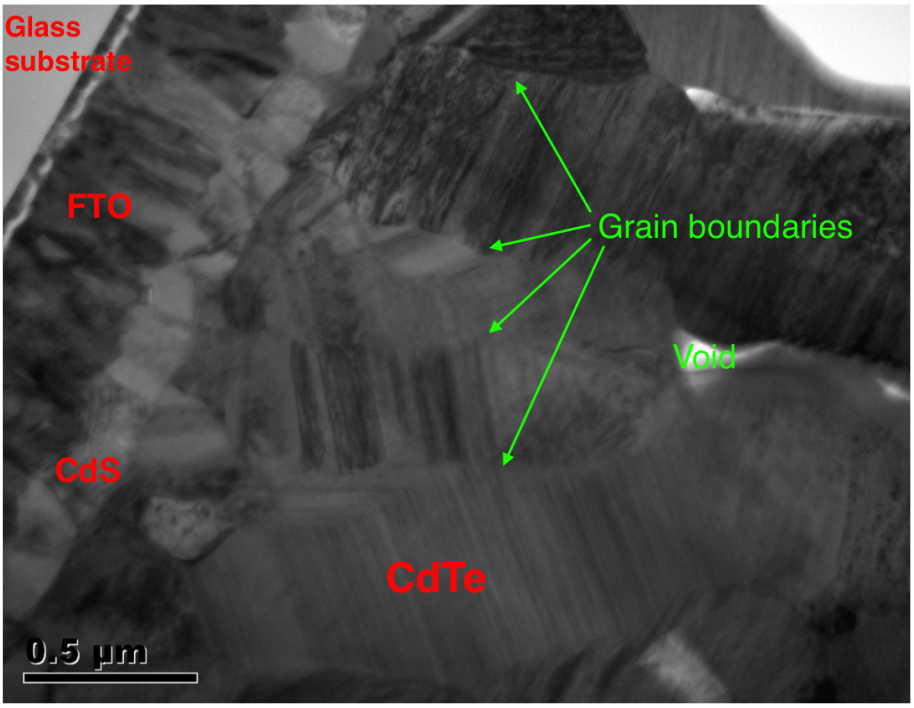


**Figure 1.3:** A TEM image of a CdTe thin film solar cell sample. The image captures the main structure of a thin film solar cell. From the top left to the bottom right, the materials of the layers are: the glass substrate, the layer of fluorine doped tin oxide (FTO) as the transparent conducting oxide (TCO), the layer of CdS as the window layer and the layer of CdTe as the absorber. The texture of the CdTe layer is captured in the image, further more, defects, such as voids and grain boundaries, are also captured. Image provided by CREST in Loughborough University.[18]

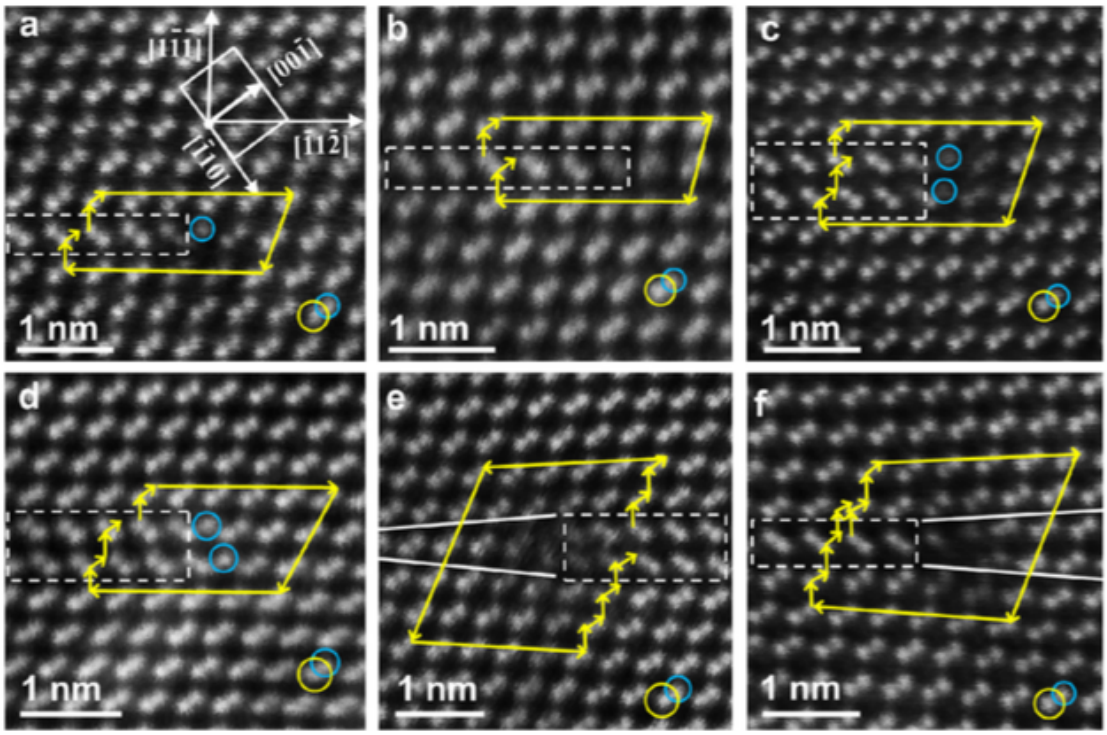


**Figure 1.4:** High resolution TEM images of stacking faults in CdTe thin films. Images capture different configurations of partial dislocations (stacking faults). The white lines show there is an interstitial plane and a vacancy plane on each stacking fault. The small blue and big yellow circles indicate Cd and Te columns, respectively. The white dashed boxes indicate the stacking faults. The yellow arrows mark the Burgers circuits. All the figures are aligned in the same coordinate system shown in (a). Image is taken from [19].

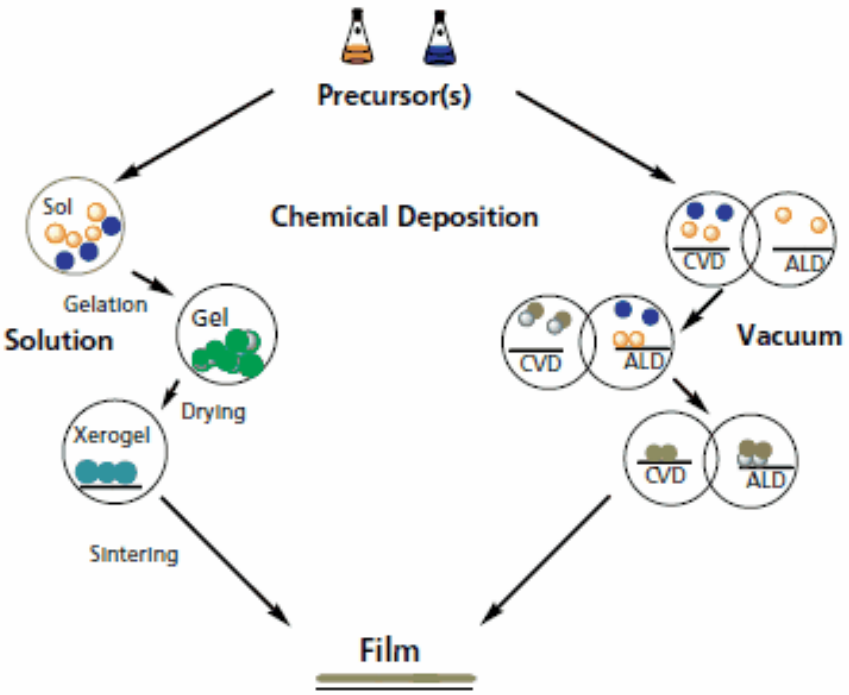


**Figure 1.5:** Schematic illustrating chemical deposition. Left hand side shows the chemical solution deposition (CSD) techniques, while right hand side shows the chemical vapour deposition (CVD) and atomic layer deposition (ALD) techniques. "Sol" and "gel" in the CSD processing represent for "solvent" and "gelation", respectively. Figure is taken from [27].

solid-state. They include formation of colloidal suspension in an appropriate solvent (sol), gelation (gel), evaporation of the solvent (drying), and thermal treatment (sintering) [23;24;25;26]. Figure 1.5 shows two groups of chemical deposition process.

The CVD can be used to produce CdTe thin films. The thin films are grown in a vacuum container filled with gas phase raw materials, which typically are mixes of Cd gas and Te gas. Chemical reactions mainly occur on the surface of the substrate, where the CdTe thin film grows. One advantage of using CVD to produce CdTe thin films is that we can control the ratio of Cd and Te of the source material by controlling the pressure of source gases. Another advantage is that it is easy to add dopant into the film by simply adding the gas phase dopant into the reaction container. Illustration of a typical CVD reactor is shown in Figure 1.6.

Physical deposition uses physical transformations of materials, for example mechanical, electromechanical or thermodynamic means, to produce thin films. The final material of the desired thin films is the same as the raw material. Most physical

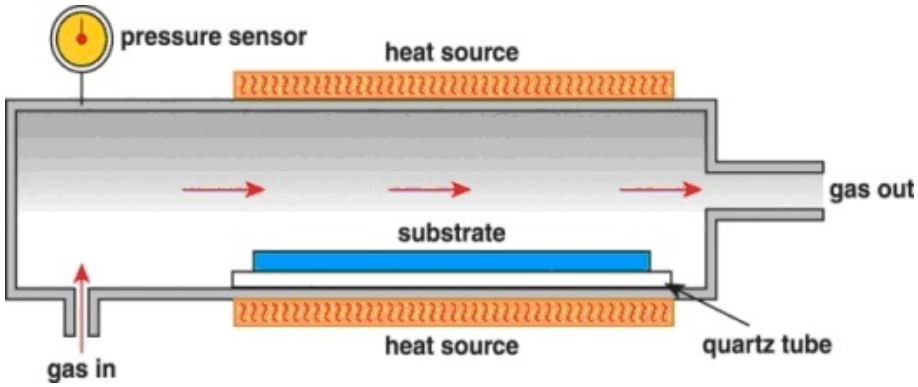


**Figure 1.6:** Illustration of a typical CVD reactor. Figure is taken from [28].

deposition techniques use a vapour phase to transport the material onto substrate, so that they are classified as physical vapour deposition (PVD). Similarly to CVD, PVD is also taken place within a vacuum chamber. There are two main categories for the PVD techniques, evaporation and sputtering. Evaporation usually requires high temperature to vaporise the material by either thermal the entire material (evaporative deposition), closed space sublimation (CSS) [29] for example, or use electron beam (EBPVD) or pulsed laser (PLD) to boil a small spot of material [30;31;32]. Sputtering relies on a plasma, some energetic particles, to knock a target of material that is to be deposited. Since there is no evaporation, the temperature is relatively low and the sputtering technique is very flexible. The plasma used to knock target material can be a noble gas or ion-beam [33;34]. Sputtering is a fast technique and provides good control on the thickness, thus widely used.

CSS is an evaporative deposition technique. Many scientists use CSS to produce CdTe thin films due to its high growth rate. The growth process is taken place within a vacuum chamber. The CdTe source material is heated at a very high temperature, and they sublimate into gaseous state. The vaporised CdTe condense on the substrate surface, allowing the CdTe thin film to growth. Figure 1.7 illustrates a CSS deposition system.

Magnetron sputtering deposition [36;37;38] is also widely used for CdTe thin film production. Unlike the CSS, magnetron sputtering deposition does not require high temperature to sublimate the source material. Instead, it uses accelerated $Ar^+$ atoms to hit the CdTe source material, therefore Cd or Te atoms would be sputtered from the target and then deposit onto the substrate surface. A sketch of magnetron

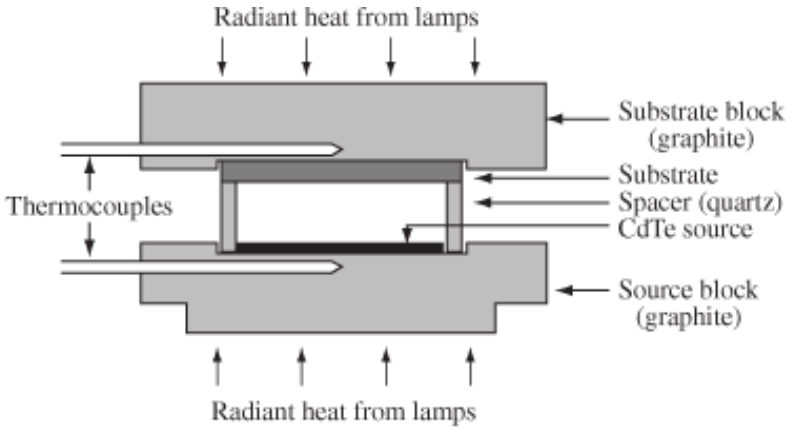


**Figure 1.7:** Illustration of a closed space sublimation deposition system. Figure is taken from[35].

sputtering process is shown in Figure 1.8.

In this work we focus on modelling the growth of thin films via PVD, particularly magnetron sputtering.

## 1.4 Simulation Techniques

In materials sciences, scientists usually use atomic simulations to verify or predict experimental results. There are varies of techniques. Each method has its own applications and limitations. A sketch of time scale versus lattice size for different techniques is shown in Figure 1.9.

*Ab initio* or density functional theory (DFT) method has been very popular for atomic simulations since the 1970s. In most cases, the results of DFT calculations for solid-state systems agree with experimental data quite well. However, the computational costs are relatively high compare to other atomic simulation methods. Therefore we can only afford to simulate for a very small system with a short simulation time.

Molecular dynamics (MD) was originally developed in the 1950s and it is widely applied nowadays in materials science. The MD simulates the trajectories of atoms by solving the Newton's equations of motion for a system. In the system, the forces and potential energies are described by molecular mechanics force fields. In the MD method, the time is increased by a time step (usually 1 femtosecond). Due to the complexity of computing integrals, the system size is limited to hundreds

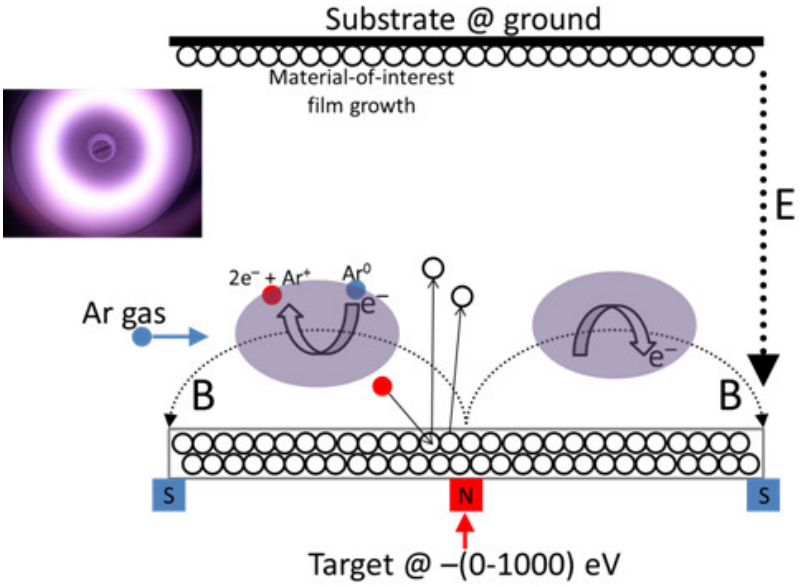


**Figure 1.8:** Sketch of magnetron sputtering deposition. Figure is taken from [39]

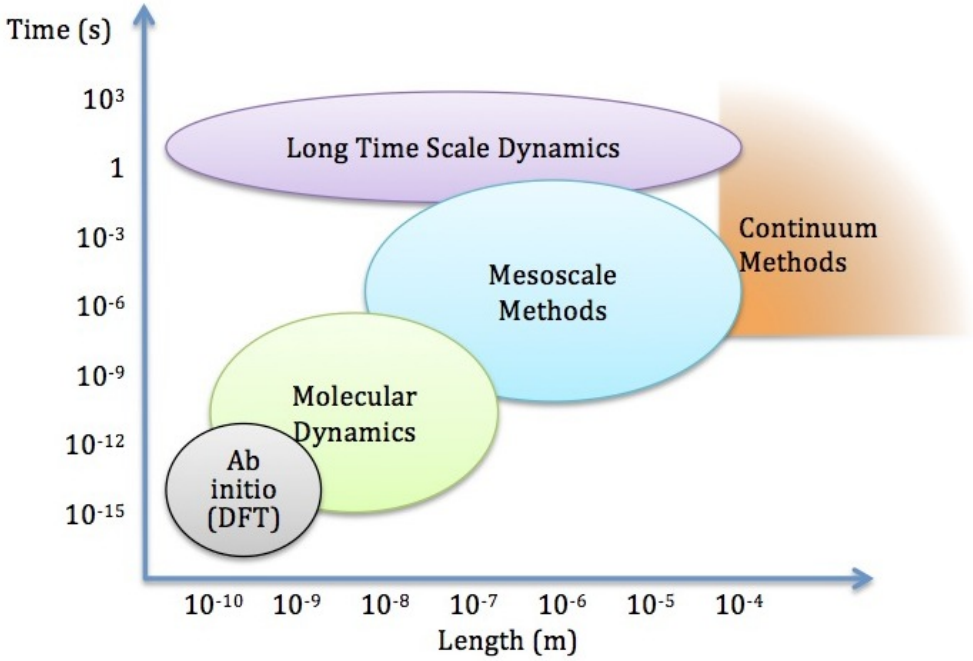


**Figure 1.9:** The attainable simulation time and lattice sizes for different techniques.

of thousands of atoms. And it is very hard to reach nanoseconds even for a small system.

Many interesting process occurs on time scale of seconds or even longer. To extend the time scale of the atomic simulations, new methodologies are developed, such as mesoscale methods, continuum methods and long time scale dynamics (LTSD). All these methods extend either the size of system or attainable time or both in various ways. For example, in the simulations for polymers, the mesocale method regards a group of atoms (polymer) as one object while calculating the interatomic forces. Another example is the kinetic Monte Carlo (KMC) method, one of the LTSD methods, which ignores the atomic vibrations within a potential basin and only simulates hoppings between potential basins (e.g. diffusions).

In this work, we use the combination of the MD and the LSTD method to simulate the growth of CdTe thin films.

## 1.5 Software Implementation and Development

We use a combination of MD and on-the-fly KMC (OTF-KMC) to simulate the CdTe thin film growth. The MD code we are using in this work is the LAMMPS package (Large-scale Atomic/Molecular Massively Parallel Simulator[40;41]), an open source code using classical MD.

The OTF-KMC technique was initially introduced by L. Vernon[42]. The OTF-KMC techniques used in this work are developed in collaboration with colleagues C. Scott and T. Lazauskas from Loughborough University's materials modelling group. The method is initially developed to work with the LboMD (Loughborough Molecular Dynamics) package. In this work, the method is extended to work with LAMMPS, and a few new features are added.

At the beginning of my PhD, the decision was mad to completely rewrite the OTF-KMC code used at Loughborough University. The drivers for doing this included improving the parallel efficiency of the code, making better reuse of commonly employed techniques and re-engineering the code to better enable new features to be added. I undertook this task along with my co-workers C. Scott and T. Lazauskas. The work started with designing the framework for the code so as to engineer a robust, scalable code that could have new techniques easily added to it. The code is written in Python, utilising "multiprocessing" module (part of the Python standard

library) for parallelisation to enable use on high performance computing systems with embedded C libraries for the computationally demanding parts of the code.

In addition to contributing generally to the code, I led on a number of specific projects. Firstly I implemented a methodology to link LAMMPS to our OTF-KMC code to enable the potential for my project to be used. My main contribution was the development of the superbasin method, see Chapter 6, in the code. This was a substantial undertaking and involved circa six months worth of work on my part. The first stage of this project was to develop a superbasin algorithm suitable for our OTF-KMC approach. I then translated this into a coding framework to efficiently implement this method. This was followed by the actual coding of the algorithm along with the subsequent testing and debugging. This development allows for relevant time scales to be reached in my simulations and is now being employed by four other members of the group.

## 1.6 Thesis Layout

Chapter 2, the first methodology chapter, introduces the MD method, with descriptions of interatomic potentials. In this chapter, the boundary conditions, thermalisation and system relaxation are also discussed. An efficient tool to visualise the simulation results is also introduced.

Chapter 3, the second methodology chapter, introduces the OTF-KMC method, which is one of the LTSD methods. Saddle finding methods and reuse of transitions, which are used in the OTF-KMC method, are also discussed in this chapter.

Chapter 4 introduces the Cadmium Telluride lattice, including lattice structure, properties and defects.

Chapter 5, the first result chapter, introduces the energetic impact simulations of $Cd_xTe_y$ clusters on the CdTe surfaces using the MD. This chapter discusses the behaviour of deposited clusters after impact at different conditions. The information gained from this chapter is helpful for choosing the right condition for a thin film growth simulation.

Chapter 6 introduces a superbasin method, which speeds up the OTF-KMC by considering several potential basins connected by low barriers as a single superbasin object. The superbasin method can speed up the CdTe thin film growth simulations by at least two orders of magnitude.

Chapter 7, the second result chapter, discusses the results of simulations for the CdTe thin film growth. We use OTF-KMC with superbasin methods to simulate the (111) CdTe thin film growth, and use MD with accelerated deposition rate to simulate the CdTe thin film growth on the (100) dimerised Te-terminated surfaces. Different growth mechanisms are observed on different type of CdTe surfaces.

Chapter 8 is the final chapter. It draws the conclusions of this work and suggestions for the potential future studies.

# Chapter 2

# Methodology I: Molecular Dynamics

## 2.1 Introduction

In material science, atomistic simulation is widely used as an outstanding partner with experiment in addressing problems. Molecular Dynamics (MD) is one of these atomistic simulation techniques. By changing the parameters in the simulations, we can simulate different experiments, e.g. magnetron sputtering[43] and close space sublimation[44] for producing thin film cells. We use computer simulations to gain knowledge and predict experimental results.

In the MD method, an appropriate interatomic potential is chosen to describe the atomic forces. The interatomic potentials will be introduced later in Section 2.2. Then the motions of atoms can be simulated by solving Newton's equations of motion.

$$\mathbf{F} = m \cdot \mathbf{a} \qquad \mathbf{F} = -\frac{\partial E}{\partial \mathbf{r}} \tag{2.1}$$

where $\mathbf{F}$ is the force acting on atoms, $m$ is the mass, $\mathbf{a}$ is the acceleration, $E$ is the potential energy and $\mathbf{r}$ is the system configuration.

One can model the dynamics by integrating the equations of motion numerically with a chosen small time step $\Delta t$. We use the Velocity Verlet algorithm[45] to integrate time in MD, because of its straightforward nature. By employing Taylor expansion to $\mathbf{r}(t + \Delta t)$, $\mathbf{v}(t + \Delta t)$ and $\mathbf{a}(t + \Delta t)$, respectively, and combining them,

the new configuration and velocity are then given by

$$\mathbf{r}(t+\Delta t) = \mathbf{r}(t) + \mathbf{v}(t)\Delta t + \frac{1}{2}\mathbf{a}(t)\Delta t^2 + O(\Delta t^3) \tag{2.2}$$

$$\mathbf{v}(t+\Delta t) = \mathbf{v}(t) + \frac{1}{2}\left[\mathbf{a}(t+\Delta t) + \mathbf{a}(t)\right]\Delta t + O(\Delta t^2) \tag{2.3}$$

where $\mathbf{v} = \dot{\mathbf{r}}$ is the velocity and $\mathbf{a} = \ddot{\mathbf{r}}$ is the acceleration.

MD follows the actual dynamical evolution of the system. The technique has been able to model many interesting processes, such as sputtering[46], crack propagation[47] and nanoindentation[48]. Resolving individual atomic vibrations requires a time step of the order of femtoseconds (fs) to integrate of the equations of motion.

The most difficult and complex part in the MD is to choose a right interatomic potential for force evaluations. In this work, the only potential we are using throughout the work is the analytical bond-order potential for CdTe binary system which is introduced in Section 2.2.3. Due to the difficulty and complexity of implementing new potentials into an MD code, I did not write an implementation of this potential. Instead, we use an open source MD code using classical MD, the LAMMPS package (Large-scale Atomic/Molecular Massively Parallel Simulator[40;41]), which already include the bond-order potentials.

## 2.2 Interatomic Potentials

In the MD simulation, we need to choose the right potential function to describe the interatomic interactions.

The most accurate force calculations are *ab initio*[49], which uses the knowledge of methods such as density functional theory (DFT). However, the *ab initio* calculations, such as DFT calculations, are so computationally expensive that we cannot afford to use them for the simulations throughout this work. The *ab initio* modelling, however, can be used for parametrisation of empirical potential function.

Traditionally the potential function is derived by fixing an analytical functional form and then using experimental data to parametrise the function. Generally, the energy of $N$ interacting particles can be resolved into one-body, two-body, three-

body, etc. contributions as follows:

$$E = \sum_i V_1(i) + \sum_{\substack{i,j \\ i<j}} V_2(i,j) + \sum_{\substack{i,j,k \\ i<j<k}} V_3(i,j,k) + \cdots + V_N(1,\ldots,N) \tag{2.4}$$

where $V_m$ is an "$m$-body potential" and $V_m$ converge quickly to zero with increasing $m$. In this expansion, the first term that describes the interactions of particles is the second (two-body) term. Thus $V_1$ term is absent from the interatomic potential functions.

The pair potential is the simplest form of such traditional potential. The total energy $E$ is the sum of site energy $E_i$ for atom $i$ over all $i$, where $E_i$ is given by the sum of bond energy $V(i,j)$ over all pairs of $i$ and $j$.

$$E = \sum_i E_i = \frac{1}{2} \sum_i \sum_{j \neq i} V(i,j) \tag{2.5}$$

Pair potentials are widely used due to their simplicity. They are easy to implement and quick to parametrise. The famous Lennard-Jones (LJ) potential is a simple model to approximate the interactions between a pair of atoms or molecules. However, for many interesting materials such as semiconductors, polymers and some metals, the pair potentials are not satisfactory to provide the full range of interactions.

### 2.2.1 Stillinger-Weber Potential

The Stillinger-Weber (SW) potential was developed by F. H. Stillinger and T. A. Weber in 1985 [50]. In addition of the pair potentials, $V_2(i,j)$, the SW potentials [50] also take the triplet potentials, $V_3(i,j,k)$, into account:

$$E = \sum_i \sum_{j>i} V_2(i,j) + \sum_i \sum_{j \neq i} \sum_{k>j} V_3(i,j,k) \tag{2.6}$$

where the pair and triplet potentials are given by

$$V_2(i,j) = \begin{cases} A(Br_{ij}^{-p} - r_{ij}^{-q}) \exp[(r_{ij}-a)^{-1}] & , r < a \\ 0 & , r \geq a \end{cases} \tag{2.7}$$

$$V_3(i,j,k) = h(r_{ij}, r_{ik}, \theta_{jik}) + h(r_{ji}, r_{jk}, \theta_{ijk}) + h(r_{ki}, r_{kj}, \theta_{ikj}) \tag{2.8}$$

$$h(r_{ij}, r_{ik}, \theta_{jik}) = \lambda \exp[\gamma(r_{ij}-a)^{-1} + \gamma(r_{ik}-a)^{-1}] \times (\cos\theta_{ijk} + 1/3)^2 \tag{2.9}$$

where $r_{ij}$ is the distance between atoms $i$ and $j$, $\theta_{ijk}$ is the angle between $r_{ji}$ and $r_{jk}$ and $a$ is the cut-off, together with $A$, $B$, $q$, $p$, $\lambda$ and $\gamma$ are parameters to be determined.

Obviously, SW potential is a potential that contains both two- and three-body components. The two-body potentials only consider the distance between atoms. It is not enough to accurately describe the geometry of the system. By introducing the three-body terms $V_3$ and also consider the angles among three atoms, the cosine term in Equation 2.9, the SW potential is able to distinguish pairs of bonds emanating from vertex $j$ with the desired geometry. In other words, if we think of two-body potentials as describing pairs of atoms in one dimension, with the help of three-body terms, the SW potentials are able to describe the geometry of atoms in three dimensions.

The SW potentials are still not adequate for accurately describing the cohesive energy over a wide range of bonding geometry and coordination[51] despite taking both pair and triplet potentials in consideration. However inclusion of four- or five-body terms may cause far too many free parameters.

### 2.2.2 Tersoff Potential

Rather than taking more many-body terms into account, J. Tersoff introduced the Tersoff (TR) potential in 1988[52;53]. The TR potential uses the bond-order to describe pair potentials. In this model, the bond-order (i.e. the strength of each bond) depends upon the local environment. The more neighbours an atom has, the weaker bonds it forms.

The TR potential is taken to have the form of Equation 2.5, where

$$V(r_{ij}) = f_C(r_{ij}) \left[a_{ij} f_R(r_{ij}) + b_{ij} f_A(r_{ij})\right] \tag{2.10}$$

Here $f_R$ is the repulsive pair potential, $f_A$ is the attractive pair potential associated with bonding, and $f_C$ is a smooth cut-off function. They are given by

$$f_R(r) = A\exp(-\lambda_1 r) \tag{2.11}$$

$$f_A(r) = -B\exp(-\lambda_2 r) \tag{2.12}$$

$$f_C(r) = \begin{cases} 1 & ,r < R - D \\ \frac{1}{2} - \frac{1}{2}\sin\left(\frac{\pi}{2}(r-R)/D\right) & ,R - D < r < R + D \\ 0 & ,r > R + D \end{cases} \tag{2.13}$$

where the cut-off function is continuous and smooth over all $r$, and goes from 1 to 0 in a small range around $R$. $A$, $B$, $\lambda_1$, $\lambda_2$, $R$ and $D$ are parameters.

The novel feature of the TR potential is the $b_{ij}$ term in Equation 2.10. It represents a measure of the bond-order.

$$b_{ij} = (1 + \beta^n \zeta_{ij}^n)^{-1/2n} \tag{2.14}$$

$$\zeta_{ij} = \sum_{k \neq i,j} f_C(r_{ik}) g(\theta_{jik}) \exp[\lambda_3^3 (r_{ij} - r_{ik})^3] \tag{2.15}$$

$$g(\theta) = 1 + c^2/d^2 - c^2/[d^2 + (h - \cos\theta)^2] \tag{2.16}$$

where $r_{ij}$ is the length of the $ij$ bond, and $\theta_{jik}$ is the bond angle between bonds $ij$ and $ik$. $\beta$, $n$, $\lambda_3$, $c$, $d$ and $h$ are parameters. The expression includes the smooth cut-off function $f_C(r)$, which limit the range of interaction to the first neighbour shell. The bond-order $b_{ij}$ is able to discriminate pairs of bonds regarding their neighbour atoms with the help of $g(\theta)$ term. Clearly $b_{ij} \neq b_{ji}$.

The function $a_{ij}$ is similar to $b_{ij}$ but without $g(\theta)$ term. It consists solely of range-limiting term $f_C(r)$. However it is usually not used, i.e. $a_{ij} = 1$. The bond-orders describe many-body potentials without yielding plenty of parameters.

The TR potential takes the form of pair potentials which seems only consider the two-body potentials, but it actually takes many-body potentials into account as well by introducing the bond-order $b_{ij}$. Because while calculating the bond-order $b_{ij}$, it takes all its neighbour atoms into account and the many-body potentials are included.

### 2.2.3 Analytical Bond-Order Potential

Recent research on the accuracy of existing atomic potentials for the CdTe semiconductor compound[54] shows that neither SW potential nor TR potential is sufficiently accurate at predicting the properties of CdTe, while these properties are necessary for understanding defects. D. G. Pettifor and I. I. Oleinik developed the analytical bond-order potential (BOP) in 1999[55], and the BOPs were applied to many materials, such as hydrocarbons[56] and CdTe[57].

The BOP is based on quantum-mechanical theories. It is an extension to the TR potential. Similar to the TR potential, the BOP uses the bond-orders to describe the many-body potentials. As known the covalent bonds are the most common bonds in the compounds. In chemistry, there are different types of covalent bonds categorising by different ways of formation, such as $\sigma$ bond and $\pi$ bond. The TR potential can be viewed as an empirical BOP, and considering only the $\sigma$ bonding with a second-moment approximation[58]. To improve the accuracy of describing interatomic interactions, the analytical BOP incorporates both $\sigma$ and $\pi$ bondings with a four-moment approximation[57]. Therefore the BOP in principle is more accurate than SW and TR potentials.

The analytic expression for the BOP is derived from tight-binding theory, where the bond energy is a multiplication of the bond-order $\Theta$ and bond integral $\beta$. The total energy of a system containing $N$ atoms is expressed as

$$E = \frac{1}{2}\sum_{i=1}^{N}\sum_{j=i_1}^{i_N}\phi_{ij}(r_{ij}) - \sum_{i=1}^{N}\sum_{j=i_1}^{i_N}\beta_{\sigma,ij}(r_{ij})\cdot\Theta_{\sigma,ij} - \sum_{i=1}^{N}\sum_{j=i_1}^{i_N}\beta_{\pi,ij}(r_{ij})\cdot\Theta_{\pi,ij} \quad (2.17)$$

where $\phi_{ij}$ is a short-range two-body potential representing the overlap repulsion between a pair of ion cores[58], $\beta_{\sigma,ij}$ and $\beta_{\pi,ij}$ are, respectively, $\sigma$ and $\pi$ bond integrals, $\Theta_{\sigma,ij}$ and $\Theta_{\pi,ij}$ are, respectively, $\sigma$ and $\pi$ bond-orders, $r_{ij}$ is the interatomic distance between atom $i$ and $j$, where $j = i_1, i_2, \ldots, i_N$ represents neighbours of atom $i$. $\phi_{ij}(r_{ij})$, $\beta_{\sigma,ij}(r_{ij})$ and $\beta_{\pi,ij}(r_{ij})$ are expressed in a general form as:

$$X_{ij}(r_{ij}) = X_{0,ij}\cdot f_{ij}(r_{ij})^{m_{ij}}\cdot f_{c,ij}(r_{ij}) \quad (2.18)$$

where $X$ represents $\phi$, $\beta_\sigma$ or $\beta_\pi$, $X_{0,ij}$ and $m_{ij}$ are pair dependent parameters, $f_{c,ij}(r_{ij})$ is a cut-off function, and $f_{ij}(r_{ij})$ is a Goodwin-Skinner-Pettifor radial func-

tion[59], similar to the LJ potential and given by

$$f_{ij}(r_{ij}) = \frac{r_{0,ij}}{r_{ij}} \exp\left[\left(\frac{r_{0,ij}}{r_{c,ij}}\right)^{n_{c,ij}} - \left(\frac{r_{ij}}{r_{c,ij}}\right)^{n_{c,ij}}\right] \tag{2.19}$$

$$\tag{2.20}$$

where $r_{0,ij}$, $r_{c,ij}$ and $n_{c,ij}$ are pairwise parameters.

The new features in the BOP is the way of calculating bond-orders $\Theta_{\sigma,ij}$ and $\Theta_{\pi,ij}$. They are functions of the local environment of atoms $i$ and $j$ and can be viewed as environment-dependent local variables. The maximum value of $\sigma$ and $\pi$ bond-orders are 1 and 2, respectively. These bond-orders reflect the common single-, double-, and triple-bond behaviour of chemistry. By using the tight-binding theory, the analytical expressions of bond-orders can be derived. In the BOP, the first two and four levels of the recursive representations for the $\sigma$ and $\pi$ bond-orders, respectively, are taken.

The Cyrot-Lackmann theorem states that bond-orders can be understood in terms of molecular orbital hopping paths[55]. These hopping paths incorporate bond lengths and (three- and four-body) bond angles, and the most important ones are shown in Figure 2.1. The two-level $\sigma$ bond-order for the BOP with a half-full valence shell is given by

$$\Theta_{\sigma,ij}^{(1/2)} = \frac{\beta_{\sigma,ij}(r_{ij})}{\sqrt{\beta_{\sigma,ij}^2(r_{ij}) + c_{\sigma,ij} \cdot A_\sigma + \zeta_1}} \tag{2.21}$$

$$A_\sigma = \beta_{\sigma,ij}^2(r_{ij}) \cdot \Phi_{2\sigma}^i + \beta_{\sigma,ij}^2(r_{ij}) \cdot \Phi_{2\sigma}^j \tag{2.22}$$

where $c_{\sigma,ij}$ is a parameter, $\zeta_1$ is a small number to remove singularities, and $\Phi_{2\sigma}^i$ is a local variable arising from 2-hops in the $\sigma$ bonding shown in Fig 2.1(a). The general $\sigma$ bond-order is then extrapolated.

$$\Theta_{\sigma,ij} = \Theta_{s,ij}\left(\Theta_{\sigma,ij}^{(1/2)}, f_{\sigma,ij}\right) \cdot \left[1 - \left(f_{\sigma,ij} - \frac{1}{2}\right) \cdot k_{\sigma,ij} \frac{\beta_{\sigma,ij}^2(r_{ij}) \cdot R_{3\sigma,ij}}{\beta_{\sigma,ij}^2(r_{ij}) + \frac{A_\sigma}{2} + \zeta_2}\right] \tag{2.23}$$

where $f_{\sigma,ij}$ and $k_{\sigma,ij}$ are pairwise parameters, $\zeta_2$ is a small number, $R_{3\sigma,ij}$ is a local variable arising from 3-hops in the $\sigma$ bonding shown in Fig 2.1(a), and the symmetric band-filling function $\Theta_{s,ij}$ is expressed as a spline function, which is omitted here.

For a better understanding of Equation 2.23, especially the $\Phi_{2\sigma}^i$ and $R_{3\sigma,ij}$ terms

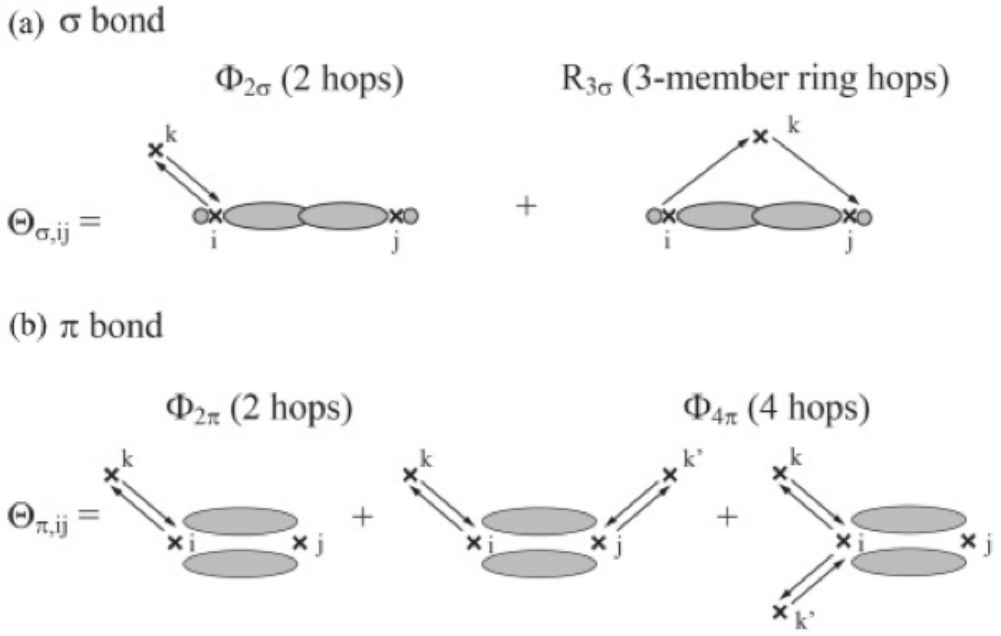


**Figure 2.1:** A schematic representation of the hopping paths that sample the local configuration around the $ij$ bond: (a) the primary $\sigma$ bond and (b) the secondary $\pi$ bond. Figure taken from [57].

with respect to Fig 2.1(a), we create a simple 3-atom system, as shown in Fig 2.2, and calculate the changes of force acting on the highlight atom while moving around a CdTe dimer. The separation of CdTe atoms in the dimer is chosen to be $R = 2.96$ Å. The positive angle $\theta^+$ means the highlighted Te atom moves around the Te atom, while the negative angle $\theta^-$ means it moves around the Cd atom in the dimer. The changes of force acting on the highlighted Te atom versus rotation angle $\theta$ is shown in Figure 2.3.

Pettifor [55] deduces the analytic expression for the $\pi$ bond-order, and is give by

$$\Theta_{\pi,ij} = \frac{\alpha_{\pi,ij} \cdot \beta_{\pi,ij}(r_{ij})}{\sqrt{\beta^2_{\pi,ij}(r_{ij}) + c_{\pi,ij} \cdot \left(\frac{A_\pi}{2} + \sqrt{\beta^4_{\pi,ij}(r_{ij}) \cdot \Phi_{4\pi,ij} + \zeta_3}\right) + \zeta_4}} + \frac{\alpha_{\pi,ij} \cdot \beta_{\pi,ij}(r_{ij})}{\sqrt{\beta^2_{\pi,ij}(r_{ij}) + c_{\pi,ij} \cdot \left(\frac{A_\pi}{2} - \sqrt{\beta^4_{\pi,ij}(r_{ij}) \cdot \Phi_{4\pi,ij} + \zeta_3} + \sqrt{\zeta_3}\right) + \zeta_4}} \tag{2.24}$$

$$A_\pi = \beta^2_{\pi,ij}(r_{ij}) \cdot \Phi^i_{2\pi,ij} + \beta^2_{\pi,ij}(r_{ij}) \cdot \Phi^j_{2\pi,ij} \tag{2.25}$$

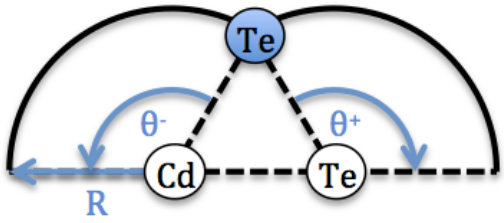


**Figure 2.2:** A simple 3-atom system illustrating the bond order potential. We calculate the force acting on the highlighted Te atom, which moves around the CdTe dimer underneath. The distance between the CdTe dimer is $R$, and the Te atom moves around the Cd/Te with a radius $R$ as well. The positive angle $\theta^+$ means the highlighted Te atom moves around the Te atom, while the negative angle $\theta^-$ means it moves around the Cd atom in the dimer.

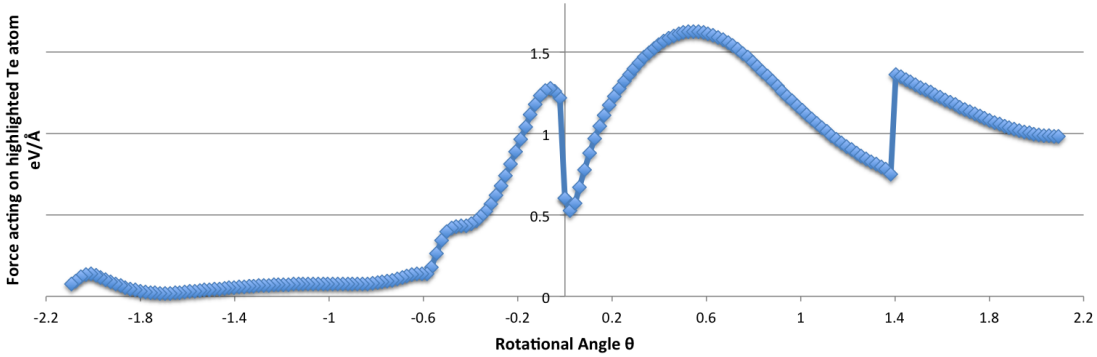


**Figure 2.3:** Force acting on highlighted Te atom in Figure 2.2 versus rotation angle $\theta$.

where $\alpha_{\pi,ij}$ and $c_{\pi,ij}$ are pairwise parameters, $\zeta_3$ and $\zeta_4$ are small numbers, and $\Phi^i_{2\pi,ij}$ and $\Phi_{4\pi,ij}$ are, respectively, local variables arising from 2- and 4-hops in the $\pi$ bonding shown in Fig 2.1(b).

The BOP is much more complex and more accurate than the SW and TR potentials. In addition of $\sigma$ bonding, which is only bonding considered in the TR potential, the BOP also considers $\pi$ bonding. And moreover, the BOP also considers three-body term, $R_{3\sigma,ij}$, in $\sigma$ bondings and four-body term, $\Phi_{4\pi,ij}$, in $\pi$ bondings.

D.K. Ward et al. applied the analytical BOP to CdTe in 2012[57]. The BOP parametrisation of CdTe is done independently for Cd, Te and finally for CdTe. The analytical BOP for CdTe binary system accurately captures property trends and it results in crystalline growth in vapour deposition simulations.

Early studies on the bonding in CdTe[60] indicate that CdTe is only weakly ionic, the effective ionic charge with CdTe should be only a fraction of an electronic charge. Therefore it is possible to use a potential without electrostatic contributions for CdTe surface calculations. D.K. Ward, who applied the BOP to CdTe,[57] also studied the surface energies for CdTe with BOP and they fit well with the same calculations using DFT. These showing that the BOP is indeed suitable for CdTe surface calculations.

In the meanwhile, the potential is developed and included in the LAMMPS package and free to use. Therefore we choose this potential for all simulations throughout this work.

## 2.3 Boundary Conditions

MD is limited by the size of system to be simulated. The more atoms there are in the system, the slower the simulations to evolve the system. Typically in the MD simulations, the number of atoms in the system varies from thousands to millions. The number has increased over years with higher computer technology and faster computational speed. But it is still not possible to simulate realistic number of atoms, which might be at least quadrillions. However, it is possible to keep the size of system small whilst retaining some of the properties of a larger system, therefore predict some interesting mechanisms by simulating small systems.

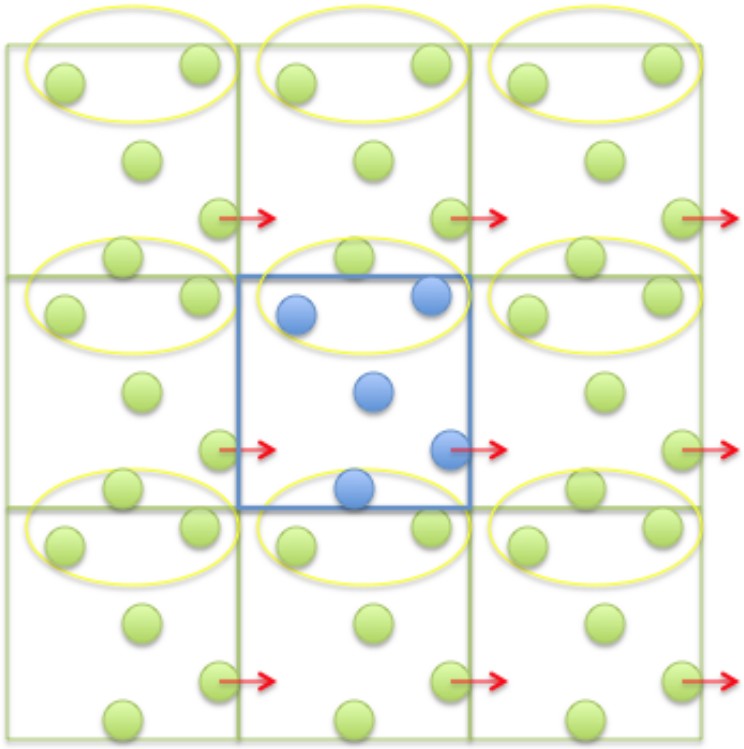

**Figure 2.4:** Illustration of periodic boundary conditions in 2D. The blue cell in the middle represents the simulation box. Atom exist the boundary will re-enter from the other side. Atoms near the edges will regards the other edges' atom as neighbours.

### 2.3.1 Periodic Boundary Conditions

By using periodic boundary conditions (PBCs), we can extend the size of system to be simulated by imagining the simulation box is only part of the system, and it is surrounded by its replicas. In other words, once the atom leaves from one side of the simulation box, it would enter the simulation box from the other side. Moreover, atoms close to edges of the simulation box will regard all the opposite edges' atoms as neighbours, interacting with them as normal. An illustration is shown in Figure 2.4.

### 2.3.2 Fixed/Free Boundary Conditions

When the fixed boundary conditions (FBCs) are applied, the edges of the simulation box behave like walls. We usually fixed the outer layer(s) of atoms, to stop atom(s)

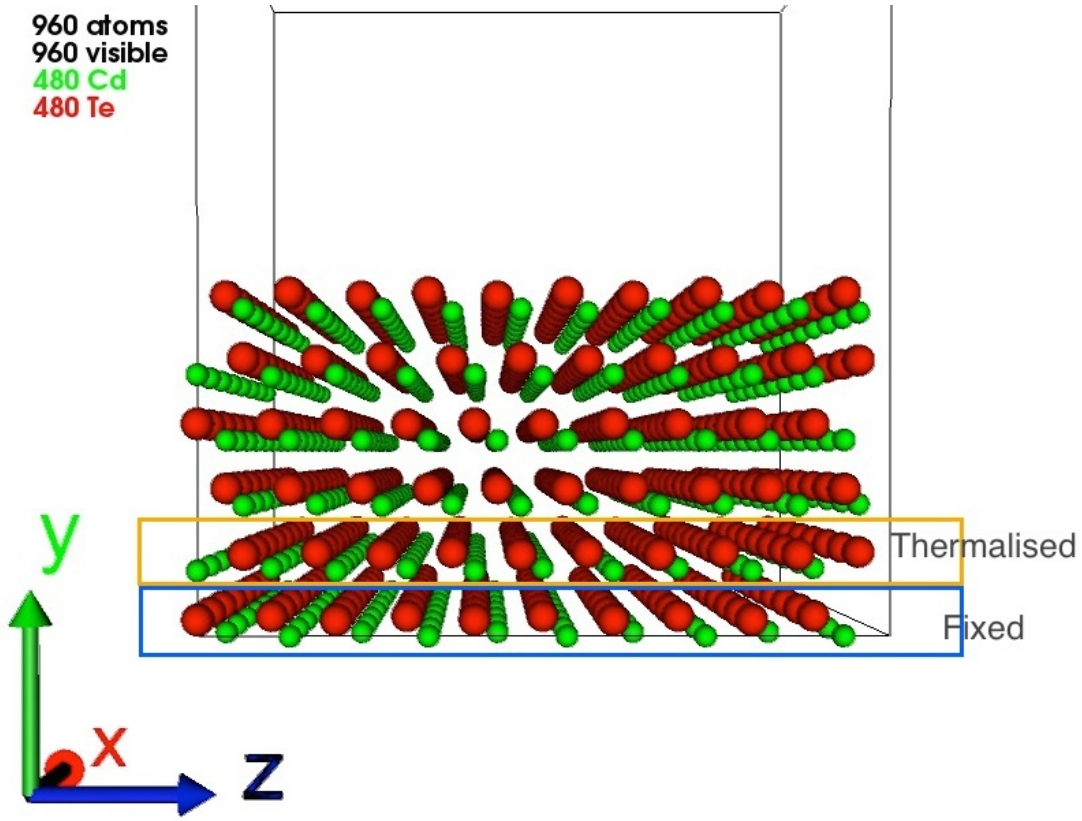


**Figure 2.5:** Simulation box for energetic impacts and growth simulations. Red bigger spheres represent the Cd atoms, green smaller spheres the Te atoms. PBCs are applied in x and z directions, and FBC is applied in y direction. Blue layers indicates layers of atoms to be fixed, and orange layers indicates the thermalised layers, which will allow for system heating and cooling.

going over the edges and to allow reproduction of lattice strain. The fixed outer layers of atoms applies an artificial pressure on atoms inside the bulk, simulating the surrounding bulk.

When the free boundary conditions are applied, if atom(s) move towards the edges, the atom(s) will be removed once they exceed the simulation box. The free boundary conditions are usually applied together with fixed boundary conditions in the surface growth simulations. For example, when simulating energetic impact onto a surface, fixed boundary conditions are applied to bottom two layers (blue layers in Figure 2.5), while the surface remains free. A fixed boundary condition must be applied on the bottom layer during the energetic impacts, otherwise the whole block of material would drift downwards.

## 2.4 Thermalisation

In some cases, we need to maintain the temperature of the system at a desired temperature. For example, in a real system containing billions of atoms, when energetic impacts occurs, energy would eventually dissipate away from the impact area. However for a smaller system containing only a few thousand atoms, the impacts would cause the increasing temperature of the whole system. In practice, the temperature of film growth is barely changed during the growth process. Thus thermalisation is necessary. And it is also used for the initial heating of the system.

There are several different thermalisation methods available in the LAMMPS package. In this work, the thermostat we are using is the Berendsen thermostat [61]. We use Berendsen method due to its simplicity, and that it gives a very stable temperature.

In the Berendsen thermostat, the temperature of a system, $T$, can be calculated in the following way:

$$T = \frac{2 \cdot KE_{\text{avg}}}{3 \cdot k_B} \tag{2.26}$$

where $k_B$ is the Boltzmann constant, $KE_{\text{avg}}$ is the average atomic kinetic energy of the system.

The kinetic energy is proportional to the square of velocity. The Berendsen thermostat controls temperature by rescaling the velocities of atoms every time step. The temperature of the system is corrected by scaling velocities from $v$ to $\lambda v$, such that the deviation exponentially decays with time constant $\tau_T$.

$$\frac{dT}{dt} = \frac{1}{\tau_T} \cdot (T_0 - T) \tag{2.27}$$

$$\lambda = \left[1 + \frac{\Delta t}{\tau_T}\left(\frac{T}{T_0} - 1\right)\right]^{1/2} \tag{2.28}$$

where $T_0$ is the desired temperature, $T$ is the actual temperature, $\Delta t$ is the time step. With Berendsen thermostat we can increase or decrease system temperature, and eventually bring the system to desired temperature.

In our simulations, we first heat the whole system to the desired temperature. Afterwards the thermalisation is only applied to the thermalised layer(s) of the

system (orange layers in Figure 2.5) to allow the impact energy dissipate on the surface.

## 2.5 System Relaxation

It is often necessary to relax a system to its minimal energy configuration during a simulation. Especially after successful impacts on the surface, the system relaxation makes sure the system is in its minimal energy configuration. Moreover, the system relaxation is also used in saddle point search methods, which will be introduced in Chapter 3.

There are various system relaxation techniques, such as steepest descent, conjugate gradient (CG), quasi-Newton, Limited memory Broyden-Fletcher-Goldfarb-Shanno algorithm for Bound constrained optimisation (L-BFGS-B) etc. In this work, we mainly use two system relaxation techniques: CG and L-BFGS-B.

### 2.5.1 Conjugate Gradient

The conjugate gradient (CG) method is initially developed by M. R. Hestenes and E. Stiefel in 1952[62]. It is an algorithm for the numerical solution of linear equations, whose matrix is symmetric and positive-definite, and it can also be used for energy minimisation[63]. There are several different implementations on the CG method, for example Fletcher-Reeves method[64] and Polak-Ribiere method[65]. The CG method we use in this work is the Polak-Ribiere method.

The CG method starts with calculating the gradient, $\mathbf{g}_n$, from the atomic forces, $\mathbf{F}$, at the configuration, $\mathbf{r}_n$:

$$\mathbf{g}_n = \mathbf{g}(\mathbf{r}_n) = -\nabla \mathbf{F}(\mathbf{r}_n) \tag{2.29}$$

Then the system moves to a new configuration, $\mathbf{r}_{n+1}$:

$$\mathbf{r}_{n+1} = \mathbf{r}_n + \alpha_n \cdot \mathbf{d}_n \tag{2.30}$$

where $\alpha_n$ is the linear search parameter, obtained by minimising the function $\mathbf{F}(\mathbf{r})$

along the $\mathbf{d}_n$ direction. The direction, $\mathbf{d}_n$, is given by:

$$\mathbf{d}_0 = \mathbf{g}_0 \tag{2.31}$$

$$\mathbf{d}_n = \mathbf{g}_n + \beta_n \cdot \mathbf{d}_{n-1} \tag{2.32}$$

where the value of parameter $\beta_n$ in the Polak-Ribiere method is given by

$$\beta_n = \frac{\|\mathbf{g}_n\|^2 - \mathbf{g}_n \cdot \mathbf{g}_{n-1}}{\|\mathbf{g}_{n-1}\|^2} \tag{2.33}$$

The CG method keeps updating the configuration $\mathbf{r}_n$ using the above algorithm until the gradient $\mathbf{g}_n$ converges to zero and therefore find the minimum energy configuration of the system.

### 2.5.2 L-BFGS-B

The Broyden-Fletcher-Goldfarb-Shanno (BFGS) algorithm belongs to the quasi-Newton methods family, which can be used to find local maxima and minima of functions. The BFGS uses gradient evaluations to approximate the Hessian matrix.

The BFGS method start with an initial guess of configuration, $\mathbf{r}_0$, and initial approximation of the Hessian, $\mathbf{H}_0$.

Similar to the CG method, we first calculate the direction, $\mathbf{d}_0$, by solving:

$$\mathbf{H}_n \mathbf{d}_n = -\nabla F(\mathbf{r}_n) \tag{2.34}$$

Then the system moves to a new configuration with a suitable step size $\alpha_n$ by using Equation 2.30. Afterwards the new gradient $-\nabla F(\mathbf{r}_{n+1})$ can be calculated. Therefore we can update the Hessian approximation using

$$\begin{aligned}\mathbf{H}_{n+1} = \mathbf{H}_n &+ \frac{(\nabla F(\mathbf{r}_{n+1}) - \nabla F(\mathbf{r}_n))(\nabla F(\mathbf{r}_{n+1}) - \nabla F(\mathbf{r}_n))^\top}{(\nabla F(\mathbf{r}_{n+1}) - \nabla F(\mathbf{r}_n))^\top (\alpha_n \mathbf{d}_n)} \\ &- \frac{\mathbf{H}_n (\alpha_n \mathbf{d}_n)(\alpha_n \mathbf{d}_n)^\top \mathbf{H}_n}{(\alpha_n \mathbf{d}_n)^\top \mathbf{H}_n (\alpha_n \mathbf{d}_n)}\end{aligned} \tag{2.35}$$

The BFGS method will repeat the above algorithm until the Hessian converged, which is used to find the minimum energy configuration of the system.

An improved BFGS method, Limited Memory BFGS algorithm for Bound constrained optimisation (L-BFGS-B)[66;67], which is implemented in the open source

library SciPy for Python[68], is used in this work. Comparing to BFGS algorithm, the L-BFGS-B allows user to control the memory required for storing Hessian and also it can handle simple box constraints on variables. Therefore the L-BFGS-B is very efficient and suited for optimising functions with massive number of variables.

## 2.6 Visualisation

During the simulations, the atomic positions of the system are stored. Huge amounts of data are generated during simulations. Data visualisation is an efficient way to analyse the results. In this work, we use a 3D Atomic Visualiser developed by C. Scott since 2012. The Visualiser is written in Python programming language, and is able to render atoms using POV-ray (the Persistence of Vision Raytracer[69]), a free software tool for creating stunning three-dimensional graphics. It allows the user to zoom and rotate the system. The Visualiser also provide many useful filters for visualising a system in different ways, such as highlight defects, option to view part of the lattice, option to colour by species or height, display bonds etc. Once one has set up the preferred display options, the Visualiser can generate a single graph for a given system, or generate a sequence of graphs for groups of systems and create a movie. The user interface of the Visualiser is shown in Figure 2.6.

This work is to simulate the CdTe thin film growth. Therefore we only focus on the surface layers and the deposited clusters. Thus throughout this work, all graphs generated from the Visualiser (unless specified) is a top view of the lattice, showing the top 2 surface layers together with deposited atoms/clusters. PBCs are applied in $x$ and $z$ directions. In the graph, bigger spheres represent the Te atoms, while smaller spheres the Cd atoms, and the atoms are coloured by height.

MD is very useful in simulating many interesting processes, especially short time scale dynamics, e.g. sputtering, crack propagation and nanoindentation. Many processes of interest in materials science are, however, not able to be modelled by MD. This is because the integration is sequential in nature, and it would take years to simulate the system for one second even on today's fastest processors[70]. Normally, it is very difficult to reach even one microsecond ($\mu$s) for very small systems, and it just about possible to reach nanoseconds (ns) on larger systems. The problem is that many interesting phenomena in materials science occur on time scales of seconds or longer, thus MD is not feasible. Recently, many people have been working on

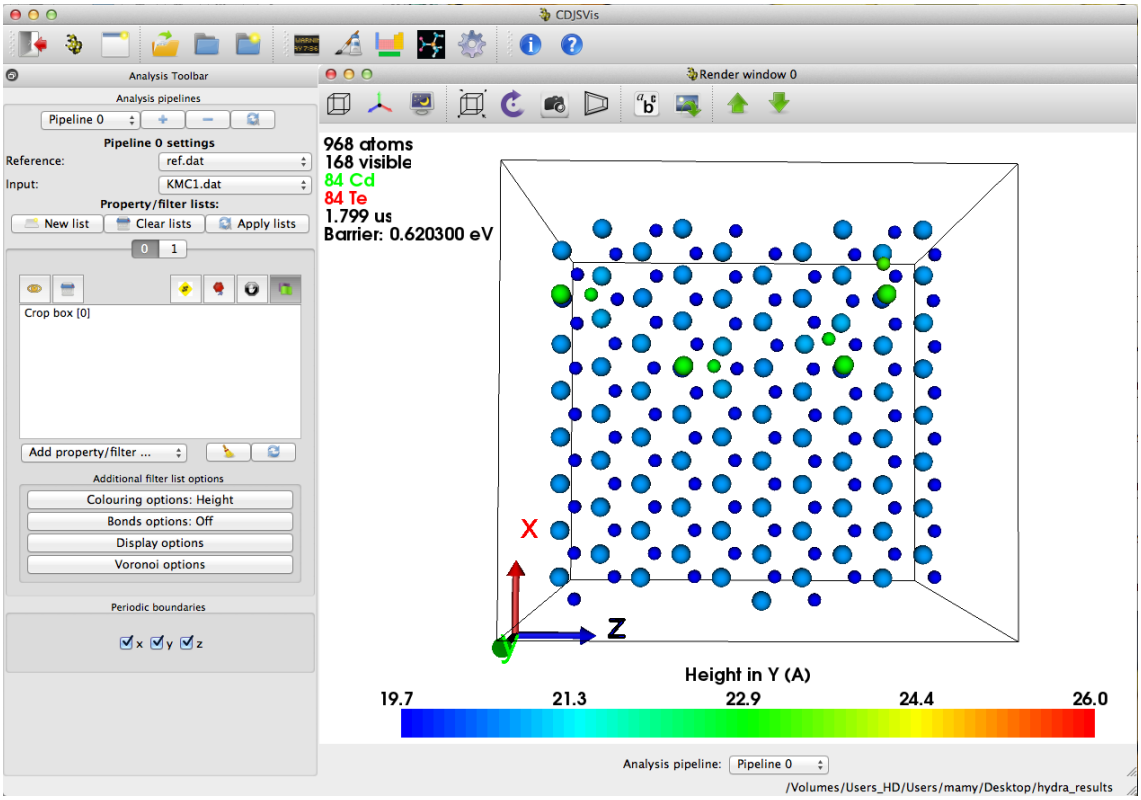


**Figure 2.6:** The user interface of the 3D Atomic Visualiser (©2014 Chris Scott). The generated atomic graph is a top view of the lattice, showing the top 2 surface layers together with deposited atoms/clusters. PBCs are applied in $x$ and $z$ directions. In the graph, bigger spheres represent the Te atoms, while smaller spheres the Cd atoms, and the atoms are coloured by height.

long time scale dynamics (LTSD) to overcome this problem. These methods are introduced later in Chapter 3.

# Chapter 3

# Methodology II: Long Time Scale Dynamics

## 3.1 Introduction

Chapter 2 introduced the Molecular Dynamics (MD), which can only simulate up to nanosecond[1] time scales for small systems and up to microsecond[2] time scales for larger systems. However many interesting phenomena in materials science occur on time scales of seconds or longer, thus MD is not feasible. One example of this is thin film growth. The rate for this is typically of the order of a few monolayers per second. To model growth, one needs to simulate the deposition of several layers, thus a few seconds of time. It is not possible to simulate directly by MD, since this time scale is $10^9$ orders of magnitude larger than a nanosecond. Another example that cannot simulate by direct MD is diffusion in solid state, which often occurs over time scales of seconds or even longer.

Recently many people have been working on long time scale dynamics (LTSD) techniques to overcome this problem. There are many LTSD techniques, which can extend the MD simulation time in an accurate way for materials problems[70], such as hyper-dynamics[71], parallel replica dynamics[72], temperature accelerated dynamics[73] and kinetic Monte Carlo (KMC) methods[74;75].

The system we discuss throughout this work is an infrequent event system. Our aim is to simulate the long timescale evolution of the system. The solution is to find

[1] 1 ns = $10^{-9}$ s
[2] 1 $\mu$s = $10^{-6}$ s

the barriers which the trajectory would go across and evolve the system. The LTSD methods are used to simulate the system trajectory, finding a path for escape more quickly than it would with direct MD. As in MD, no previous knowledge about the escape path is given; the trajectory has to find its own way out.

In the hyper-dynamics approach, the potential surface of the system is modified by adding a non-negative bias, which is zero at the dividing surfaces between states. Then the trajectory on this surface will escape more rapidly due to shallower minima, i.e., lower barriers which the trajectory would get across.

The parallel replica method is the simplest and the most accurate of the LTSD techniques. The parallel replica method accelerates the simulations by replicating the entire system on each of $M$ available parallel or distributed processors. After a short dephasing stage, during which momenta are periodically randomized to eliminate correlations between replicas. Each processor carries out an independent MD for the entire system, thus $M$ times faster than a single MD. Once a transition is detected, all processors are stopped. The simulation clock is advanced by the summed time over all replicas. The final state of the transition would be the new state for the next step, and the simulations go on with dephased $M$ replicas of this new state.

The idea of the temperature accelerated dynamics is to speed up the transitions by increasing the temperature, while filtering out the transitions that would not have occurred at the original temperature. In this method, the system is evolved at a high temperature, thus faster than in the temperature of interest, which is lower. Once a transition is detected, the rate for this transition is then reflected back to the original temperature using the harmonic transition state theory (hTST).

No matter which method is chosen to simulate in longer time scales, transition state theory (TST) is their theoretical foundation. An important problem for these simulations is to calculate the transition rates. One can obtain accurate estimates of transition rates using TST. The TST/hTST rate calculations will be presented in Section 3.2. But the most challenging thing is to find the saddle points. Later in Section 3.3, several saddle finding methods, namely activation relaxation technique (ART), relaxation and translation (RAT) method, dimer method, minimum mode following algorithm, Lanczos algorithm, nudged elastic band (NEB) method and string method will be introduced. Section 3.5 introduced the method of reusing transitions (refinements).

C. Scott, T. Lazauskas and I co-wrote the OTF-KMC script which is used

throughout this work. The main methodologies used in the OTF-KMC script are presented in this chapter. C. Scott and T. Lazauskas have implemented all saddle search algorithms and the reuse of transitions, and I am responsible for testing and debugging their implementations. The OTF-KMC script also include implementation of relaxation methods which are introduced in Section 2.5, and I am responsible for implementing relaxation methods using LAMMPS.

## 3.2 Kinetic Monte Carlo

The kinetic Monte Carlo (KMC) method is one of the LTSD techniques. It can simulate the system evolution while keeping the realistic dynamics of the system with known rates of processes. Similar to other LTSD techniques, the KMC method also relies on the transition state theory (TST)[70;76].

In the TST approximation, the classical rate constant for escape from state $A$ to some adjacent state $B$ is taken to be the equilibrium flux through the dividing surface between $A$ and $B$. If there are no correlated dynamical events, the TST rate is the exact rate constant. If we run the trajectory for so long time so as to reach equilibrium, we could determine the fraction of the time spends in state $A$ and the number of crossing, per unit time, of the dividing surface. Then the TST rate for escaping from $A$, $k_{A\rightarrow}^{TST}$, would be half of this crossing rate.[77]

$$k_{A\rightarrow}^{TST} = \frac{1}{2}\left\langle \left|\frac{dx}{dt}\right| \delta(x-q) \right\rangle_A \tag{3.1}$$

where the angular bracket indicate the ratio of Boltzmann-weighted integrals over $6N$-dimensional phase space, the subscript $A$ indicates the configuration space integrals are restricted to the space belonging to state $A$, and the dividing surface is at $x = q$.

A.F. Voter has proved that the integrals in Equation 3.1 are separable[77], and we can get

$$k_{A\rightarrow}^{TST} = \frac{1}{2}\sqrt{\frac{2k_BT}{\pi m}}\left\langle \delta(x-q)\right\rangle_A \tag{3.2}$$

where $k_B$ is the Boltzmann constant, $T$ is the temperature and $m$ is the effective mass of the reaction coordinate over the dividing surface, i.e. $m$ is the mass of particle passing from state $A$ to $B$.

In classical TST, rate constants are computed after the dividing surface is specified. However, in the LTSD methods, the dividing surfaces are usually not required to be known in advance. For a system close to harmonic at the minima and saddle points, the harmonic approximation to TST (hTST) can typically be used:

$$k_{A\rightarrow}^{hTST} = \frac{\Pi_i^{3N}\nu_i^{min}}{\Pi_i^{3N-1}\nu_i^{sad}}\exp(-E_a/k_BT) \tag{3.3}$$

where $E_a$ is the static barrier height, or activation energy (energy difference between the saddle point and the minimum), and $\nu_i$ are the corresponding normal mode frequencies.

To simplify the rate calculation, we usually use a fixed prefactor $\nu$ for rate calculation used in the LSTD.

$$R = \nu\exp(-E_a/k_BT) \tag{3.4}$$

The common choice of this fixed prefactor is between $10^{12}$ and $10^{13}$ $s^{-1}$. In the thin film growth simulations, if we choose a smaller prefactor, the time increments in each KMC step is larger, therefore there would be fewer diffusions between depositions. In this work, we use $\nu = 10^{13}$ $s^{-1}$ as suggested by L.J. Vernon[42], who have calculated the Vineyard's prefactor for many transitions and found that $10^{13}$ $s^{-1}$ is a good estimation, and also allowing enough diffusions between depositions in our thin film growth simulations.

### 3.2.1 Standard KMC

The main steps in a kinetic Monte Carlo (KMC) algorithm are outlined in Figure 3.1(a). Unlike the MD method, there is no classical trajectory at all. In the standard KMC approach, we only care about where and how the trajectory escape from the current state. By constructing a list of possible transitions and weighted by the rate constants, a transition is chosen randomly. The standard KMC algorithm is as follows:

**Step 1** Initialise simulation time (usually $t = 0$);

**Step 2** Construct available list of possible events with rate $r_i$, and the total rate is given by $R = \sum_i r_i$;

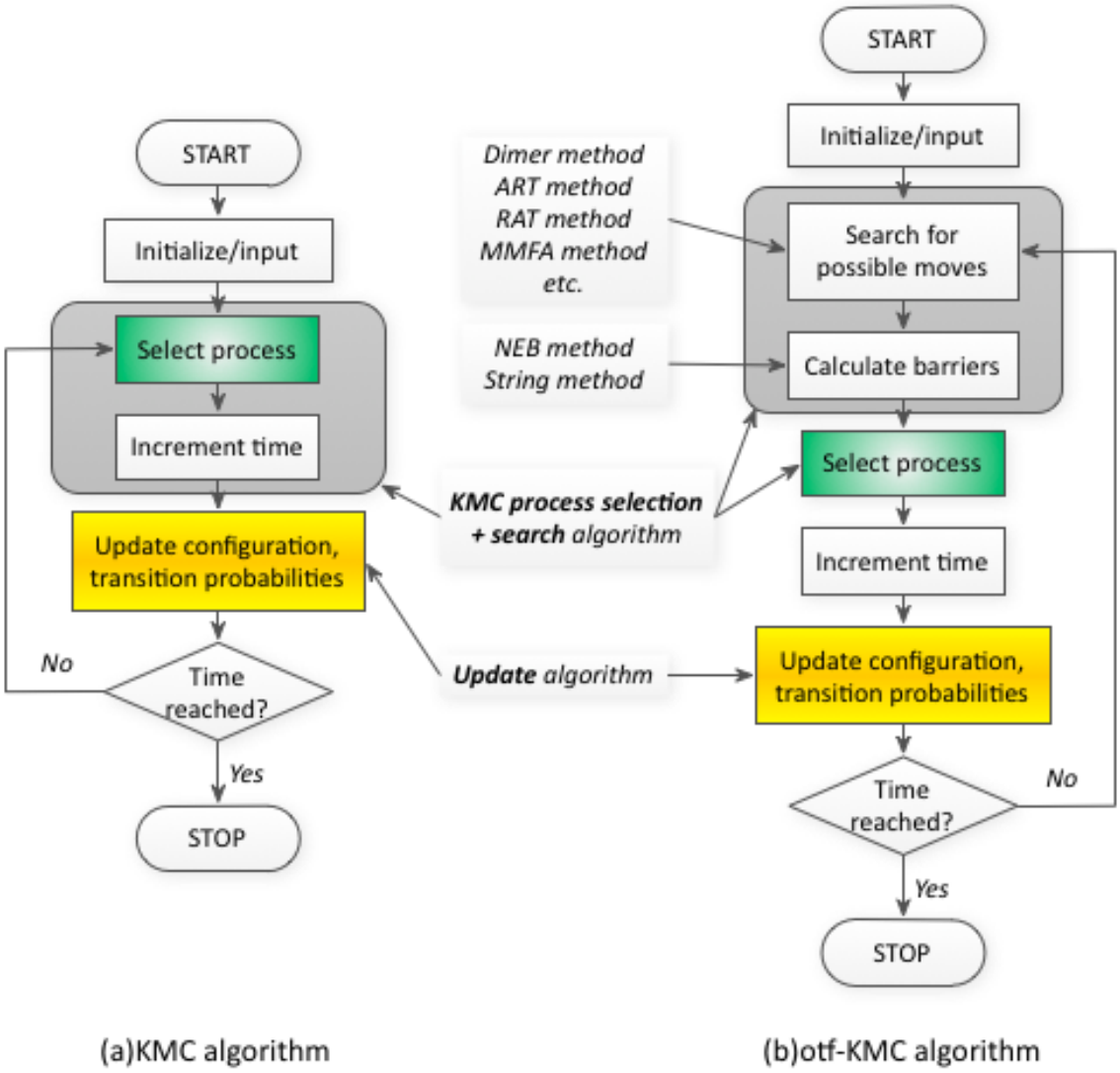


**Figure 3.1:** Flowcharts for KMC and OTF-KMC algorithm. The underlying principle in KMC algorithm is the random selection of a process based on the transition probabilities of all processes, execution of the selected process (i.e., appropriately modifying the configuration of the system), updating the time clock and the transition probabilities. There are two additional processes in the OTF-KMC algorithm. First search for possible moves using single-ended saddle searching method, and calculate barriers using NEB or string method. Then continue the generic KMC algorithm. Shaded boxes denote the computationally most expensive steps.

**Step 3** Choose a random number $P \in [0, R)$, and cumulatively step through all events until $P$ is exceeded;

**Step 4** Execute and selected event, and the system is advanced to next KMC step;

**Step 5** The simulation time is advanced by $\Delta t = -\ln u/R$, where $u \in [0, 1)$ is a random number;

**Step 6** Go back to Step 2 for next iteration unless the simulation time is reached.

### 3.2.2 On-the-fly KMC

The standard KMC algorithm requires generating a list of possible escape paths. Thus, it may be extremely difficult to compile an adequate KMC catalogue. In 2001, G. Henkelman and H. Jónsson initially extend the original KMC method to LTSD simulations without predefined event table[78], which is known as the on-the-fly KMC (OTF-KMC).

The main steps in the OTF-KMC algorithm are outlined in Figure 3.1(b). The OTF-KMC algorithm relies on the ability to search for barriers during the simulation, hence on the fly. The main improvement in the OTF-KMC is to use saddle point search algorithms to find all the low-lying saddles surrounding the current state, thus building a KMC catalogue on the fly. If all saddles are found, then one has an exact KMC, and even if only the relevant low-lying saddles are found, one has a very accurate KMC. Therefore is a very appealing approach.

The saddle searches in the OTF-KMC algorithm are the most computationally expensive part. In this work, we use a modified version of the OTF-KMC algorithm for LTSD simulations. The flowchart of the modified OTF-KMC algorithm is shown in Figure 3.2. The modified algorithm starts with identifying all the defects in the system by comparing with the reference system, and creating defect volumes (DVs) around each of the defect. The DV usually contains a few tens of atoms, and it is a collection of atoms surrounding around a point defect within a certain radii. Instead of searching the whole system for saddle points, we only search each of the DV for saddles. There are two main advantages: (1) generally it is faster to do searches on DVs than on the whole system, as DVs contain much fewer atoms; (2) transitions found in DVs can be reused occasionally in the following steps. For example, DV with one vacancy may continuously exist in the system for many steps, until another interstitial diffuses and fills the vacancy.

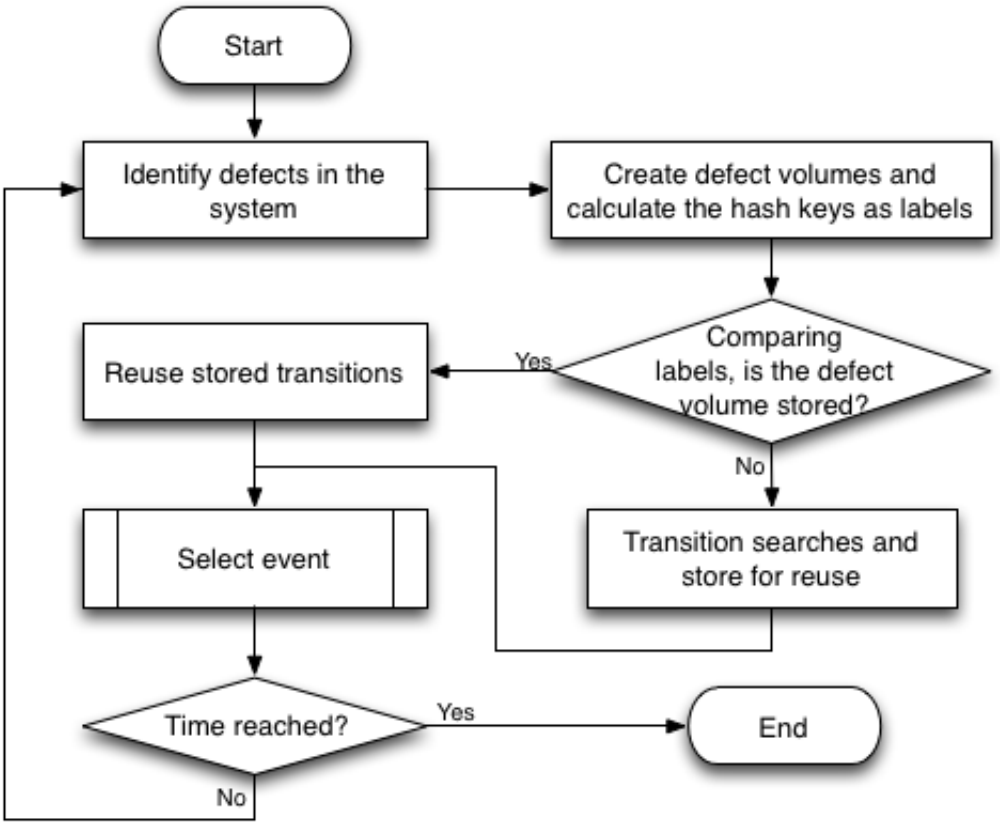


**Figure 3.2:** Flowchart of the modified OTF-KMC algorithm with reusing transitions. Comparing to the original OTF-KMC, the modified algorithm accelerates the simulations in two ways: (1) Instead of searching the whole system, we only search defect volumes, which are created around defects. (2) By labelling defect volumes with their hash keys, we can reuse the transitions found in previous steps.

The OTF-KMC algorithm mentioned throughout this work refers to the modified one with reusing transitions, as shown in Figure 3.2, unless specified. The details of the saddle search algorithms are explained in Section 3.3. And the reuse of transitions (refinements) is introduced in Section 3.5.

## 3.3 Saddle Finding Methods

In the LTSD methods, the most challenging part is to find escaping transitions, i.e. to find saddle points around the given state.

To help finding the saddle points, the minimum energy path (MEP) is introduced. The MEP is a path connecting two minima. At any point of the path, the direction of potential force is parallel to the path. The energy is stationary for any perpendicular degree of freedom. As we know, rank 1 saddle points are maxima of one degree of freedom and minima of other degrees of freedom. The MEP pass through saddle points and the maxima on the MEP are the saddle points. Thus by finding MEPs, one can get the saddle points.

Several single-ended search methods are introduced in this Section: activation relaxation technique (ART), relaxation and translation (RAT) method, dimer method, minimum mode following algorithm (MMFA) and Lanczos algorithm. All these methods start searching saddles from a given initial state, which is the reason they are called single-ended search methods. Two double-ended search methods are also introduced in this Section: nudged elastic band (NEB) method and string method. Both methods start searching saddles from given both initial and final states, which is the reason they are called double-ended search methods. For a specific transition, the double-ended search methods are normally slower but more accurate than the single-ended ones. However the single-ended search methods often do not find a transition while the double-ended ones usually do. Sometimes it might be more efficient to use single-ended search methods with low accuracy, and then switch to use double-ended search methods to calculate the accurate barriers.

The main techinique used for saddle searching in this work is the MMFA method, which uses the dimer method to get closer to the saddle and uses Lanczos method for saddle convergence.

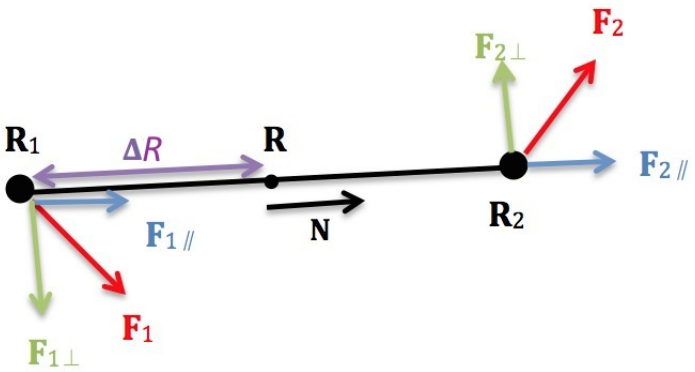


**Figure 3.3:** Illustration of the dimer. The actual force acting on the dimer (red) are decomposed into parallel (blue) and perpendicular (green) force components. The dimer $\mathbf{R}_1$ and $\mathbf{R}_2$ are centred at a state $\mathbf{R}$ with displacement $\Delta R$.

### 3.3.1 Dimer Method

The dimer method developed by G. Henkelman and H. Jónsson in 1999[79]. It's one of the most powerful and fast methods to find saddle points when only given the initial minimum.

The dimer method represent a given state $\mathbf{R}$ as two images (we call these two images a "dimer") with displacement $\Delta R$, as shown in Figure 3.3. Thus we get a dimer $\mathbf{R}_1$&$\mathbf{R}_2$ centred at $\mathbf{R}$, and then we can rotate and translate the dimer until find the saddle point.

The dimer method starts with creating a dimer from the given state $\mathbf{R}$. For a random displacement vector $\mathbf{N}$, 2 end points of the dimer, $\mathbf{R}_1$ and $\mathbf{R}_2$, are created by displacing a small distance, $\Delta R$, along $\mathbf{N}$, such that $\mathbf{R}_1 = \mathbf{R} - \Delta R\hat{\mathbf{N}}$ and $\mathbf{R}_2 = \mathbf{R} + \Delta R\hat{\mathbf{N}}$, where $\hat{\mathbf{N}}$ denotes the normalised displacement vector.

Forces acting on the dimer can be decomposed into parallel and perpendicular components, $\mathbf{F}_{i\parallel}$ and $\mathbf{F}_{i\perp}$, with respect to $\mathbf{N}$. Then the global rotational force acting on the dimer is given by:

$$\mathbf{F}_\perp = \mathbf{F}_{2\perp} - \mathbf{F}_{1\perp} \tag{3.5}$$

where $\mathbf{F}_\perp = \mathbf{F} - \mathbf{F}_\parallel$ and $\mathbf{F}_\parallel = (\mathbf{F} \cdot \hat{\mathbf{N}})\hat{\mathbf{N}}$.

In the rotation step, the rotational minimisation is performed to minimise the

global rotational force $\mathbf{F}_\perp$. The rotational plane of minimisation is defined by the orthonormal vectors $\mathbf{\Theta}$ and $\hat{\mathbf{N}}$. For the first minimisation, $\mathbf{\Theta} = \mathbf{F}_\perp$. After a trial rotation $d\theta$, $\mathbf{\Theta}^*$ is calculated by corresponding modified forces $\mathbf{F}^*$ and $\mathbf{F}^*_\perp$. Using the harmonic approximation of modified Newton method, we can calculate the minimisation rotational angle $\Delta\theta$[79]:

$$\Delta\theta \approx -\frac{1}{2}\arctan\left(\frac{2F}{F'}\right) \tag{3.6}$$

$$F = \mathbf{F}_\perp \cdot \mathbf{\Theta}/\Delta R \tag{3.7}$$

$$F' = \frac{dF}{d\theta} \approx \frac{\mathbf{F}^* \cdot \mathbf{\Theta}^* - \mathbf{F} \cdot \mathbf{\Theta}}{d\theta} \tag{3.8}$$

After the rotational minimisation, a translation scheme should be applied to update the position of the dimer. In the translation step, the dimer moves along the modified force direction at a fixed step size, i.e.

$$\mathbf{R}_{\text{new}} = \mathbf{R} + \hat{\mathbf{F}}_{\text{mod}} \times \text{StepSize} \tag{3.9}$$

where the modified force $\mathbf{F}_{\text{mod}}$ is given by:

$$\mathbf{F}_{\text{mod}} = \begin{cases} \mathbf{F}_\parallel & \text{if } C > 0, \\ \mathbf{F} - 2\mathbf{F}_\parallel & \text{if } C \leq 0. \end{cases} \tag{3.10}$$

$$C = \frac{(\mathbf{F}_2 - \mathbf{F}_1) \cdot \mathbf{N}}{2\Delta R} \tag{3.11}$$

where $C$ is the curvature of the potential surface along the dimer vector, $\mathbf{F} = \mathbf{F}_1 + \mathbf{F}_2$ is the global real force acting on the dimer, $\mathbf{F}_\parallel$ is the component of force parallel to the dimer vector.

Replicate the rotation and translation procedures and one can eventually find the saddle point.

### 3.3.2 Activation Relaxation Technique

The activation relaxation technique (ART) method was initially developed by G. T. Barkema and N. Mousseau[80] in 1996. Since then there have been several applications and improvements to the ART method[81;82;83]. The ART method start from a local minimum, then search for transitions in two steps: (1) Activation: climbing along MEP to find the saddle point; (2) Relaxation: push the system over the saddle

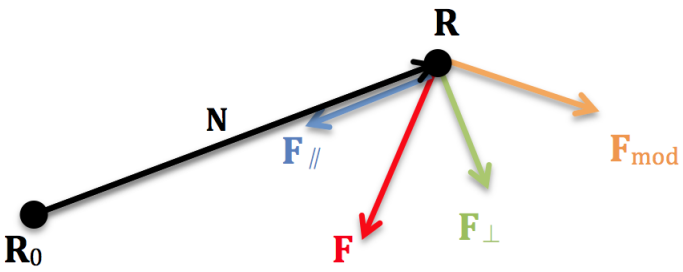


**Figure 3.4:** Illustration of force decomposition for the ART method. The actual force acting on images (red) are decomposited into parallel (blue) and perpendicular (green) components. The modified force (orange) represents the translation direction. The displacement vector **N** tethers the current position **R** to the origin $\mathbf{R}_0$.

and relax to a new minimum. We only use the activation part of ART method in this work.

As known that the direction of potential force on the MEP is parallel to the MEP, i.e. the perpendicular components of the force is zero on the MEP. We decompose the actual force of a point **R** with respect to the displacement vector **N**. The parallel component of the force is responsible for travelling toward the local minimum while the perpendicular component results in travelling towards the MEP. Thus a perpendicular relaxation of will allow the point to travel towards the MEP without relaxing towards the local minimum. After each step of relaxation, a new translation direction is calculated, and the relaxation is applied in the calculated translation direction. We repeat the translation and relaxation steps until reaches the stopping criteria.

After an initial random displacement, at each step, the vector **N** is constructed that tethers the current position **R** to the origin $\mathbf{R}_0$. Forces acting on **R** are decomposed into parallel and perpendicular components, $\mathbf{F}_{\parallel}$ and $\mathbf{F}_{\perp}$, as shown in Figure 3.4.

The key of ART method is to calculate the modified force $\mathbf{F}_{\text{mod}}$, which is also used as the translation direction:

$$\mathbf{F}_{\text{mod}} = \mathbf{F}_{\perp} - \alpha \mathbf{F}_{\parallel} \tag{3.12}$$

where $\alpha$ is a scalar variable that controls the climb away from the initial minimum,

and is chosen to be $0.15/|\mathbf{R} - \mathbf{R}_0|$. Here $|\cdot|$ indicates the L2-norm of a vector.

In the translation step, the search point $\mathbf{R}$ is then moving along the modified force direction using Equation 3.9. Then replicate the translation procedures with new directions calculated at each step until both $\mathbf{F}$ and $\mathbf{F}_{\text{mod}}$ vanish.

### 3.3.3 Relaxation And Translation Methods

The ART method requires large amount of translation searches to find the saddle points. While the relaxation and translation (RAT) method, developed by L. Vernon[42], aims to reduce the translation searches by doing force minimisation after every translation.

Unlike the ART method, in the RAT method, the vector $\mathbf{N}$ is constructed by tethering the current position $\mathbf{R}_i$ to the previous historical step $\mathbf{R}_{i-1}$. Similarly to the ART method, the RAT method relies on decomposition of forces into parallel and perpendicular components with respect to $\mathbf{N}$. The RAT method searches for saddle points in two steps: relaxation and translation.

In the relaxation step, after an initial displacement or translation step, force minimisation is applied. $\mathbf{R}'$ is relaxed along the direction $\mathbf{F}_\perp$ and moved to $\mathbf{R}$, as shown in Figure 3.5, with a variable step size depending on force change, which is given by:

$$\text{StepSize}_{j+1} = \begin{cases} 1.2 \cdot \text{StepSize}_j & \text{Ratio} < 1.2 \\ 0.5 \cdot \text{StepSize}_j & \text{Ratio} > 1.2 \end{cases} \tag{3.13}$$

$$\text{Ratio} = (\mathbf{F}_{\perp,j+1} - \mathbf{F}_{\perp,j})/\mathbf{F}_{\perp,j+1} \tag{3.14}$$

After the relaxation step, there are a pair of vectors $\mathbf{N}'$ and $\mathbf{N}$ define the initial and relaxed displacement of the search point, respectively. The new translation direction vector is constructed by:

$$\mathbf{N}'_{i+1} = \frac{\mathbf{N}_i + \mathbf{N}'_i}{|\mathbf{N}_i + \mathbf{N}'_i|} \tag{3.15}$$

Clearly, $\mathbf{N}'_{i+1}$ is normalised. The search point is then moved along this new direction. Replicate the relaxation and translation procedure until the dot product of parallel force component and displacement vector turns positive. The saddle point will be found then.

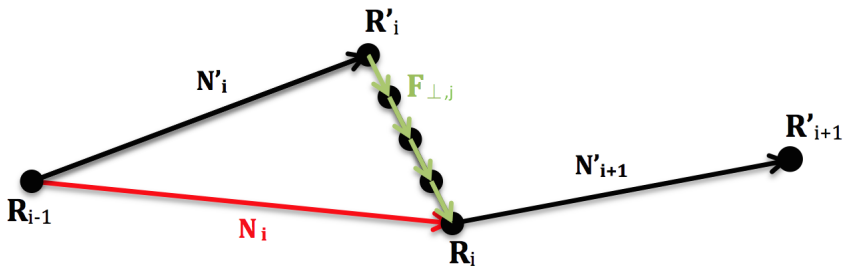


**Figure 3.5:** Schematic illustration of force minimisation in the RAT method. Green arrows indicate direction of perpendicular force component. The initial displacement vector $\mathbf{N}'$ tethers the current position $\mathbf{R}'_i$ to previous step $\mathbf{R}_{i-1}$, while the relaxed displacement vector $\mathbf{N}$ tethers the relaxed position $\mathbf{R}_i$ to $\mathbf{R}_{i-1}$.

### 3.3.4 Minimum Mode Following Algorithm

C. J. Cerjan and W. H. Miller first suggested to use eigenvectors of the Hessian for approaching saddle points in 1981 [84]. The Hessian is defined as a matrix of second-order partial derivatives of the potential forces, thus it is massively computational expensive to construct the full Hessian matrix, especially for large systems. In 2011, A. Pedersen, S. F. Hafstein and H. Jónssen developed the minimum mode following algorithm (MMFA) [85], which only uses the vector corresponding to the lowest eigenvalue (minimum mode) of the Hessian matrix to approach saddle points.

The saddle points we are trying to find are rank 1 saddles, i.e. the saddle is a maximum in one dimension and is minima in other dimensions. The basic idea of MMFA method is to invert the force along the maximum dimension, i.e. invert force along the eigenvector corresponding to the lowest eigenvalue of the Hessian:

$$\mathbf{F}^{\text{eff}} = \mathbf{F} - 2(\mathbf{F} \cdot \mathbf{v}_{\text{min}})\mathbf{v}_{\text{min}} \tag{3.16}$$

where $\mathbf{F}^{\text{eff}}$ is the effective force driving the system to a saddle point, $\mathbf{F}$ is the actual force and $\mathbf{v}_{\text{min}}$ is the eigenvector corresponding to the lowest eigenvalue of the Hessian. Therefore the rank 1 saddles would become a local minima, and we can use local optimisation algorithms to find them.

The MMFA method is the main algorithm used for saddle searching throughout this work. A. Pederson [85] suggested to use the dimer method (Section 3.3.1) to approach the saddle points and use the CG method (Section 2.5.1) for local

optimisation. However T. Lazauskas[86] found that a combination of the BFGS minimisation algorithm (Section 2.5.2) and the Lanczos method (Section 3.3.5) for eigenvector/eigenvalue calculation is the most appropriate in terms of unique successful searches. He also found that the combination of the dimer method with the MMFA has a good mixture of accuracy and speed. Therefore in this work, we choose the combination of dimer method with MMFA, together with BFGS minimisation algorithm and Lanczos method for eigenvector/eigenvalue calculation.

### 3.3.5 Lanczos Algorithm

The Lanczos algorithm is an iterative algorithm developed by C. Lanczos[87;88;89]. It is an efficient algorithm for calculating eigenvalues and eigenvectors of a symmetric matrix. In our case, the Hessian matrix at a certain point of the system is a symmetric matrix, where we use the L-BFGS-B algorithm introduced in Section 2.5.2 to approximate the Hessian. Thus we can use the Lanczos method for calculating the eigenvector corresponding to the lowest eigenvalue of the Hessian.

The Lanczos algorithm is actually not a saddle search algorithm. The Lanczos algorithm mentioned in this work usually refers to the MMFA method with using Lanczos algorithm for eigenvalue/eigenvector calculations.

Denote $\mathbf{A}$ as a $m \times m$ symmetric matrix whose eigenvalues and eigenvectors need to be determined, in our case the Hessian matrix. The Lanczos algorithm first converts this symmetric matrix to a tridiagonal symmetric matrix, with the following algorithm as suggested by C. C. Paige[88]:

**Step 1** Initialisation:

$\beta_1 = 0$;

$\mathbf{v}_0 = 0$;

$\mathbf{v}_1 =$ random normalised vector;

**Step 2** Loop for $i$ from 1 to $m - 1$:

$\mathbf{w}_i = \mathbf{A}\mathbf{v}_i$;

$\alpha_i = \mathbf{w}_i \cdot \mathbf{v}_i$;

$\mathbf{w}_i = \mathbf{w}_i - \alpha_i \mathbf{v}_i - \beta_i \mathbf{v}_{i-1}$;

$\beta_{i+1} = \|\mathbf{w}_i\|$,

$\mathbf{v}_{i+1} = \mathbf{w}_i / \beta_{i+1}$;

**Step 3** Finalisation:

$$\mathbf{w}_m = \mathbf{A}\mathbf{v}_m;$$
$$\alpha_m = \mathbf{w}_m \cdot \mathbf{v}_m;$$

Thus we get the tridiagonal symmetric matrix $\mathbf{T}$ given by

$$\mathbf{T} = \begin{pmatrix} \alpha_1 & \beta_2 & & & & 0 \\ \beta_2 & \alpha_2 & \beta_3 & & & \\ & \beta_3 & \alpha_3 & \ddots & & \\ & & \ddots & \ddots & \beta_{m-1} & \\ & & & \beta_{m-1} & \alpha_{m-1} & \beta_m \\ 0 & & & & \beta_m & \alpha_m \end{pmatrix} \tag{3.17}$$

Then we use the QR method, which is implemented from the Linear Algebra PACKage (LAPACK) library and is specially designed for estimating eigenvalues/eigenvectors of a tridiagonal symmetric matrix, to calculate the lowest eigenvalue and corresponding eigenvector of the tridiagonal symmetric matrix $\mathbf{T}$.

### 3.3.6 Nudged Elastic Band Method

The nudged elastic band (NEB) method was first introduced by Jónsson in 1998 [90] and improved later by G. Henkelman [91;92]. The NEB method is an efficient method for finding the MEP between two given initial and final states of a transition. As shown in Figure 3.6, by using elastic band method, one chooses $N+1$ images (nodes) in the potential field connecting the given initial and final minima. Imagine these images are linked with "elastic bands". On each image, both the potential force (true force) and the spring forces from its adjacent images are acting on it. The elastic band method allows the intermediate images move under these forces, while the endpoints (the initial and final states) are fixed.

To distinguish NEB method with other elastic band methods, the forces we use are force projections which ensure that the spring forces do not interfere with the convergence of the elastic band to the MEP, and ensure that the true forces do not affect the distribution of images along the MEP. Only the perpendicular component of the true force and the parallel component of the spring force are included. This force projection is referred to as "nudging".

Denote the $N+1$ images on an elastic band as $[\mathbf{R}_0, \mathbf{R}_1, \ldots, \mathbf{R}_N]$. The endpoints

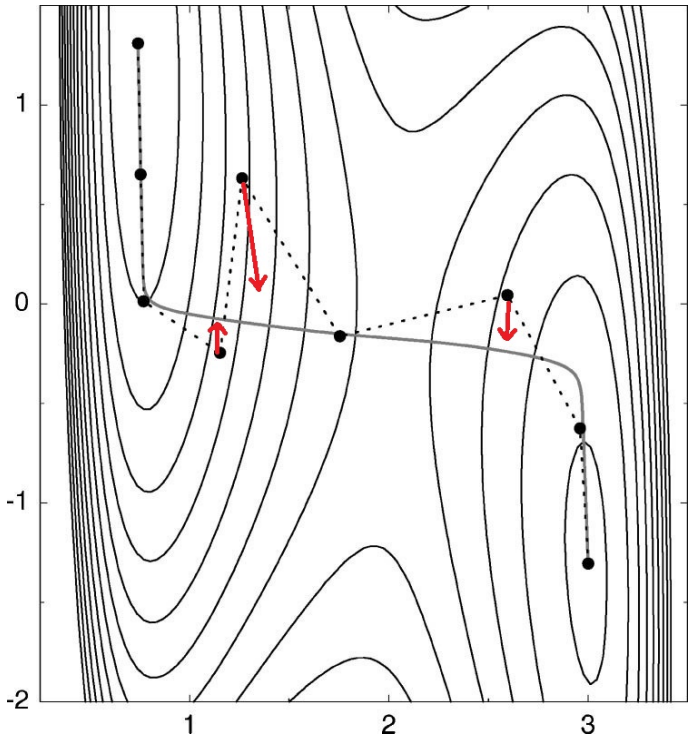


**Figure 3.6:** Schematic illustration of NEB method for finding MEP in 2-dimension. The solid line is the real MEP, and dashed line is some intermediate state during the calculation using NEB method. The dash line will eventually converge to the solid line. The arrows indicate the direction that images move. Graph is taken from [92].

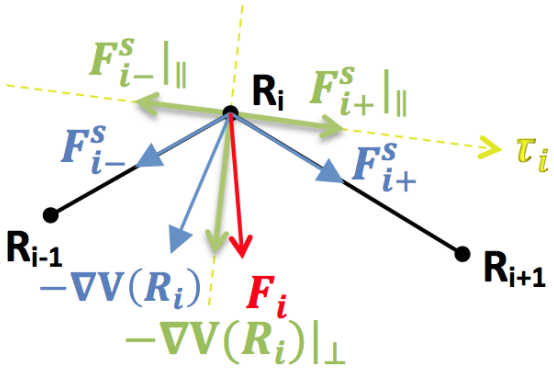


**Figure 3.7:** Force analytical graph of image $i$ in the NEB method. The yellow dashed arrow $\boldsymbol{\tau}_i$ indicates the tangent direction, the blue arrows represent forces acting on the image, and the green arrows are force projections: perpendicular component of the potential force and the parallel component of the spring force respectively. The red arrow indicates the resultant force of NEB method.

$\mathbf{R}_0$ and $\mathbf{R}_N$ are fixed and given by the energy minima corresponding to the initial and final states. The remaining $N-1$ images are adjusted by the NEB algorithm.

In the NEB method, the forces we used are force projections. A schematic illustration of these force projections is shown in Figure 3.7. The tangent at an image $i$ should be first calculated. An estimate of the tangent, which ensures the images are equispaced, are calculated from the two adjacent images,$\mathbf{R}_{i-1}$ & $\mathbf{R}_{i+1}$, along the path:

$$\boldsymbol{\tau}_i = \frac{\mathbf{R}_i - \mathbf{R}_{i-1}}{|\mathbf{R}_i - \mathbf{R}_{i-1}|} + \frac{\mathbf{R}_{i+1} - \mathbf{R}_i}{|\mathbf{R}_{i+1} - \mathbf{R}_i|} \tag{3.18}$$

then normalise $\hat{\boldsymbol{\tau}} = \boldsymbol{\tau}/|\boldsymbol{\tau}|$. The total force acting on the image is the sum of perpendicular component of the potential force and the parallel component of the spring force:

$$\mathbf{F}_i = \mathbf{F}^s_i|_\parallel - \nabla V(\mathbf{R}_i)|_\perp \tag{3.19}$$

$$\nabla V(\mathbf{R}_i)|_\perp = \nabla V(\mathbf{R}_i) - (\nabla V(\mathbf{R}_i) \cdot \hat{\boldsymbol{\tau}}_i)\,\hat{\boldsymbol{\tau}}_i \tag{3.20}$$

$$\mathbf{F}^s_i|_\parallel = k\,\{[(\mathbf{R}_{i+1} - \mathbf{R}_i) - (\mathbf{R}_i - \mathbf{R}_{i-1})] \cdot \hat{\boldsymbol{\tau}}_i\}\,\hat{\boldsymbol{\tau}}_i \tag{3.21}$$

where $V$ denotes the system energy (potential field), thus $-\nabla V(\mathbf{R})$ represents the

potential force and $k$ is the spring constant.

Then an optimisation algorithm is applied to minimise the total force $\mathbf{F}_i$ by moving the images. The images converge to the MEP with equal spacing if the spring constant is the same for all the springs.

As we know that the saddle point is the maximum of a MEP, an efficient strategy for finding a saddle point between known states is to estimate it by interpolation on the calculated MEP by NEB method. Another approach, which avoids having to run two separate optimizations or interpolates to find the saddle, is the climbing image NEB (CI-NEB).

The CI-NEB method is a small modification to the NEB method. By using CI-NEB method, one can get not only the shape of MEP, but also a point converges to the saddle point. In this method, the highest energy image $i_{max}$ feels no spring forces and climbs to the saddle via a reflection in the force along the tangent.

The CI-NEB method first follows the regular NEB algorithm for a few iterations until the image with the highest energy $i_{max}$ can be identified. Then the force on this one image is no longer given by Equation 3.19 but rather by

$$\begin{aligned}\mathbf{F}_{i_{max}} &= -\nabla V(\mathbf{R}_{i_{max}}) + 2\nabla V(\mathbf{R}_{i_{max}})|_{\parallel} \\ &= -\nabla V(\mathbf{R}_{i_{max}}) + 2(\nabla V(\mathbf{R}_{i_{max}}) \cdot \hat{\boldsymbol{\tau}}_{i_{max}})\hat{\boldsymbol{\tau}}_{i_{max}}\end{aligned} \tag{3.22}$$

Clearly, the maximum energy image (saddle point) is not affected by the spring force at all. Therefore, the spacing of the images will be different on each side of the climbing image. As it moves up to the saddle point, images on one side will get compressed, and on the other side spread out.

### 3.3.7 String Method

The string method is initially developed by W. E, W. Ren and E. Vanden-Eijnden in 2002[93] and later a simplified version is introduced[94;95]. Similarly to the NEB method, the string method also start with given initial and final states and return the saddle point and MEP.

For any image in the potential field, it would "fall" into the local minimum due to the potential force if there were no other restraints. The NEB method assumes the images are linked with elastic bands, the artificial spring force along the path prevents the images from falling into the local minimum at the ends. For the string

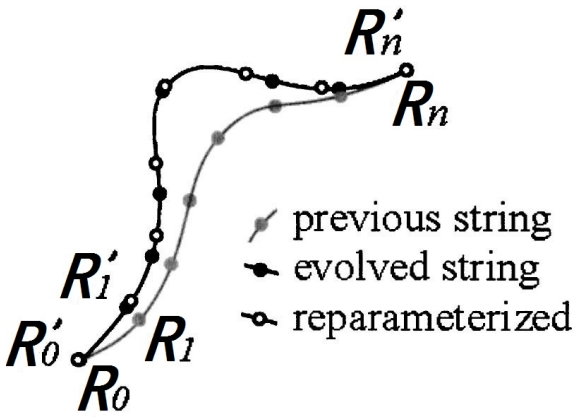


**Figure 3.8:** Schematic illustration of one iteration of the string method showing the initial string, the evolved string and the evolved string after reparametrisation. Figure taken from [94].

method, this is done by enforcing a particular parametrisation. The string method can also be viewed as the inextensible limit ($k \to \infty$) of the elastic band method, i.e. replace the elastic bands by strings in the elastic band method.

In each iteration of the string method, there are two main steps: evolution step and reparametrisation step (interpolation step). The evolution step guides the string toward the MEP, and the reparametrisation step redistributes the images along the string after each evolution step. A schematic illustration is shown in Figure 3.8.

In the evolution step, the total force acting on the image is given by

$$\mathbf{F}_i = -\nabla V(\mathbf{R}_i)|_\perp + \lambda_i \hat{\boldsymbol{\tau}}_i \tag{3.23}$$

where $\lambda_i \hat{\boldsymbol{\tau}}_i$ is a Lagrange multiplier term, which is added to enforce the particular parametrisation that we have chosen. Together with Equation 3.18 & 3.20, one can get the evolved string.

Then for the interpolation step, one can choose parametrisation by equal arc length or by energy-weighted arc length.

In the original string method, the main difficulty is in the computation of the projected force. Numerical stability requires changing the way that the tangent vector is computed before and after the saddle points are crossed. To simplify the original string method, the discrete points on the string are evolved over some time

interval $\Delta t$ according to the full potential force, i.e. replace Equation 3.23 by

$$\dot{\mathbf{R}}_i = \mathbf{F}_i = -\nabla V(\mathbf{R}_i). \tag{3.24}$$

Then Equation 3.24 can be integrated in time by any ODE solver.

During the calculation of the simplified string method, the images are first evolved and then reparametrised in every iterations. These images eventually converge to the MEP.

The simplified string method has one more advantage: the initial string can be chosen arbitrary, not necessary to be a string connects two minima.

## 3.4 Transition Search Algorithm

With the help of saddle finding methods introduced in Section 3.3, we can find possible transitions for a given state of a system. As described in Section 3.2.2, in the modified OTF-KMC algorithm, we search for saddles on defect volumes (DVs). Thus all transitions found are corresponding to DVs.

For a given state of a system, we search for possible transitions on each DVs. On each DV, the transition search algorithm used in the OTF-KMC is as follows:

**Step 1 Initial displacement:**

From the given initial search DV, randomly displace atoms which are in the initial displaceable radius.

**Step 2 Saddle search:**

Use any saddle search methods introduced in Section 3.3 to find the rank 1 saddle points.

**Step 3 Uniqueness check:**

Check the uniqueness of saddle points by calculation the separation of atoms in the DV. If the separation is larger than the threshold, discard the saddle as a duplicate.

**Step 4 Construct the final state:**

Find the final state of the transition by relaxing the system which are constructed by pushing atoms in the saddle with a displacement vector between the initial and saddle.

**Step 5 Calculate the rate:**

Use the Arrhenius Equation, Equation 3.4, to calculate the rate of the transition we found.

If any of these steps failed, the transition search is aborted as a failure. We usually launch serval hundreds of searches for each DVs, and the transition searches are performed in parallel. Once all searches on a given DV are finished, all unique transitions found are saved for reuse.

### 3.4.1 Choice of Saddle Search Method

Section 3.3 introduced several saddle finding methods. Before doing any real simulations, a suitable saddle finding method need to be chosen. It is essential to know the timing and efficiency of each method. Therefore many tests for saddle searching with different methods were performed.

To find out the efficiency of each method, we gradually increase the number of searches with the same system until the number of unique successful transitions found converges. Therefore we get the number of searches required to find most low-lying saddles for each method. At the same time, we could also get the timings for each method.

The statistical results show that the ART method is the fastest method for this problem, however the success rate for finding a low-lying saddle is extremely low, therefore require huge number of searches. The RAT method is much slower than the ART method, but the success rate is significantly improved, thus require fewer number of searches than ART. The time required for one saddle search with Dimer method has a similar time scale with RAT, and the efficiency is further improved. Therefore the Dimer method has the best overall performance for finding all low-lying saddles among the mentioned three methods. However after these single-end search methods, we still need to launch double-end search methods, namely NEB or string methods, for barrier calculating, which is another time consuming process.

The efficiency for saddle searching with the minimum mode following algorithm (MMFA) is very similar to the Dimer method. On average the MMFA method is slower than the Dimer method for saddle searching, but it is still faster than Dimer + NEB/String for calculating the barrier, as the MMFA method is able to provide an accurate barrier and does not require NEB or string methods for barrier calculating.

Therefore, the MMFA method is the overall optimal saddle searching method for my system.

In this work, the saddle searching method we use in the simulations is the MMFA method, which uses the dimer method to get closer to the saddle and uses Lanczos method for saddle convergence.

## 3.5 Reuse of Transitions

In the OTF-KMC algorithm, the most time consuming part is the saddle searching step. To reduce the simulation time and to get the most use of results from searches, in our modified OTF-KMC algorithm, we store results from searches and reuse them on the same defect volumes, which might re-appear later during the simulations. The idea of reuse of transitions is suggested by F. El-Mellouhi, N. Mousseau and L. Lewis in 2008[96], and it is implemented into the modified OTF-KMC by T. Lazauskas[86].

Therefore before reusing any of the transitions stored, the DVs need to be labelled. The labels should be able to distinguish different configurations in symmetrical or rotational point of view, i.e. the labels should be the same for isomorphic configurations but different from others. In this work, the "NAUTY" (No AUTomorphisms, Yes?) package, which is initially written by B. D. McKay[97;98], is used to generate such labels (hash keys of graphs generated from NAUTY) for DVs. If two DVs shared the same hash key, they are regarded as isomorphic.

Figure 3.9 illustrate how NAUTY assigns a hash key to a defect volume. To generate a hash key using NAUTY, we pass the positions of a group of atoms (DV) and a threshold of atomic neighbours to the NAUTY package (Figure 3.9(a)). The NAUTY package is able to find all neighbours for each atom in the DV with the given threshold, and therefore we get the connectivity between these atoms (Figure 3.9(b)). Atoms are assumed to be connected if the separation between them is less than the user defined threshold. Once we get the connectivity, a graph according to the connectivity is generated (Figure 3.9(c)) and the corresponding hash key is produced by NAUTY (Figure 3.9(d)). The hash key produced by NAUTY is unique for all the configurations which share the same connectivity graph.

If transitions found from one of the isomorphic DVs are stored, we can reuse these transitions to the other DV. The reuse algorithm is as follows:

**Step 1 Find the transformation matrix:**

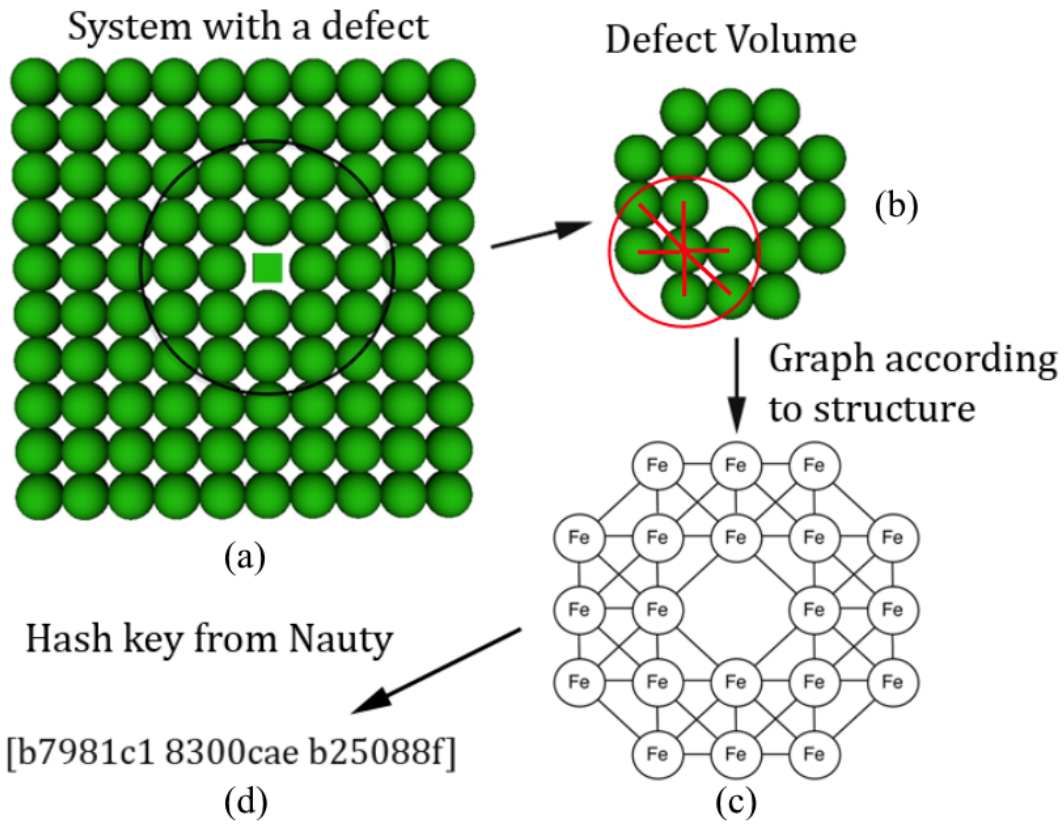


**Figure 3.9:** Schematic representation of how NAUTY assigns a hash key to a defect volume, given through a 2D vacancy example: (a) finding atoms in the defect volume, (b) finding the connectivity between atoms, (c) creating a graph according to the connectivity and (d) generating a hash key depending on the graph with NAUTY. The graph is taken from[86].

NAUTY is also used to describe the isomorphism between isomorphic DVs. The corresponding atoms between two DVs can be determined with the help of NAUTY, and the transformation matrix which transforms from one DV to the other can then be calculated.

**Step 2 Transform saddle and final states of a saved transition:**
Once we got the transformation matrix, we can transform the saved saddle and final states of transitions.

**Step 3 Apply refinements on transformed saddle and final states:**
Afterwards, the adjustment (refinement) must be applied to the transformed saddle and final states, since atoms surrounding the DV are very likely to have different configurations comparing to the original DV's.

**Step 4 Uniqueness check:**
The same as the one in the transition search algorithm, which is used to check whether the reused saddle is unique, and if not, discard it as a duplicate.

**Step 5 Calculate the rate:**
The same as the one in the transition serach algorithm, which use the Arrhenius Equation to calculate the corresponding rate of the transition.

If any of these steps failed, the reuse is aborted as a failure. The number of reuse for a given DV depends on how many transitions were saved for the DV with the same hash key. Reuse is performed in parallel with the transitions searches as well.

Once all transition searches and reuses are finished for all DVs in the current state of the system, we have a list of possible transitions from the current KMC step and can follow the KMC algorithm to next step.

# Chapter 4

# The Cadmium Telluride Lattice

Cadmium Telluride (CdTe) is a stable crystalline compound formed from cadmium and tellurium. Its applications include to be used as an infrared optical window, a highly efficient solar cell absorber material, a electro-optic modulator, an infrared detector, a radiation detector, etc.[99;100]

In this work, we modelled CdTe, as it is an excellent material for low-cost, high efficiency thin film solar cells. It is the only thin film photovoltaic technology to surpass crystalline silicon photovoltaics in the watt/cost measure and has a promising efficiency[7;8]. However the laboratory recorded efficiency of CdTe solar cells lags significantly behind the theoretical maximum for the material. This discrepancy is often attributed to defects such as grain boundaries and intra-grain dislocations[9]. Thus it is important to research how these defects are formed during the growth process and therefore reduce them. First of all, we need to understand the CdTe lattice and its properties.

## 4.1 Lattice Structure

The lattice structure of CdTe is zinc-blende structure, in which two atom types form two inter-penetrating face-centred cubic lattices. The unit cell of a zinc blende structure for CdTe is illustrated in Figure 4.1. The arrangement of atoms in CdTe is the same as diamond structure, but with alternating types of atoms such that each atom is surrounded by four opposite type of atoms.

In this work, we simulate CdTe thin film growth. All the simulations are performed on a CdTe surface. The (100) and (111) surfaces are most common types

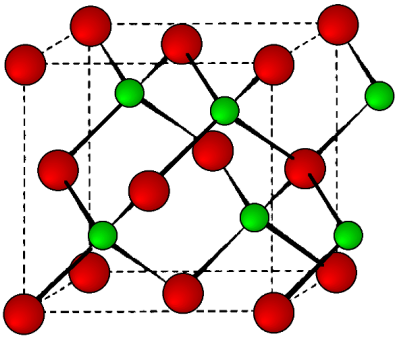

**Figure 4.1:** Unit cell of a zinc blende structure for CdTe lattice. Green smaller spheres represent the Cd atoms, and red bigger spheres the Te atoms. The dashed lines show the unit cell. Picture taken from[101].

of zinc-blende type of surfaces. There are four different CdTe surfaces used in this work for our simulations: the Cd-terminated (100) surface, the Cd-terminated (111) surface, the dimerised Te-terminated (100) surface and the Te-terminated (111) surface.

For the Te (100) surfaces there are two surface reconstruction that have been proposed, namely the $(2 \times 1)$ and the $c(2 \times 2)$, both involving Te dimerisation on the Te-terminated (100) surface[102]. We choose the $(2 \times 1)$ dimerised Te-terminated (100) surface (Figure 4.2b) for our impact simulations, because the $(2 \times 1)$ dimerisation has a lower system energy than $c(2 \times 2)$ dimerisation within our description.

Illustrations of the surfaces used in our simulations are shown in Figure 4.2. Circles and diamonds represent the two different species, and the different sizes represent the atoms in different layers. Blue areas are the smallest repeatable regions on the surface, and the impact simulations described in Section 5 are done within these regions.

## 4.2 Lattice Properties

We use the LAMMPS package, which is an open source code using classical MD, with the analytical BOP for the CdTe binary system, which is introduced in Section 2.2.3, to do all the simulations throughout this work. First, we need to test how well the potential describes CdTe by computing its lattice properties using BOP.

The CdTe material we investigate throughout this work is in zinc-blende structure. Firstly, we calculate the optimised lattice constant with BOP, and compare it

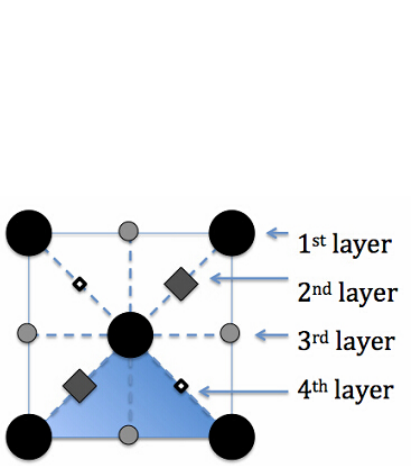


**(a)** (100) surface

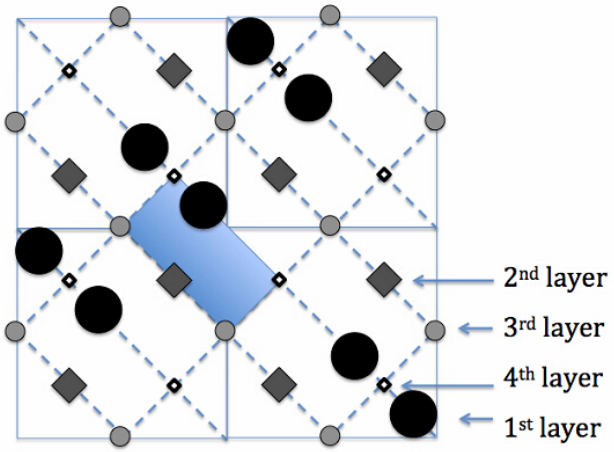


**(b)** $(2 \times 1)$ dimerised (100) surface

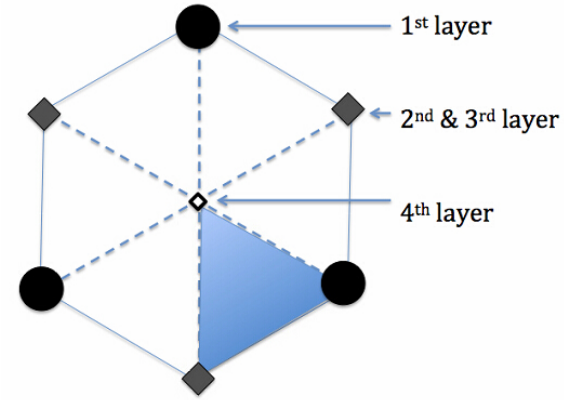


**(c)** (111) surface

**Figure 4.2:** Illustration of different surfaces used in our simulations. These graphs are top views of the first 4 layers on the CdTe surfaces. Circles and diamonds represent the two different species. Sizes represent the different layers. The shaded triangle or rectangle areas are the smallest repeatable regions on the surface. The side view of a (100) surface is exactly the same as (a), and the side view of a (111) surface is shown in Figure 4.3. The unit cell in the (100) direction is illustrated in Figure 7.21 and the unit cell in the (111) direction is illustrated in Figure 7.1

**Table 4.1:** The zinc-blende CdTe lattice constants. (Å)

| Experimental[103] | BOP | DFT[57] | SW[57] | TR[57] |
|---|---|---|---|---|
| 6.48 | 6.83 | 6.52 | 6.51 | 6.49 |

with experimental data and other potentials. We create series of lattices with different lattice constants. The lattice constant corresponding to the relaxed lattice with lowest energy is the optimal lattice constant of the chosen potential. The results are given in Table 4.1.

Secondly, the elastic constants and modulus can be calculated[104;105]. We are aiming to calculate the elastic constants, $C_{11}$ and $C_{12}$, and the bulk modulus, $B$. First we create a reference lattice with the optimal lattice constant. Then transform the primitive vectors $(a_1, a_2, a_3)^T$ of the reference lattice with a non-rotating strain tensor $\underline{\underline{\epsilon}}$:

$$(a_1', a_2', a_3')^T = (a_1, a_2, a_3)^T(\underline{\underline{\mathbf{I}}} + \underline{\underline{\epsilon}}) \tag{4.1}$$

$$\begin{pmatrix} a_1 \\ a_2 \\ a_3 \end{pmatrix} = \begin{pmatrix} 0 & a/2 & a/2 \\ a/2 & 0 & a/2 \\ a/2 & a/2 & 0 \end{pmatrix} \tag{4.2}$$

where $\underline{\underline{\mathbf{I}}}$ is the $3 \times 3$ identity matrix, $a$ is the lattice constant and the strain tensor $\underline{\underline{\epsilon}}$ is represented by a symmetric tensor with six independent components:

$$\underline{\underline{\epsilon}} = \begin{pmatrix} e_1 & e_6/2 & e_5/2 \\ e_6/2 & e_2 & e_4/2 \\ e_5/2 & e_4/2 & e_3 \end{pmatrix} \tag{4.3}$$

Relax the transformed lattice and the total energy will be changed by an amount

$$\Delta E = \frac{1}{2} V \sum_{i=1}^{6} \sum_{j=1}^{6} C_{ij} e_i e_j \tag{4.4}$$

where $\Delta E$ is the total energy change, $V$ is the volume of reference (untransformed) system and $C_{ij}$ is the elastic constants.

We can get $C_{ij}$ by varying $e_i$ and solve set of Equations 4.4. To simplify the calculations, we choose $e_1 = e_2 = \delta$, $e_3 = (1+\delta)^2 - 1$ and $e_4 = e_5 = e_6 = 0$. Then

**Table 4.2:** Elastic constants of zinc-blende CdTe lattice. (GPa)

| | Experimental[106] | BOP | DFT[107] | SW[57] | TR[57] |
|---|---|---|---|---|---|
| $C_{11}$ | 53.3 | 49.6 | 53.2 | 44.3 | 50.7 |
| $C_{12}$ | 36.5 | 31.3 | 36.0 | 19.6 | 37.5 |
| $B$ | 42.1 | 41.7 | 37.4 | 27.8 | 41.9 |

the energy change becomes

$$\Delta E(\delta) = 6VC'\delta^2 + O(\delta^3) \tag{4.5}$$

Therefore we can easily get the shear modulus $C' = (C_{11} - C_{12})$ by varying $\delta$ and applying the quadratic fittings on collected data. Similarly, we can get the bulk modulus $B = (C_{11} + 2C_{12})/3$ by choosing $e_1 = e_2 = e_3 = \delta$ and $e_4 = e_5 = e_6 = 0$ with the energy change given by

$$\Delta E(\delta) = \frac{9}{2}VB\delta^2 \tag{4.6}$$

Hence elastic constants $C_{11}$ and $C_{12}$ are given by

$$C_{11} = \frac{3B + 4C'}{3} \tag{4.7}$$

$$C_{12} = \frac{3B - 4C'}{3} \tag{4.8}$$

The comparison with experimental data and other potentials are listed in Table 4.2.

## 4.3 Point Defects

The primary point defects observed in CdTe compounds are Cd interstitials under the Cd-rich condition and Cd vacancies, Te interstitials, and Te antisites under the Te-rich conditions[108;109]. The point defects of various types can be easily introduced into our model and the defect energy, $\Gamma$, can be calculated by[110;111]

$$\Gamma = E'_D - 0.5(n_{\mathrm{Cd}} - n_{\mathrm{Te}})\Delta\mu \tag{4.9}$$

$$\Delta\mu = (\mu_{\mathrm{Cd}} - \mu^{\mathrm{bulk}}_{\mathrm{Cd}}) - (\mu_{\mathrm{Te}} - \mu^{\mathrm{bulk}}_{\mathrm{Te}}) \tag{4.10}$$

**Table 4.3:** Intrinsic defect energies $E'_D$ of various defects in zinc-blende CdTe model. (eV)

| Defect | BOP | DFT [57] | SW [57] | TR [57] |
|---|---|---|---|---|
| $V_{Cd}$ | 2.66 | 2.37 | 2.60 | 2.42 |
| $V_{Te}$ | 1.64 | 0.95 | 1.53 | 0.93 |
| $Cd_{Te}$ | 3.30 | 2.12 | 0.80 | 0.18 |
| $Te_{Cd}$ | 2.16 | 3.71 | 0.74 | 1.19 |
| $Cd_{i,Te}$ | 2.52 | 1.40 | 3.76 | 0.61 |
| $Cd_{i,Cd}$ | 2.29 | - | - | - |
| $Te_{i,Te}$ | 3.99 | - | - | - |
| $Te_{i,Cd}$ | 4.63 | 2.47 | 2.60 | 0.55 |

Defect types: $V_X$- $X$ vacancy; $X_Y$- $X$ at $Y$ antisite;
$X_{i,Y}$- $X$ interstitial surrounded by the $Y$ tetrahedron shell.
($X, Y$ represent for Cd or Te.)

where $n_X$ ($X$ represents for Cd or Te) is numbers of X atoms in the system, $\mu_X$ is the chemical potentials of X in the CdTe compound, $\mu_X^{\text{bulk}}$ is the chemical potentials for the lowest-energy X phases, and $E'_D$ is an intrinsic defect energy.

Generally, $\Delta\mu = 0$ means stoichiometric condition, $\Delta\mu > 0$ means Cd-rich condition and $\Delta\mu < 0$ means Te-rich condition. Clearly under the equilibrium condition $\Delta\mu = 0$, we have $\Gamma = E'_D$. We focus on calculating the intrinsic defect energy $E'_D$, which is given by

$$E'_D = E_D - 0.5(n_{\text{Cd}} + n_{\text{Te}})\mu_{\text{CdTe}}^{\text{bulk}} - 0.5(n_{\text{Cd}} - n_{\text{Te}})(\mu_{\text{Cd}}^{\text{bulk}} - \mu_{\text{Te}}^{\text{bulk}}) \tag{4.11}$$

where $E_D$ is the total energy of the defect system, and $\mu_{\text{CdTe}}^{\text{bulk}}$ is the chemical potential of the lowest-energy CdTe phase. Experiments indicated that equilibrium phases for Cd, Te, and CdTe are hexagonal-close-packed, $\gamma$-Se, and zinc-blende with cohesive energies of $\mu_{\text{Cd}}^{\text{bulk}} = -1.133$ eV/atom, $\mu_{\text{Te}}^{\text{bulk}} = -2.168$ eV/atom, and $\mu_{\text{CdTe}}^{\text{bulk}} = -4.356$ eV/atom, respectively [57;103].

A table of intrinsic defect energies $E'_D$ of various defects is shown in Table 4.3. The point defects listed include Cd vacancy ($V_{Cd}$), Te vacancy ($V_{Te}$), Cd at Te antisite ($Cd_{Te}$), Te at Cd antisite ($Te_{Cd}$), Cd interstitial surrounded by the Te tetrahedron shell ($Cd_{i,Te}$), Cd interstitial surrounded by the Cd tetrahedron shell ($Cd_{i,Cd}$), Te interstitial surrounded by the Te tetrahedron shell ($Te_{i,Te}$), and Te interstitial surrounded by the Cd tetrahedron shell ($Te_{i,Cd}$).

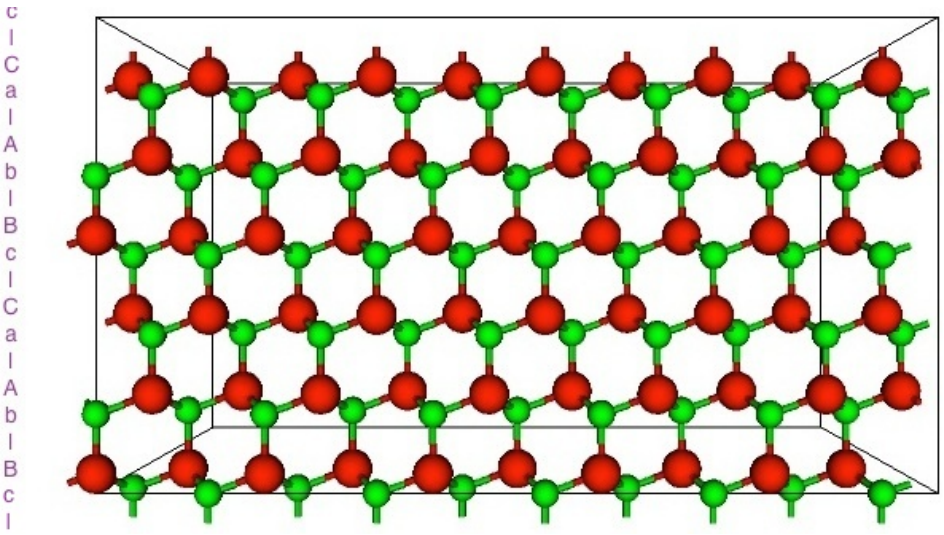


**Figure 4.3:** Stacking of a perfect zinc-blende lattice in (111) direction. Stacking sequence: $\cdots$ABCABC$\cdots$. Different colors/sizes represent different species. Vertical direction is the $\langle 111 \rangle$ direction.

## 4.4 Stacking Faults

Stacking faults are local regions of incorrect stacking of planes associated with the presence of partial dislocations. For a lattice of zinc-blende structure, in the $\langle 111 \rangle$ direction, planes of atoms are stacked in the order of $\cdots$AaBbCcAaBbCc$\cdots$ ($\cdots$ABCABC$\cdots$ for short). A graph illustrates the stacking is shown in Figure 4.3

There are three main types of stacking faults in a lattice of zinc-blende structure: (a) The intrinsic stacking fault (Figure 4.4a): an entire plane is missing. (b) The extrinsic stacking fault (Figure 4.4b): an additional plane is inserted. (c) The twin stacking fault (Figure 4.4c: part of the lattice is reflected.

In this work, we use BOP for simulations. However BOP cannot capture the formation energy of stacking faults. That's because the cut off used in the BOP is large enough for a plane to "see" its adjacent plane, but not enough to "see" the second plane. And the BOP gives the same system energy for both Wurtzite and zinc-blende structure. (Stacking sequence for Wurzite structure is $\cdots$ABAB$\cdots$) Therefore, even with stacking faults, the lattice is still locally 'perfect' in either Wurtzite or zinc-blende structure.

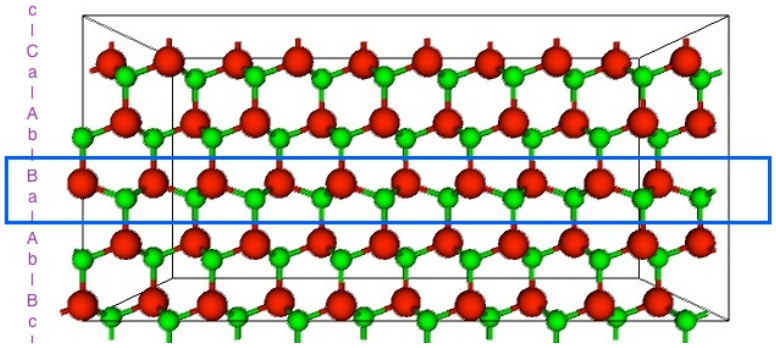


**(a)** Intrinsic Stacking Fault.
Stacking sequence: $\cdots$ABCAB|ABC$\cdots$.
An entire plane is missing.

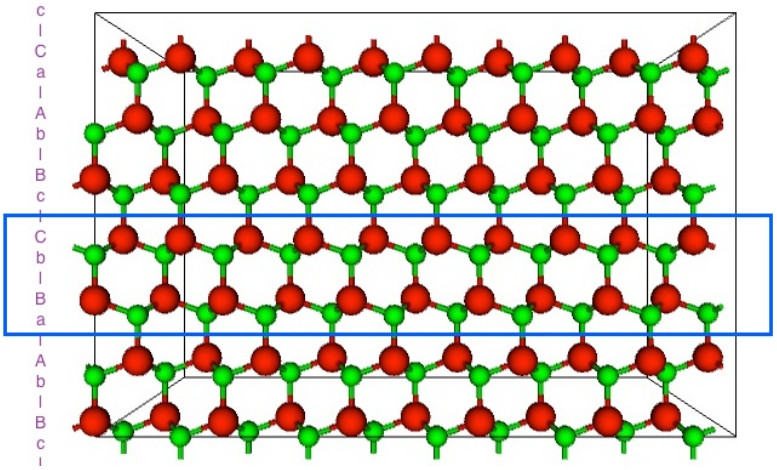


**(b)** Extrinsic Stacking Fault.
Stacking sequence: $\cdots$ABC|B|ABC$\cdots$.
An entire plane is inserted.

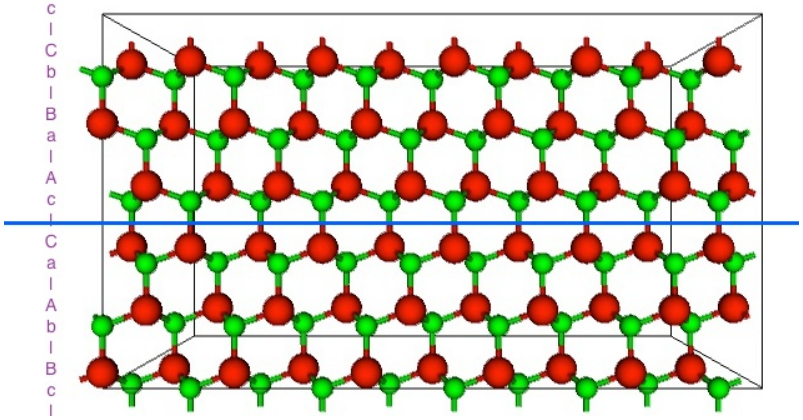


**(c)** Twin Stacking Fault.
Stacking sequence: $\cdots$CBACBA|C|ABCABC$\cdots$.
Part of the lattice is reflected.

**Figure 4.4:** Three main types of stacking faults. Vertical direction is the $\langle 111 \rangle$ direction. Coloured by species. Blue boxes indicate the stacking fault area.

## 4.5 New Deposited Layers

We found some interesting fact of the new deposited layers when we undertook the CdTe thin film growth simulations, which will be introduced in Chapter 7. New layers are formed in pairs, i.e. the new Cd layer and Te layer are formed together. And the deposited CdTe clusters do not sit on their correct sites. Therefore, it is worth calculating the energy difference of new deposited CdTe clusters sitting in different sites.

The growth simulations are done on (111) surfaces. Figure 4.2c shows sites of first 4 layers of a (111) surface. Take the Te-terminated (111) zinc-blende CdTe surface for example, diamonds represent the Cd atoms and circles the Te atoms in the graph. The first new layer should be Cd layer, and they should sit directly above the surface Te atoms. The second new layer should be Te layer, and the Te atoms should sit in the hollow site (middle) of the hexagon. We call this the 'correct site'. However the growth simulation results show that new deposited CdTe clusters always sit in the opposite sites, i.e. the Cd atoms of the first new layer sit in the hollow site and the Te atoms of the second new layer sit directly above the surface Te atoms. We call this the 'deposited site'.

First, we calculated the energy differences of small clusters at different sites. We manually insert a single CdTe cluster onto the (111) zinc-blende CdTe surface, at both the 'correct site' and the 'deposited site'. Then relax the system and calculate the system energy. We repeat the tests on both Cd- and Te-terminated surfaces. Results show that, on the Te-terminated surface, the single CdTe cluster on the 'correct site' is not stable, and it moves to a different site after relaxation (Figure 4.5b). However the single CdTe cluster on the 'deposited site' is stable and it has a lower energy than the one on the 'correct site' (Figure 4.5a). The results explain why we always observe new deposited CdTe clusters sit on 'wrong site' during the growth simulations. On the other hand, on the Cd-terminated surface, clusters on both the 'correct site' and the 'deposited site' are stable, but the cluster on the 'deposited site' has a lower energy. Figure 4.5 shows the relaxed 'deposited site' and the relaxed 'correct site' on both Cd- and Te-terminated surfaces.

Then, we want to investigate whether the situation changes when the entire new deposited layers are formed. We create a perfect (111) CdTe surface, and assume the top 2 layers are new deposited layers at the 'correct site'. Then we manually displace the top 2 layers such that they sit at the 'deposited site'. Relax both systems and

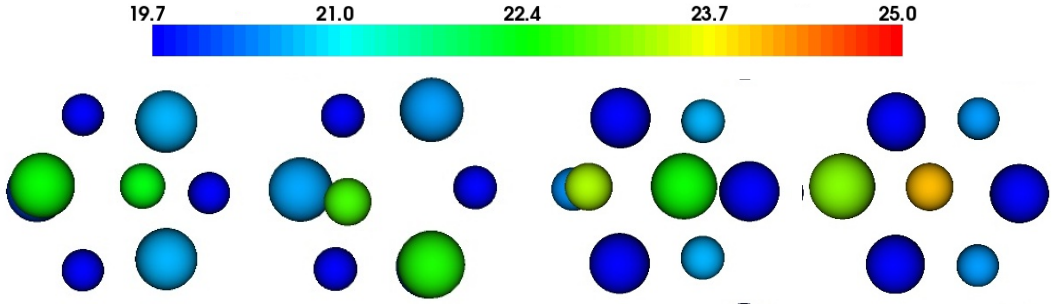


**(a)** Relaxed 'deposited site' on Te-terminated surface.

**(b)** Relaxed 'correct site' on Te-terminated surface.

**(c)** Relaxed 'deposited site' on Cd-terminated surface.

**(d)** Relaxed 'correct site' on Cd-terminated surface.

**Figure 4.5:** Relaxed surfaces with single CdTe cluster on different sites. Graphs are coloured by height. Bigger spheres represent the Te atoms, and smaller spheres the Cd atoms. Figure 4.4b is actually not at the 'correct site', it's unstable and falls to other site.

compare their total energies. The tests are done for both Cd- and Te-terminated surfaces. The results show that, the entire new deposited layers at the 'correct site' have lower total energies as we expected. The system energy of entire new deposited layers sit at the 'deposited site' are 0.22 eV/atom and 0.54 eV/atom larger than at the 'correct site' for Te- and Cd-terminated surface, respectively. We even found that, on Te-terminated surface, after relaxation, the whole layers at 'deposited site' are pulled nearer to the surface, however on Cd-terminated surface, the whole layers at 'deposited site' are pushed further after relaxation. Table 4.4 presents details data.

These tests show that the small CdTe clusters on the (111) Te-terminated surfaces will not sit at the 'correct site', however when the entire layers formed they should sit at the 'correct site' since the system energy is lower than at other sites. Therefore, the deposited clusters must diffuse from the 'deposited site' to the 'correct site' at some point before they form entire layers. This back-to-correct-site mechanism is observed during the growth simulation in Section 7.1.3.3.

**Table 4.4:** Relaxed surfaces with whole layers on different sites.

| Cd-terminated surface | | | | |
|---|---|---|---|---|
| | deposited site | correct site | difference | diff per atom |
| total energy (eV) | -2262.17 | -2347.80 | 85.63 | 0.54 |
| height +1 layer (Å) | 24.53 | 23.67 | 0.86 | - |
| height +2 layer (Å) | 25.44 | 24.63 | 0.81 | - |

| Te-terminated surface | | | | |
|---|---|---|---|---|
| | deposited site | correct site | difference | diff per atom |
| total energy (eV) | -2312.95 | -2347.85 | 34.89 | 0.22 |
| height +1 layer (Å) | 23.52 | 23.66 | -0.14 | - |
| height +2 layer (Å) | 24.23 | 24.62 | -0.38 | - |

NB: The height of layer is the average height of all atoms in the whole layer.
There are 960 atoms in the whole system, and there are 160 atoms per layer.
The +1/+2 layers in the Cd-terminated surface are Te/Cd layers, respectively.
Similarly, in the Te-terminated surface, the +1/+2 layers are Cd/Te layers, respectively.

# Chapter 5

# Single Molecule Deposition

## 5.1 Introduction

In this work, we are aiming to model the CdTe thin film growth process, and gain knowledge on how defects are formed during the growth process and therefore reduce them. Before using the LTSD, such as OTF-KMC method (Chapter 7), to model the growth process, the impact of individual $Cd_xTe_y$ $(x, y = 0, 1)$ clusters on the CdTe surfaces are performed. These energetic impact tests are helpful to understand how the atoms behave during the deposition process in different situations, and therefore to find the appropriate growth conditions[112;113].

## 5.2 Simulation Methodology

We use MD to simulate the individual energetic impact tests, which generally last for a few picoseconds (ps). The MD code we are using for the simulations is the LAMMPS package as introduced in Chapter 2.

The lattice structure of CdTe is zinc-blende. The (100) and (111) surfaces are the most common types of zinc-blende type of surfaces. In this work, we simulate the individual $Cd_xTe_y$ $(x, y = 0, 1)$ cluster impact on four different surfaces: the Cd-terminated (100) surface, the dimerised Te-terminated (100) surface, the Cd-terminated (111) surface and the Te-terminated (111) surface. Details of these four surfaces are explained in Section 4.5.

We model 12 layers of atoms, with a total of 864 atoms, for the (100) surface systems; and 6 double-layers of atoms, with a total of 960 atoms, for the (111)

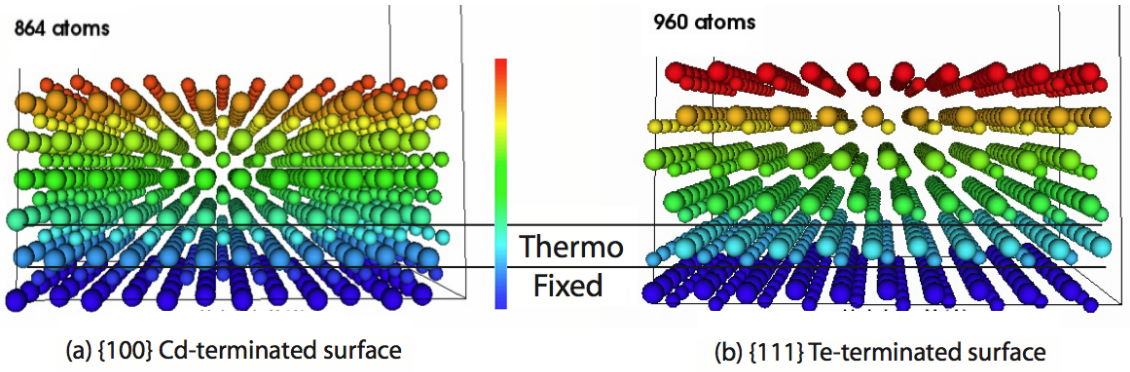


**Figure 5.1:** Front view of simulation boxes for the energetic impact tests illustrating the thermalised and fixed zone. Graph is coloured by height. Bigger spheres represent the Te atoms and smaller spheres the Cd atoms. The bottom 2 layers (or 1 double-layer) are fixed, and the next 2 layers (or 1 double-layer) above the fixed zone are thermalised.

surface systems. The bottom 2 layers (or 1 double-layer) are fixed, and the next 2 layers (or 1 double-layer) above the fixed zone are thermalised. Figure 5.1 illustrate this.

We simulate the deposition of magnetron sputtering, which is usually done at room temperature. Thus in our impact simulations, the temperature is set to be 300 K. We use the Berendsen method[61] to thermalise the system where both the heat bath coupling constant and the time step are set to be 1 fs. A single $Cd_xTe_y$ $(x, y = 0, 1)$ cluster, namely single Cd atom, single Te atom or single CdTe cluster, is deposited onto the lattice from a height of approximately 10 Å above the surface. The atom or cluster is given an velocity perpendicular to the surface, which is equivalent to be given a deposition energy of 1 eV, 10 eV, 20 eV or 40 eV. The position of deposited cluster is chosen randomly within the smallest area of each kind of surfaces (the shaded triangle or rectangle regions shown in Figure 5.2). We perform the MD simulation for 4 ps, which is enough for the temperature of the impact area to become stable after the impact and the system reach a metastable state. We then relax the system and analyse the behaviour of the deposited cluster.

We perform the impact simulations of 3 different species/clusters onto 4 surfaces with 4 different impact energies respectively, in a total of 48 cases. For each of these cases, we performed more than 1,000 impact simulations at random positions and rotations so as to sample the possible deposition positions and to collect sufficient statistics.

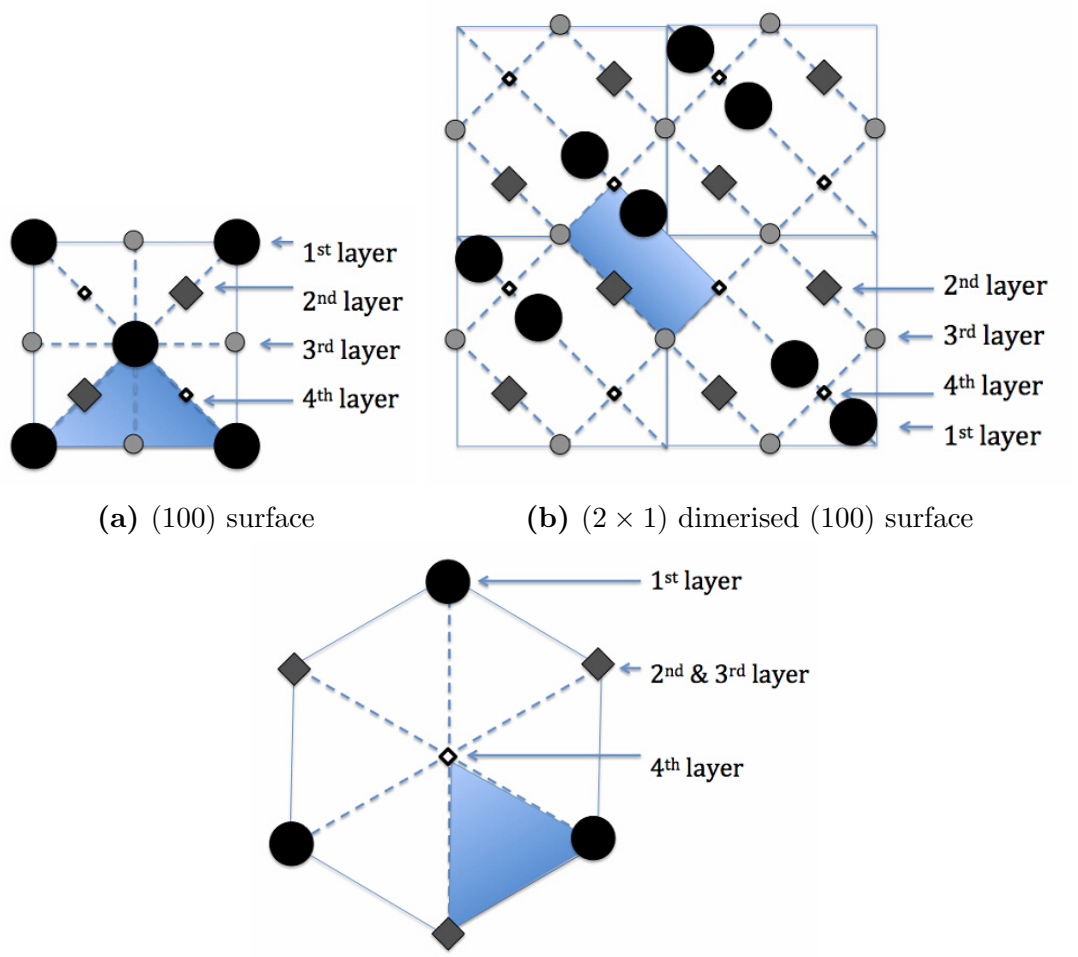


**(a)** (100) surface

**(b)** $(2 \times 1)$ dimerised (100) surface

**(c)** (111) surface

**Figure 5.2:** Illustration of different surfaces used in our simulations. These graphs are top views of the first 4 layers on the CdTe surfaces. Circles and diamonds represent the two different species. Sizes represent the different layers. The shaded triangle or rectangle areas are the smallest repeatable regions on the surface.

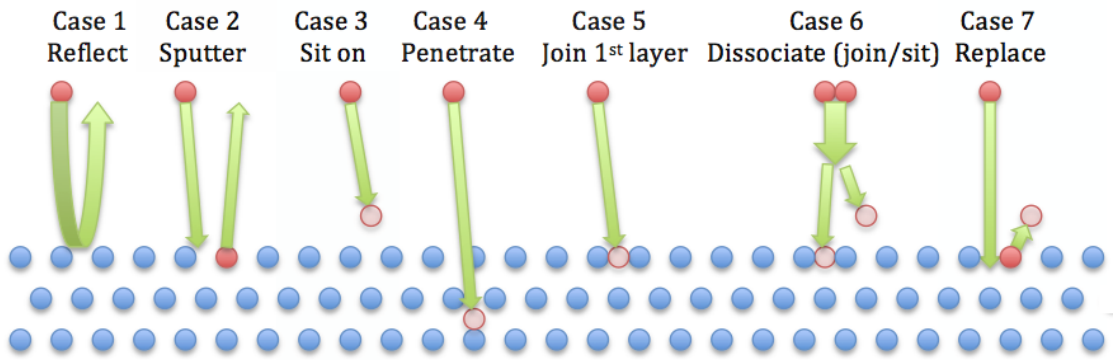


**Figure 5.3:** Illustration of 7 cases of the final states after impact.

## 5.3 Deposition Behaviours

From all the impact results, we have studied the behaviour of the deposited cluster, i.e. where the deposited cluster at the final state is and how it affects the surrounding atoms. We categorize the final states into seven cases as illustrated in Figure 5.3 and described in Table 5.1.

**Table 5.1:** Classification of impact results.

| | | |
|---|---|---|
| Case 1 | Reflect | The deposited cluster leaves the surface; |
| Case 2 | Sputter | The deposited cluster collides and other atoms are ejected from the surface; |
| Case 3 | Sit on | The deposited cluster sits on the surface as a new layer; |
| Case 4 | Penetrate | The deposited cluster penetrates the surface and becomes interstitials; |
| Case 5 | Join first layer | The deposited cluster joins the first layer and forms defects in the surface layer; |
| Case 6 | Dissociate | The deposited cluster dissociates, either joins the first layer or sits on the surfaces; (This case only occurs when depositing CdTe cluster.) |
| Case 7 | Replace | The deposited cluster replaces one of the surface atoms and pushes it onto the surface. (If depositing a CdTe cluster, this case represents the cluster dissociating and replacing a surface atom.) |

## 5.4 Simulation Results

Percentage bar charts with errors are generated for each of the 48 cases shown in Figures 5.4 and 5.5. Detailed data tables are given in Appendix B.

The results show that increasing the deposition energy typically leads to an increase in the number of atoms sputtered from the system. It also tends to decrease the number of atoms that sit on or in the surface layer, whilst increasing the number of interstitials observed.

When the CdTe cluster is deposited, if it sticks on the surface it usually dissociates at higher energies, while it prefers a soft-landing at low energies. This is not true for the (100) Te-terminated surfaces, where it also dissociates at low energies. When a single Cd/Te atom is deposited on a surface, the species of surface atoms affect the behaviour of the deposited atoms. On the surface, the probability to join the 1st layer is larger if we deposit the same species as the surface atoms than a different species. While the probability to sit on the surface is lower if we deposit the same species as the surface atoms than a different species.

The behaviours of the deposited cluster at low energies are less complex than the ones at higher energies. The deposited clusters with higher energies can penetrate the surface and displace other atoms to other sites, while the ones with lower energies usually lose their energies in the impact and stick on the surface.

The results show that, it is more difficult for the cluster to penetrate the (111) surfaces than the (100) ones. But on the other hand, it is easier to be reflected on the (111) surfaces than the (100) ones. We define that the surface is 'undamaged' if the deposited cluster is either reflected or becomes adatoms on the surface. The percentage of cases where surfaces are undamaged for the (111) surfaces is higher than the (100) ones. These facts indicate that the double-layer structure in the (111) surfaces are more stable than the single layer structure in the (100) surfaces.

For cases where the atoms leave the surface (including both reflected and sputtered), we counted the number of each species to leave the surface. The bar chart of the average number of sputtered atoms per deposition is shown in Figure 5.6. The results show that Cd atoms are more readily sputtered from the surface than Te atoms. The number of atoms sputtered from the Cd terminated surfaces is 2.5 and 5 times larger than the Te ones for the (100) and (111) surfaces respectively. They highlight that the sticking probability is higher on Te terminated surfaces than Cd ones. The ratios of the Cd atoms sputtered versus the Te atoms sputtered for the

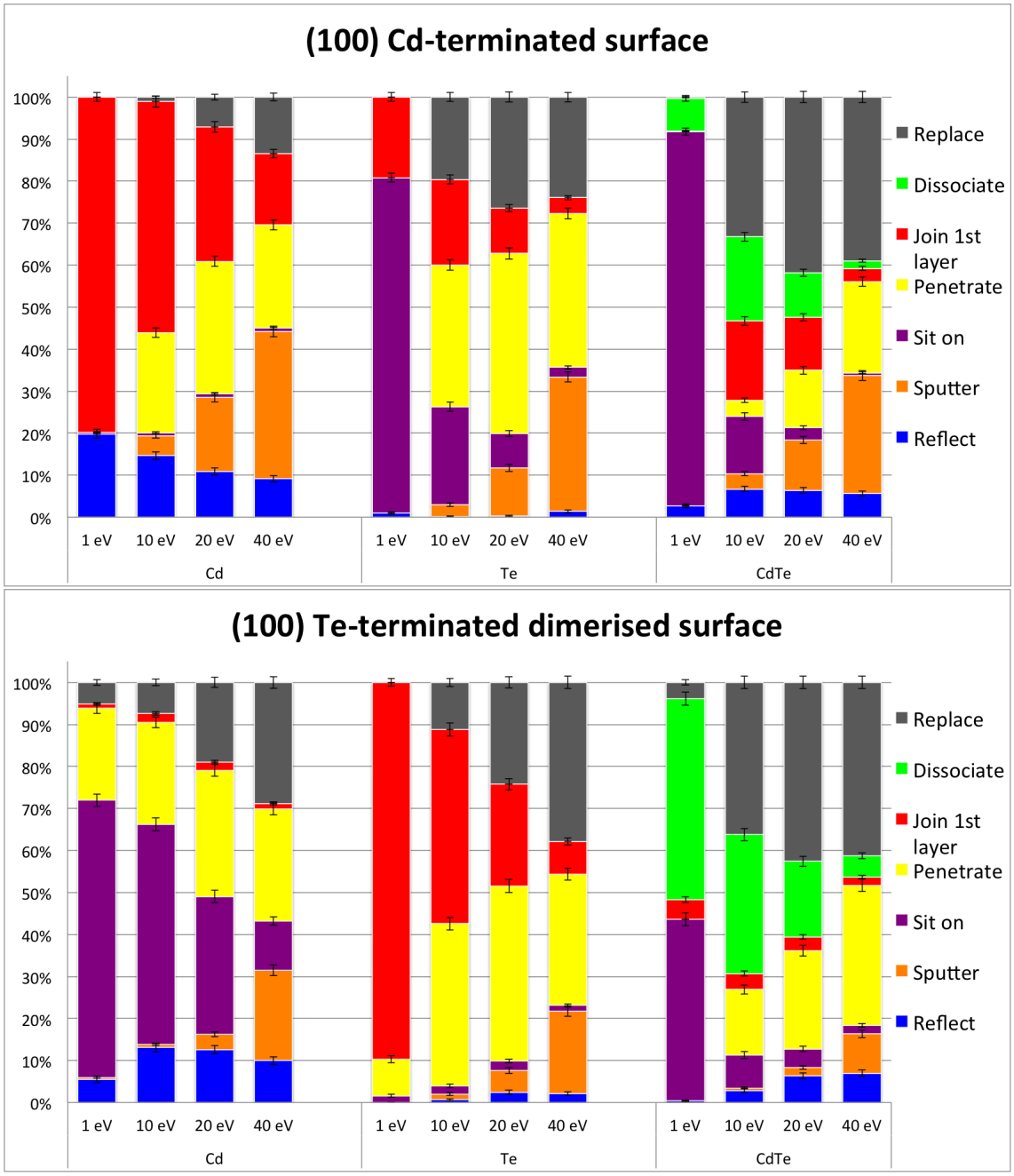


**Figure 5.4:** Energetic impact results of small $Cd_xTe_y$ $(x, y = 0, 1)$ clusters on Cd-terminated (100) and Te-terminated (100) surfaces. The 7 cases of the final states are illustrated in Figure 5.3. Error bars are on the top of each block and detailed data are given in Appendix B.

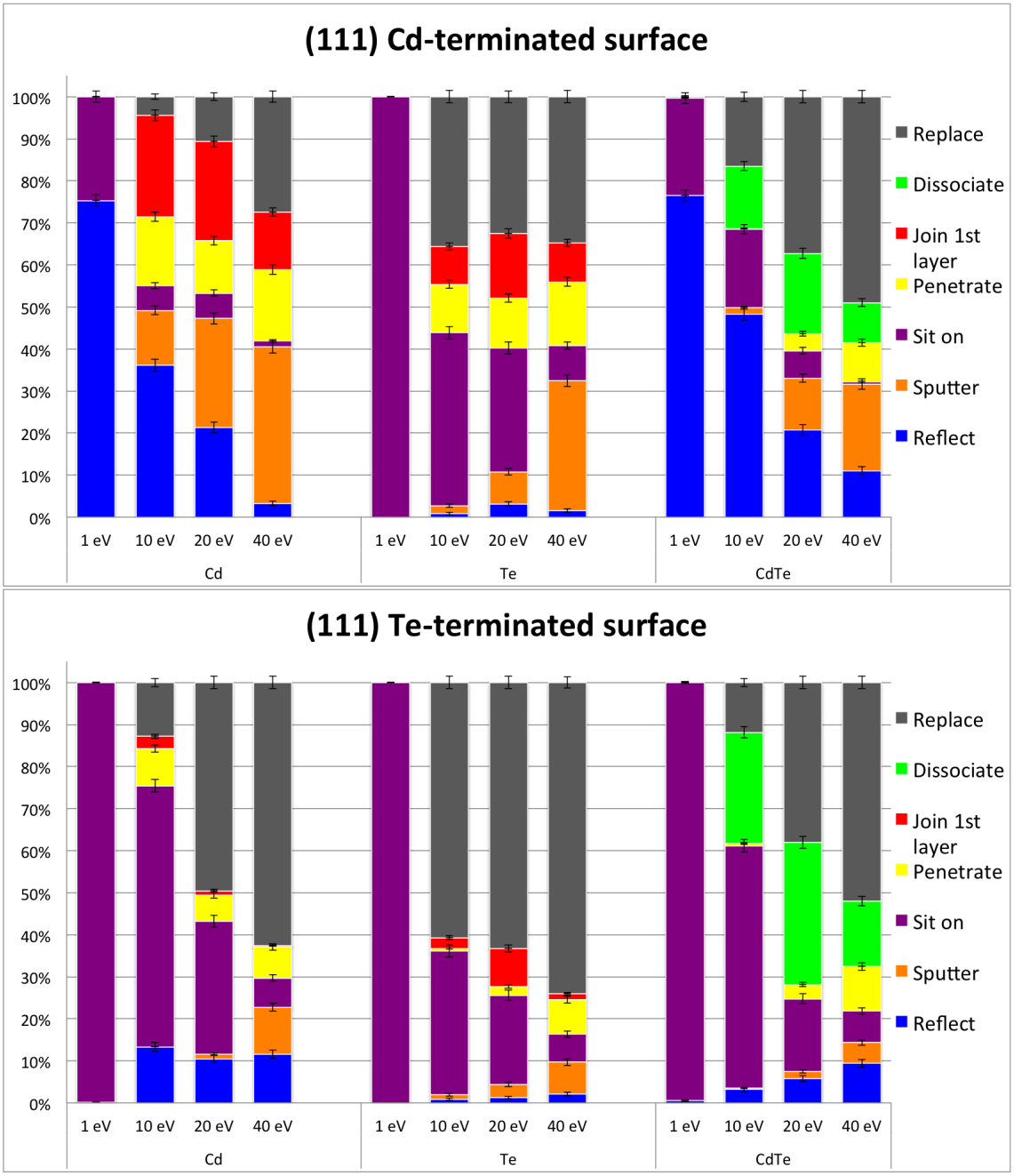


**Figure 5.5:** Energetic impact results of small $Cd_xTe_y$ $(x, y = 0, 1)$ clusters on (111) Cd-terminated and (111) Te-terminated surfaces. The 7 cases of the final states are illustrated in Figure 5.3. Error bars are on the top of each block and detailed data are given in Appendix B.

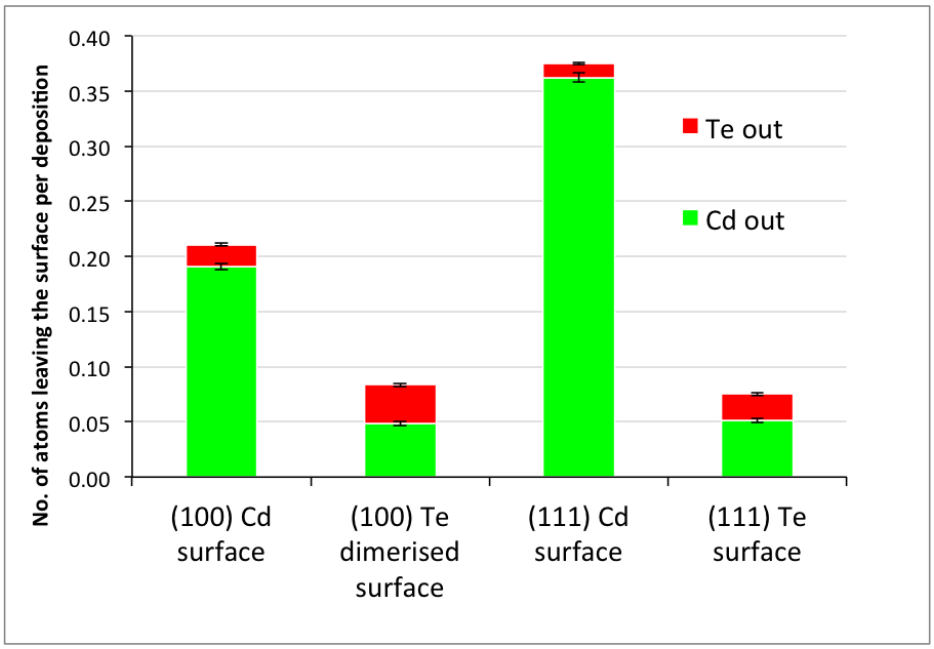


**Figure 5.6:** Average number of atoms leave the surfaces per deposition.

Te terminated surfaces (1.4 for (100) surface and 2.1 for (111) surface) are much smaller than the ratios for the Cd terminated surfaces (9.5 for (100) surface and 28.3 for (111) surface).

## 5.5 Conclusions

The energetic impact simulations of small $Cd_xTe_y$ $(x, y = 0, 1)$ clusters onto the (100) Cd and Te terminated surfaces and (111) Cd and Te terminated surfaces at 1, 10, 20 and 40 eV have been simulated.

The results show that Cd atoms are more readily sputtered than Te atoms, especially on the Cd-terminated surfaces. The deposited clusters are more likely to be reflected than sputtered at lower energies. The sticking probability is higher for the Te-terminated surfaces than the Cd-terminated ones. This explains why the growth rate decays when the Cd concentration increases in the vapor as indicated in the work of C. Ferekides using elemental vapour transport at atmospheric pressures [114].

The results also show that (100) surfaces are more likely to be penetrated or create interstitials in the surface layer than (111) surfaces. There are high possibilities for the deposited cluster to sit on the surface at low energies, and the CdTe cluster usually dissociates and replaces surface atoms when deposited onto the surfaces.

We do not observe CdTe growth mechanisms from the energetic impact simulations. It's not clear from the impact simulations alone how further layers of CdTe would grow. Further work using LTSD simulations to gain knowledge of the growth process of CdTe surfaces are presented in Chapter 7.

# Chapter 6

# Superbasin Method

## 6.1 Introduction

We are aiming to model the growth of CdTe thin films by using the OTF-KMC method, which is introduced in Section 3.2.2. In each step of OTF-KMC method, the algorithm needs to determine what to do – whether execute a transition for the diffusion process or switch to MD for doing a deposition – with respect to their corresponding rates. The deposition process deposits the target materials onto the base, therefore we get more atoms on the thin films. The diffusion process allows the deposited atoms to move around on the surface. It helps to form big clusters and eventually the whole layer. Therefore we get the thin films growing. During the simulations, we want to reduce the computing time on the repeated meaningless diffusions while keep the right distribution of simulation time, thus more depositions occur in the simulations, therefore accelerate the whole growth simulations.

In the OTF-KMC simulations, the algorithm starts with searching for all possible transitions (saddles) from current state, and then randomly select one of the transitions to execute according to their corresponding rates. The rates are calculated with respect to their barriers using the Arrhenius Equation $R = \nu \exp(-\Delta E/k_B T)$, where $\Delta E$ is the barrier height. The lower the barrier of a transition is, the higher the rate is. Sometimes during the simulations, there are several states which are connected to each other with low-barrier transitions and the transitions to other states have higher barriers. Once the simulation goes into these low-barrier-connected states, it is very likely for the simulation to be "trapped" into these low-barrier-connected states, because low-barrier transitions have higher probabilities to be chosen than

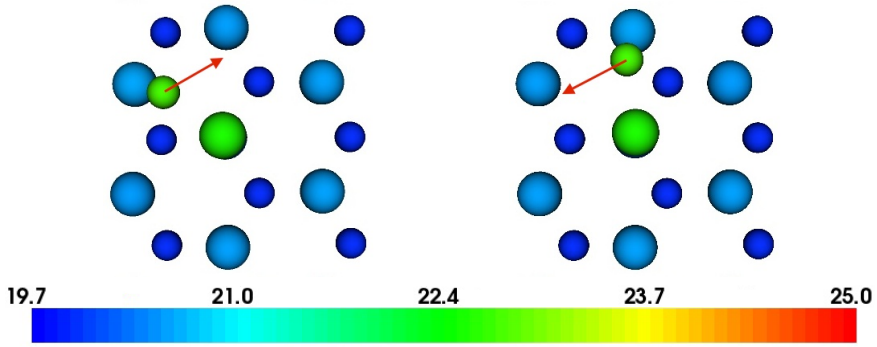


**Figure 6.1:** An example of flickering between two states on CdTe surface. The barriers between these two states are ∼0.02 eV [0.2 ps at 350 K]. The barriers of transitions to other states are normally larger than 0.27 eV [0.7 ns]. Graphs are coloured by height. Bigger spheres represent the Te atoms, and smaller ones the Cd atoms.

other transitions (the escaping transitions). As a result the simulation will spend a very long time in computing these repetitive transitions between these states, and we want to get rid of this situation.

## 6.2 Low-Barrier Problems

As described above, if there are several states which are connected by low-barrier transitions and the escaping transitions have higher barriers, the standard OTF-KMC method will be "trapped" into these states for a very long time, which is a waste of computational time. In our CdTe thin film growth simulations with standard OTF-KMC method, we found many cases of states as described above. The simulation results also show that the simulations are indeed "trapped" in these states for significant computational time with no progress.

Several examples of low-barrier transitions between states are shown in Figure 6.1∼6.3. The corresponding high barrier transitions is illustrated later in Section 7.1.3.2. In these examples, the barriers of transitions within these states are much lower than ones of escaping transitions. Therefore the simulations are very likely to be trapped in these states, because of the high possibility of choosing these low-barrier transitions.

There are two main downsides for OTF-KMC dealing with states connected with low-barrier transitions problems. First, selected low-barrier transitions limit

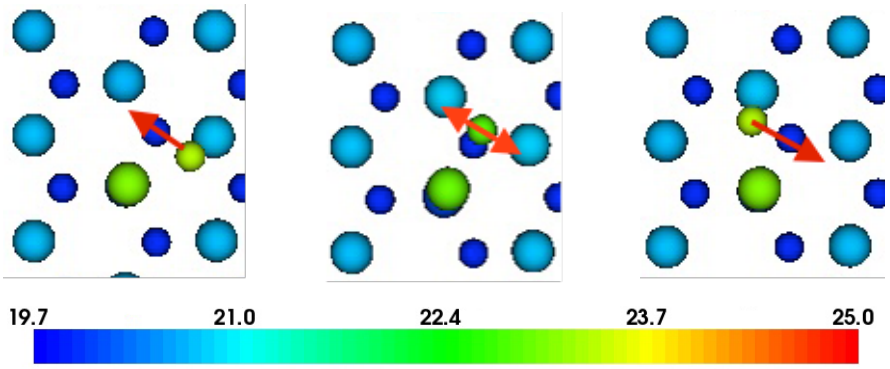


**Figure 6.2:** Flicker between 3 meta-stable states with low barriers. The barriers between these states are 0.14∼0.27 eV [0.01∼0.7 ns]. The barriers of transitions to other states are normally larger than 0.3 eV [2 ns]. Graphs are coloured by height. Bigger spheres represent the Te atoms, and smaller ones the Cd atoms.

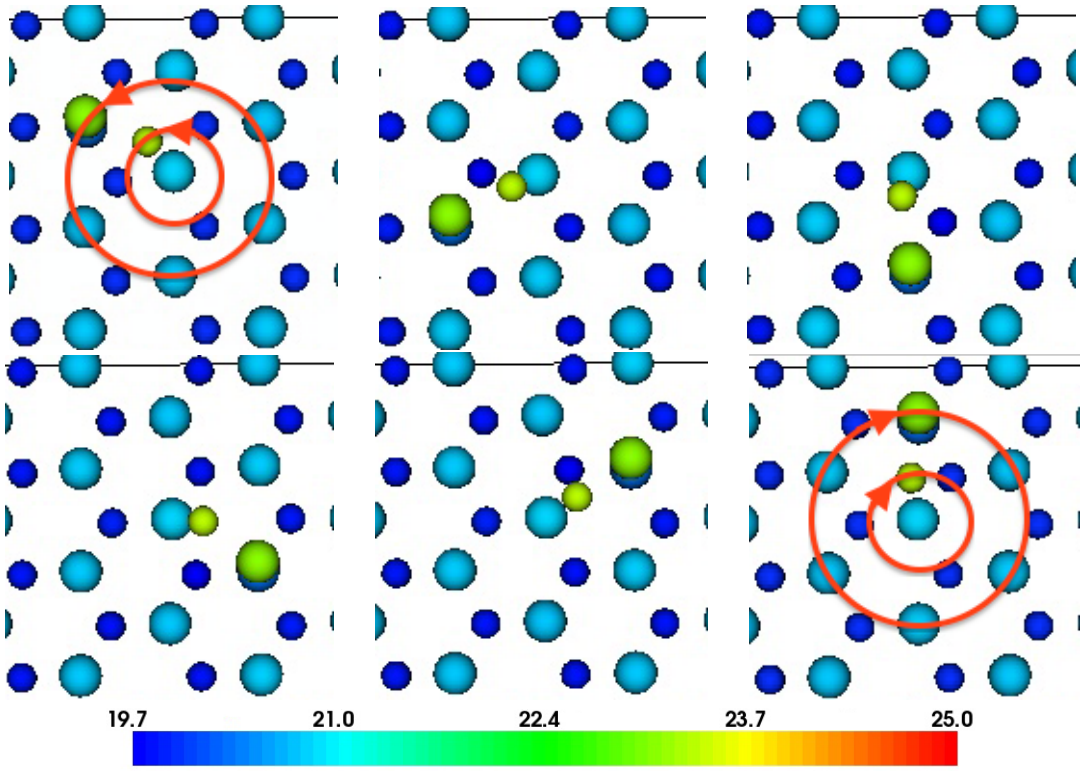


**Figure 6.3:** Replica surrounding states. The barriers between these states are 0.15 ∼ 0.3 eV [0.014∼2 ns]. The barriers of transitions to other states are normally larger than 0.3 eV [2 ns]. Graphs are coloured by height. Bigger spheres represent the Te atoms, and smaller ones the Cd atoms.

the attainable simulation time due to corresponding high rates. It is known that the time step in KMC is given by $\Delta t = -\ln u / \sum_i R_i$, where $R_i$ is the rate for each transition and the summation is over all possible transitions. Clearly the time step $\Delta t$ is dominated by the lowest barrier transition as it has the largest rate. The low-barrier transitions between such states have large rates, thus limit the time step in KMC, therefore limit the total attainable simulation time. Second, OTF-KMC are trapped in certain states, therefore lots of computing resources are spent in exploring the same states for many times without yielding much information. All we get are repetitive "flickering" among certain states.

A way of solving this kind of problem is to regard all these low-barrier-connected states as one object – a superbasin, therefore all low-barrier transitions within these states are gone while all escaping transitions are still kept. This is the key idea of superbasin-based acceleration schemes.

## 6.3 Superbasin Model

The superbasin method is developed to integrate out of low-barrier transitions within the low-barrier-connected states while keep the escaping transitions, therefore accelerate the simulations. The idea of the superbasin method is very simple. We consider all states connected by low-barrier transitions are belonged to a superbasin. Any transitions between these superbasin states are not allowed to be chosen in the KMC selection, i.e. once the system enters the superbasin, no superbasin states are revisited and the algorithm only allows to escape from the superbasin. A simple 1-D example is illustrated in Figure 6.4.

The superbasin method deals with these low-barrier problems by constructing a superbasin, which consists of low-barrier-connected states. In the superbasin model, there are two types of states: transient states and absorbing states. A state is a transient state if a transition between it and a neighbouring transient state has a barrier which is less than the user defined threshold $E_{\min}$ (the low-barrier-connected states, State 2 & 3 in Figure 6.4). A state is an absorbing state if all transitions between it and a neighbouring transient state have barriers which are larger than $E_{\min}$ (the escaping states, State 1 & 4 in Figure 6.4). There are three types of events (transitions) in the superbasin model: potential event, basin event and ordinary event. A transition is called a potential event, if the transition has a barrier which is

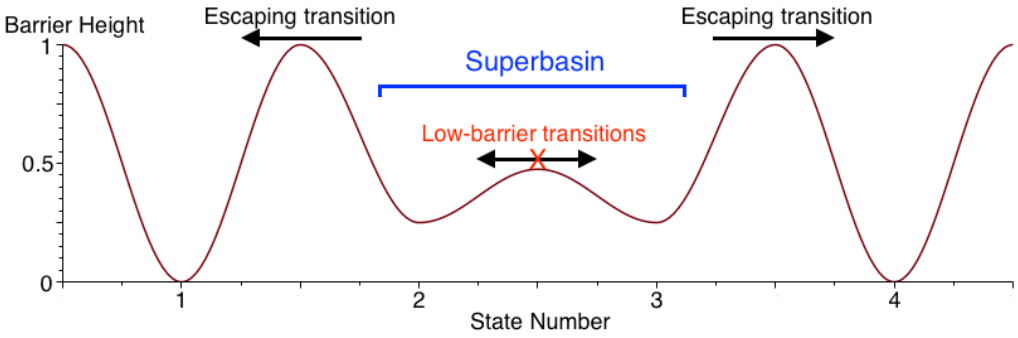


**Figure 6.4:** A one-dimensional example of superbasin method. State 2 & 3 are connected with low-barrier transitions and they form a superbasin. Once a trajectory enters the basin (either in state 2 or 3), transformations between state 2 & 3 are not allowed, and the only paths allowed to be chosen are escaping transitions to state 1 or 4.

lower than $E_{\min}$. A transition is called a basin event, if the transition is a potential event and it has been selected/executed in the KMC routine. All other transitions are called ordinary events, i.e. escaping transitions which have barriers are larger than $E_{\min}$.

On the one hand, the superbasin method is designed to escape the superbasin as soon as possible, thus all basin events are not allowed to be selected, therefore no transient states are visited twice. On the other hand, the superbasin method should give the right distribution of escaping time without altering the evolution of the system, thus we use the mean rate method (MRM) to adjust the rates for all transitions in the superbasin model.

## 6.4 Previous Work

To solve the low-barrier problems, L. K. Béland et al. developed the basin-auto-constructing mean rate method (bac-MRM) in 2011 [115], and later K. A. Fichthorn et al. developed the local superbasin KMC (LS-KMC) method in 2013 [116]. Both methods are inspired by the mean rate method (MRM) implemented by B. Puchala, M. L. Falk and K. Garikipati in 2010 [117].

Both bac-MRM and LS-KMC methods share the same superbasin model. The transitions found in both methods are with respect to the whole system, thus they need to identify whether the atomic movements in the transitions belong to the existing superbasin or not. The main differences between two methods are that the

bac-MRM method calculates the average escaping time and corresponding rates for each individual escaping transitions (ordinary events), while the LS-KMC method only calculates the average escaping time for each escaping states (absorbing states). In other words, the bac-MRM cares about how to escape the superbasin, while the LS-KMC only cares about where it finally escapes to.

### 6.4.1 Basin-Auto-Constructing Mean Rate Method

The bac-MRM is suggested by L. K. Béland, P. Brommer, F. El-Mellouhi, J.-F. Joly and N. Mousseau in 2011 [115]. It is able to calculate the mean rate of each individual escaping transition from a specific transient state, and the exact probability of exiting to each absorbing state without also calculating the full time distribution.

The bac-MRM builds the superbasin on the fly. The transitions found in the normal KMC step are categorised into three events mentioned above. The basin events are not allowed to be selected in the model. If the selected event is a potential event, one more transient state is appended to the superbasin. If the selected event is an ordinary event and it belongs to an existing superbasin, i.e. the selected transition escapes from the superbasin, the superbasin is discarded. Thus the key to the superbasin model is how to calculate the escaping probabilities.

To determine the probability to exit the basin to an absorbing state, we calculate the transition probability matrix $\underline{\mathbf{T}}$, with components

$$T_{ji} = \frac{R_{i\to j}}{\sum_k R_{i\to k}} = \tau_i^1 R_{i\to j} \tag{6.1}$$

$$\tau_i^1 = \frac{1}{\sum_k R_{i\to k}} \tag{6.2}$$

where $R_{i\to j}$ is the rate going from transient state $i$ to transient state $j$, and the summation is over all transient and absorbing states k. $\tau_i^1$, the reciprocal of the sum of all rates leaving state $i$, is the mean residence time in state $i$ each time it is visited.

The occupation probability vector, $\mathbf{\Theta}(m)$, which gives the probability of being

in any transient state after jump $m$ and before jump $m+1$, is given by

$$\mathbf{\Theta}(m) = \underline{\mathbf{T}}^m \mathbf{\Theta}(0) \tag{6.3}$$

$$\Theta_i(0) = \begin{cases} 1 & \text{if state } i \text{ is the initial state} \\ 0 & \text{otherwise} \end{cases} \tag{6.4}$$

Summing the occupation probabilities over all possible numbers of jumps gives:

$$\mathbf{\Theta}^{sum} = \sum_{m=0}^{\infty} \underline{\mathbf{T}}^m \mathbf{\Theta}(0) = (\underline{\mathbf{I}} - \underline{\mathbf{T}})^{-1} \mathbf{\Theta}(0) \tag{6.5}$$

The mean residence time in transient state $i$ before leaving the basin is given by

$$\tau_i = \tau_i^1 \Theta_i^{sum} \tag{6.6}$$

which are used to accelerate the rates of exiting to absorbing state $j$ from transient state $i$,

$$\langle R_{i \to j} \rangle = \frac{\tau_i}{\sum_k \tau_k} R_{i \to j} \tag{6.7}$$

where $k$ summing over all transient states.

The next KMC step is then determined using normal KMC selection rules with these accelerated rates. Finally, the mean escape time, which is used for the KMC timestep is given by

$$\langle t_{exit} \rangle = \sum_i \tau_i \tag{6.8}$$

The basin events are designed not to be selected, thus rates for these transitions are forced to be zero. During the construction of superbasins, the final state of a potential event is not in the built superbasin yet, thus the rates for these transitions are calculated the same way as the escaping transitions mentioned above.

### 6.4.2 Local Superbasin KMC method

The LS-KMC method is developed by K. A. Fichthorn and Y. Lin in 2013[116]. The method does not calculate escaping probability and time for each individual

escaping transitions. Instead, it gives the escaping probability and time when the system escapes to an absorbing state.

The LS-KMC method builds superbasins after the completion of searching for transitions in a normal KMC step. If an existing superbasin is detected to be changed, the superbasin need to be wrecked or revised. If a new superbasin is needed, corresponding escaping probability and time is calculated.

The LS-KMC method accelerate rates by using the theory of absorbing Markov chains. Different from the bac-MRM, in the LS-KMC method, the constructed superbasin not only contains the transient states, but also contains absorbing states. First create a Markov matrix $\underline{\mathbf{M}}$ to describe transitions among the transient and absorbing states comprising the superbasin. Re-ordering the states so that the absorbing states are first, followed by the transient states, the Markov matrix is defined as

$$M_{ij} = \begin{cases} 1 & \text{if } i = j = \text{absorbing} \\ 0 & \text{if } i = j = \text{transient} \\ \tau_i^1 R_{i \to j} & \text{if } i \neq j \end{cases} \tag{6.9}$$

where $\tau_i^1$ is given by Equation 6.2, which implies the average escape time from state $i$. The Markov matrix can be written in the general form

$$\underline{\mathbf{M}} = \begin{pmatrix} \underline{\mathbf{I}} & \underline{\mathbf{0}} \\ \underline{\mathbf{R}} & \underline{\mathbf{T}} \end{pmatrix} \tag{6.10}$$

where $\underline{\mathbf{I}}$ is the identity matrix, $\underline{\mathbf{0}}$ is the null matrix, $\underline{\mathbf{R}}$ is the recurrent matrix, and $\underline{\mathbf{T}}$ is the transient matrix which is the transpose of the transition probability matrix defined by Equation 6.1.) If there are $a$ absorbing states and $t$ transient states in the basin, then $\underline{\mathbf{I}}$ has rank $a$, $\underline{\mathbf{T}}$ has rank $t$, and $\underline{\mathbf{R}}$ is a $(t \times a)$ matrix.

For a given initial occupancy of the transient states, $\boldsymbol{\Theta}(0)$ defined by Equation 6.4, the average time to perform $n+1$ steps is given by

$$\langle t_{n+1} \rangle = \boldsymbol{\Theta}(0)^T \cdot \underline{\mathbf{T}}^n \cdot \boldsymbol{\tau}^{\mathbf{1}}. \tag{6.11}$$

Summing over all $n$, we will get the average exit time as

$$\langle t_{exit} \rangle = \boldsymbol{\Theta}(0)^T \cdot (\underline{\mathbf{I}} - \underline{\mathbf{T}})^{-1} \cdot \boldsymbol{\tau}^{\mathbf{1}}, \tag{6.12}$$

which is used for the KMC timestep and is the same as Equation 6.8. After identifying $\langle t_{exit} \rangle$, we need to choose a particular absorbing state $i$.

Different from bac-MRM, the LS-KMC method doesn't calculate the rates for each individual transitions, it only gives the probability of being at a certain absorbing state $i$. The probability vector that the system will end up in the absorbing states is given by

$$\boldsymbol{\pi}^a = \boldsymbol{\Theta}(0)^T \cdot (\underline{\mathbf{I}} - \underline{\mathbf{T}})^{-1} \cdot \underline{\mathbf{R}} \tag{6.13}$$

Then the normal KMC selection algorithm is applied to determine where the system evolves to.

Both the bac-MRM and the LS-KMC methods are able to get rid of the repetitive "flickering" among the low-barrier-connected states by building superbasins. Both methods are able escape the superbasins quickly without altering the evolution of the system by adjusting the rates of transitions. The two methods adjust the rates/probabilities of escaping transitions in two different ways. The bac-MRM method calculates the modified rates for each individual escaping transitions, while the LS-KMC method only calculates the escaping probabilities for escaping to each absorbing states.

The biggest advantage in the bac-MRM method is that the algorithm builds the superbasins on the fly, only as far as necessary. It does not require to know all information about the whole superbasin. However the bac-MRM method can only build one superbasin at one time for the whole system. If there are multiple low-barrier transitions at different places in the lattice, i.e. there are multiple potential superbasins in the system, the bac-MRM method will not work properly as it is designed to build one superbasin.

The LS-KMC method also works on the whole system. The biggest advantage in this method is that the LS-KMC method does extra work on identifying whether the atomic movements belong to existing superbasins or not, therefore it is able to handle multiple superbasins in the system. However the LS-KMC method requires to know all the transitions related to the superbasins in advance, which means the superbasins can only be built after finding all the low-barrier transitions. This requires a lot of memory, because all informations in the past a few KMC steps need to be kept in memory before the whole superbasin is built.

## 6.5 Implementation into OTF-KMC

The bac-MRM and LS-KMC method have their advantages and limitations. We want to combine their advantages and eliminate their limitations. I implemented the superbasin method into the OTF-KMC algorithm, so that the superbasin method can build multiple superbasins in the system as the LS-KMC method, and build the superbasins on the fly as the bac-MRM method.

As described in Section 3.2.2, transitions found in the OTF-KMC method are with respect to defect volumes, not the whole system. Thus superbasins built in the OTF-KMC are with respect to defect volumes as well. Therefore, the identification of transitions belong to superbasins becomes the identification of transitions relate to defect volumes in the superbasins. There are usually multiple defect volumes in a system, thus multiple superbasins built in a system is plausible. We also use the idea of bac-MRM to build superbasins on the fly, and use Equation 6.7 to calculate the accelerated rates for each individual escaping transitions.

There are several difficulties to overcome when I implement the superbasin method into the OTF-KMC method. Because we want to build the superbasins on the fly as the bac-MRM does, we need to identify whether the selected transition has a low barrier or not. But to only check the forward barrier of the transition is not enough, we need also check its reverse barrier. Figure 6.5 illustrates a one-dimensional example of a superbasin with 3 states. The bac-MRM method only regards a transition with both forward and reverse barriers less than the threshold $E_{\min}$ as a basin event (transitions between state 3 & 4). Thus in this example, the superbasin only consists of state 3 & 4. State 2 is not in the superbasin because the transition from state 3 to 2 has a higher barrier. It is possible to escape the superbasin to state 2. And clearly it is very likely to fall back to the superbasin again, as transition from state 2 to 3 has a low barrier. Therefore we decide to build a larger superbasin with state 2 included as well. Thus in our superbasin method, a basin event is defined as a transition with either a low forward barrier or with a low reverse barrier or with both forward and reverse low barriers.

The inclusion of transitions with a high backward barrier in a superbasin does not change the dynamics of the system, but saves time by not constructing the same superbasin again. Take the case shown in Figure 6.5 for example. If we have built a superbasin with state 3 & 4, it is likely that the system will go to state 2 as the escaping barrier is higher. If we do not include state 2 as a superbasin state, the

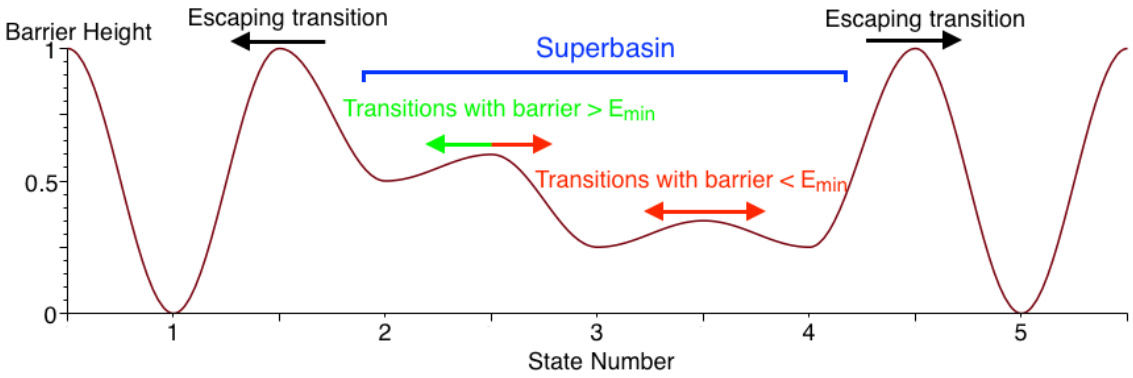


**Figure 6.5:** A one-dimensional example of superbasin. A one-dimensional superbasin consists of state 2, 3 & 4. State 3 & 4 are connected with low-barrier transitions. Transition from state 2 to 3 has a low barrier, while the reverse transition has a higher barrier. Red arrows indicate low-barrier transitions in the superbasin, i.e. transitions with barriers $\Delta E < E_{\text{min}}$. Green arrows represent transitions with barriers $\Delta E > E_{\text{min}}$ in the superbasin. Black arrows indicate the escaping transitions.

superbasin with state 3 & 4 will be discarded due to the exit of superbasin. However when the system is in state 2, there is a high possibility for the system to go back to state 3, which belongs to a superbasin. If this is the case, we have to explore state 3 & 4 again and build the same superbasin before entering state 2, which is not efficient. Therefore the inclusion of state 2 in the superbasin saves time by not constructing the same superbasin again. On the other hand, if we included state 2 into the superbasin, the dynamics of the system would not change. After applying the MRM to correct all rates for escaping transitions, generally all escaping rates are scaled down. The scaling factor is proportion to the mean resident time in each superbasin state (Equation 6.6). Because the transition from state 3 to 2 has a larger barrier than other low-barrier transitions, the mean resident time in state 2 is much less than in state 3 & 4. For example if the rates for all low-barrier transitions are 500 $s^{-1}$ (red arrows in Figure 6.5), the rate for the high backward barrier is 100 $s^{-1}$ (green arrows in Figure 6.5) and the rates for two escaping transitions are 2 $s^{-1}$ (black arrows in Figure 6.5). By the MRM, the mean resident time in state 2 is 5 times less than in state 3 & 4 as expected. Therefore the corrected rate for the escaping transition from state 2 to 1 is 5 times smaller than the one from state 4 to 5. I.e. in this example, the system is 5 times more likely to escape the superbasin from state 4 to 5. If we do the same calculation for the case where state 2 is not

included in the superbasin, the rate for escaping transition from state 2 to 1 is still 5 times smaller than the one from state 4 to 5. This confirmed that the dynamics of the system not changed by including state 2 into the superbasin.

Similar to the LS-KMC method, our superbasin method is able to build multiple superbasins. To build multiple superbasins in a system, we need to know whether the selected transition belongs to existing superbasins or not, and which superbasin it belongs to. The OTF-KMC method dealing transitions with respect to defect volumes in the system. Our superbasin method build superbasins with respect to defect volumes as well. We use a hash key generated by NAUTY to identify the topology of a defect volume, and use center of mass and moment of defect volume to identifyocation of the defect volume in the system. By using this information, it is easy to determine whether a selected transition belongs to existing superbasins or not, and which superbasin it belongs to. This allow us to know whether the selected low-barrier transition to be appended to an existing superbasin, or need to create a new superbasin.

Another difficulty we get when implementing the superbasin method into the OTF-KMC is that, sometimes a transition may result in the number of defect volumes in the system changing. For example, two separated defect volumes merge to be one, or one defect volume splits into two. If such transitions have low barriers, which means a superbasin state may be related to multiple defect volumes, the superbasin will fail to be built. Therefore, in our superbasin method, we also check whether the selected transition changes the total number of defect volumes in the system or not. If the number changes, we need to discard all built superbasins and start over.

The superbasin method is implemented into OTF-KMC in the following way:

**Step 1** Search/Reuse transitions on defect volumes. All transitions found are opted into the available list.

▶**1.1**. If there are any existing superbasins, newly found transitions which are associated with the superbasins are stored in the superbasins and all transitions which are stored in the superbasins are also opted into the available list.

▶**1.2**. Update all the rates of transitions which are associated with the superbasins.

**Step 2** Select an event to execute in the available list.

►**2.1**. If a low-barrier event is selected.

▷**2.1.1**. If the selected low-barrier event doesn't belong to any existing superbasins. A new superbasin is created containing both current state and next state. Transitions associated with the superbasin are also stored into the superbasin.

▷**2.1.2**. If the selected low-barrier event belongs to an existing superbasin. Current states are added into the superbasin, as well as all transitions associated to it.

►**2.2**. If a normal event is selected.

▷**2.2.1**. If this transition is not associated with any existing superbasins, go on normally.

▷**2.2.2**. If this transition is not associated with a superbasin, delete the superbasin.

**Step 3** Advance the clock $\Delta t = -\ln(u)/\sum_i R_i$, where $u \in (0, 1]$ is a random number and $R_i$ is the modified rate for each transition. Go back to Step 1.

A flow chart for the basin method implementation into the OTF-KMC is shown in Figure 6.6.

In the OTF-KMC algorithm, we search for transitions on the fly, therefore we cannot guarantee finding all the transitions. It's possible that we only find the transition $T_{A\to B}$ while doing searches on state $A$, but the reverse transition $T_{B\to A}$ is not found while doing searches on state $B$. (Assume both $A$ & $B$ are transient states in the superbasin.) But the basin method requires both transitions to ensure the equilibrium. To solve this problem, we build the reverse transition $T_{B\to A}$ according the the known transition $T_{A\to B}$, in the case of $T_{B\to A}$ is not found by searches. We build the reverse transition $T_{B\to A}$ when the transition $T_{A\to B}$ is found by simply reorder the final and initial states of $T_{A\to B}$.

The flow chart for building reverse transitions is shown in Figure 6.7. In the OTF-KMC, if there are transitions stored for the defect volumes, we launch refinements (reuse transitions); otherwise we launch searches. We store the built reverse transitions with a flag, identifying that no searches are done on this volume. Therefore we still need to do searches for this volume even though we already have several transitions stored. During the searches, if the transition found is a low-barrier event,

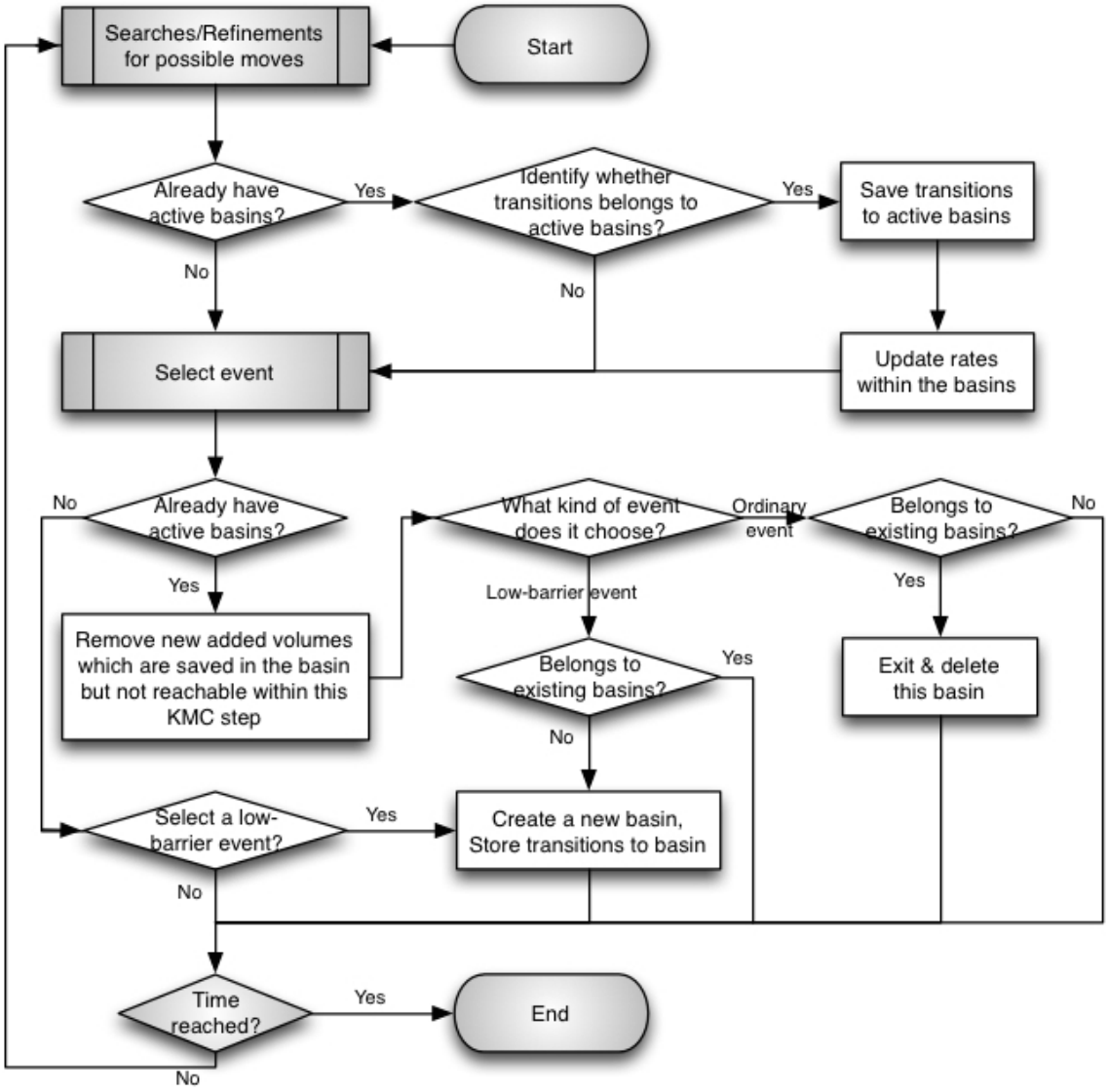


**Figure 6.6:** Flow chart for basin method implemented into the OTF-KMC. Dark procedures indicates standard OTF-KMC procedures without basin method.

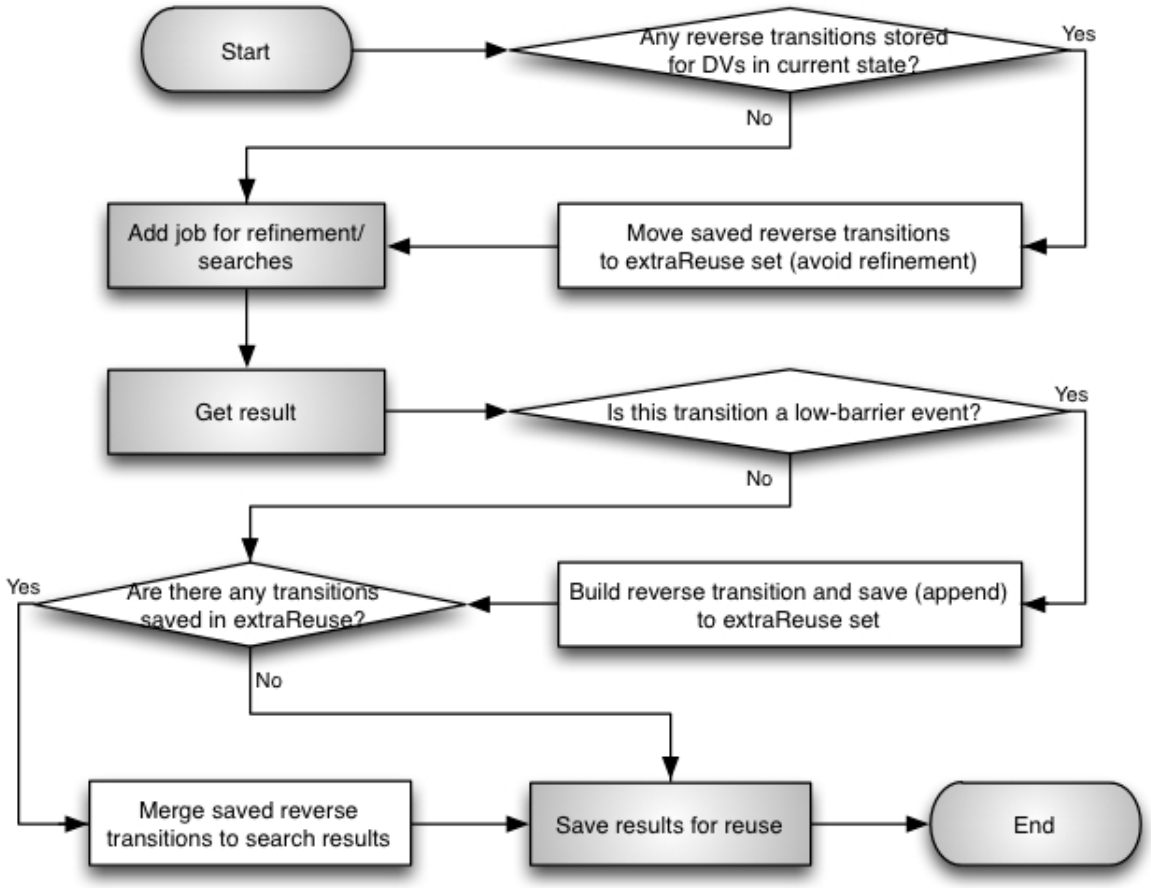


**Figure 6.7:** Flow chart of building reverse transitions during searches.

we build the reverse transition and save it. After we have done all searches for the volume, we need to merge the saved reverse transitions to the current results. Thus we can solve the problem of one way connection between transient states in the superbasin.

Since transitions found in the OTF-KMC are with respect to defect volumes, the built superbasins are with respect to defect volumes as well. We use the hash keys to identify the topologies of defect volumes. The uniqueness of hash key for a defect volume is very important, especially for the superbasin method. However, a very small disturbance could result in building a different defect volume, e.g. atoms at the boundary of defect volumes could be included or excluded due to disturbance, thus have different hash keys. Those defect volumes with different hash keys should represent the same state, and the inconformity of the hash keys for the same state will make the superbasin method fail. On one hand, the superbasin will regard identical states with different hash keys as different states, so the modified rates are not correct any more. On the other hand, if the superbasin method decides to select an escaping transition from a superbasin state, but the hash key associated with it changes, the method would fail because it believes the selected transition is not in the superbasin. We solve the problem by comparing the actual positions of atoms in the defect volumes. For two given defect volumes, first we check the hash keys and the position of the defect volumes (center of mass and moments). If the positions of two defect volumes are close enough, but the hash keys are different, we will check the separations of common atoms in both defect volumes. Once we determine that two defect volumes with different hash keys are actually the same state, we store the hash keys as extra information for future defect volume checks.

## 6.6 Conclusions

We combined the advantages of the bac-MRM and the LS-KMC methods. The superbasin method implemented in the OTF-KMC are able to build multiple superbasins for the system, and build superbasins on the fly without knowing everything in advance.

Without activating superbasin method in the OTF-KMC, the example shown in Figure 6.1 is trapped in these states for hundreds of KMC steps with the simulation time increment at ps time scales. By using the low-barrier threshold $E_{\min}$ =0.1 eV

in the superbasin method, we can build and exit the superbasin in 3 KMC steps with the simulation time increment at 0.1 ns time scales.

Similarly, by setting the low-barrier threshold $E_{\min}$ =0.3 eV, we can speed up the simulations of examples shown in Figure 6.2 & 6.3 by using the superbasin method.

The superbasin method is an efficient way to solve the low-barrier transition problems. By building a superbasin with a reasonable threshold, the simulation can exit the superbasin in a very short time and can be hundreds of times faster or even more than the standard OTF-KMC algorithm.

# Chapter 7

# Cadmium Telluride Thin Film Growth

The CdTe thin film solar cells are the second generation of solar cells. They have great potential and are a cheaper technology than conventional Si based photovoltaic devices[6]. Defects such as grain boundaries and intra-grain dislocations are responsible for lower the efficiency of CdTe thin film solar cells[9]. The main part of the CdTe thin film photovoltaics is the CdTe thin film layer. By modelling the growth of CdTe thin film is helpful to understand the formation of defects and therefore find a way to reduce them.

We deposit $Cd_xTe_y$ $(x, y = 0, 1)$ clusters onto a perfect CdTe surface with various conditions such as substrate, temperature, deposition energy and growth rate. The deposited clusters are allowed to diffuse on the surface. With more and more clusters deposited onto the surface new layers are formed and the CdTe thin film grows.

The growth conditions vary for different experimental techniques. We model the growth of CdTe thin films by magnetron sputtering deposition, which is a widely used technique for CdTe thin film production. In sputtering room temperature deposition is the most common, but elevated temperatures can be used to optimise performance[18]. The temperature we used in the simulations is $T = 350$ K.

Experimental results show that single phase CdTe can only support a maximum excess of 0.004 at % of Cd or 0.013 at % of Te[118]. Experiments undertaken by C. Ferekides et al. also indicate that even if there is an excess of Cd, the produced film will always be stoichiometric. In their experiments, the ratio Cd/Te = $1.0 \sim 1.3$ in vapour, and the ratio Cd/Te = $0.97 \sim 1.03$ in produced film[119]. This means

the ratio of Cd and Te in the vapour has little effect on the stoichiometry of the produced film. For a start, we choose the CdTe molecules as the deposited cluster.

The CdTe impact energy for magnetron sputtering varies. The results of single molecule depositions discussed in Chapter 5 show that the higher the energy is, the more defects are formed. Therefore we use low deposition energies in our simulations. We set up several simulations with various deposition energies of 0.1 eV, 1 eV and 10 eV.

As known the (111) and (100) surfaces are most commonly seen surfaces in the CdTe layers. In this work, we mainly focus on using the OTF-KMC with superbasin method and MD method to simulate the CdTe thin film growth on the (111) surfaces. We also use MD to simulate the CdTe thin film growth on the (100) Te-terminated dimerised surface.

## 7.1 Growth on (111) Surfaces

### 7.1.1 Introduction

In the laboratory, the CdTe layer is usually deposited on the CdS, which has the structure of Wurtzite. The (111) surface of CdS has a hexagonal shape, which is the same as zinc-blende structured (111) surfaces. The main difference between Wurtzite and zinc-blende structures in the [111] direction is the stacking sequences. As discussed in Section 4.4, the stacking sequence of Wurtzite structure is AaBbAaBb, while the stacking sequence of zinc-blende is AaBbCcAaBbCc. In other words, there are "missing" layers in the Wurtzite (111) surfaces compare to the zinc-blende (111) surfaces. Therefore in theory, the CdTe would grow on the (111) plane. However the lattice mismatch is possible and we may have many surfaces. Experimental results show that (100) and (111) surfaces are most common seen in the CdTe layer. A unit cell of zinc-blende CdTe is shown in Figure 7.1. In the [111] direction, the lattice consists of a Cd layer followed a Te layer (we call both layers together a double-layer).

Typical deposition rates for sputtering are between 0.1 nm/sec and 1 nm/sec[18]. In our simulations, the deposition rate is set to be 10 double-layers/sec ($\sim$2 nm/sec). The chosen deposition rate is slightly higher than the experimental results because we want to accelerate the simulations by depositing more frequently, thus get new layers faster, as this represents the slowest deposition rate that allows us to deposit

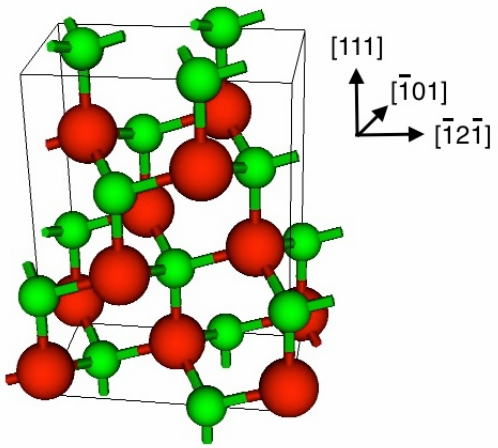


**Figure 7.1:** Unit cell of zinc-blende CdTe in [111] direction. Bigger red spheres represent the Te atoms, and smaller green spheres the Cd atoms.

a reasonable number of layers. In our simulations, there are 160 atoms per double-layer on the (111) surfaces and the deposited clusters are CdTe molecules, thus the rate for deposition is $R_{\text{depo}} = 800\ \text{s}^{-1}$.

As described in Chapter 5, during the simulation, the periodic boundary conditions are applied in all barring the surface directions. We fix the bottom 2 layers of atoms, and thermalise 2 layers above the fixed layers at the chosen temperature $T$. The single CdTe clusters are quite mobile on the surface and they may diffuse hundreds or even thousands of KMC steps before another deposition occurs. We start the simulations with 3 deposited CdTe clusters on the Te-terminated (111) surfaces and 4 CdTe clusters on the Cd-terminated (111) surfaces. The isolated CdTe clusters will diffuse around and join to become bigger clusters which are less mobile and another deposition is more likely to occur. The OTF-KMC method is used to determine whether to perform a diffusion or a deposition in each step. If a deposition event is selected, the algorithm will switch to MD to perform a deposition. In this work, we undertake several individual simulations with different growth conditions.

For a start, we use the standard OTF-KMC without the superbasin method. The results show that, the simulations are always "trapped" in several low-barrier-connected states as described in Chapter 6. We implement the superbasin method to solve the problem. The low-barrier threshold $E_{\text{min}}$ in the superbasin method is chosen to be larger than the low-barrier transitions, which we want to get rid of, but

smaller than most of other escaping transitions. The choice of $E_{\min}$ can be made during the simulations, and $E_{\min}$ may increase to get rid of repeated states observed in the simulations. However the value of $E_{\min}$ cannot be too large, otherwise you may end up with creating a huge superbasin of the whole surface and we cannot get the dynamics of atomic movements. Our choice of $E_{\min}$ is 0.35 eV. This value is large enough to create superbasins for "flicking" (0.1 eV) and "rotating" (0.3 eV) of CdTe adatoms on the surface discribed in Section 6.2, and is smaller than most escaping transitions (0.4 eV).

Due to the complexity of the analytical CdTe BOP potentials, the time taken for saddle searching is much longer than other systems, such as growth of ZnO with the reactive force field potential[120], even for a small system with about 1000 atoms. Another difficulty is that there are many meta-stable states on the CdTe surfaces, and the standard OTF-KMC simulations give results of repeated and meaningless "flickering" without much progress on evolving the system. We implement the superbasin method to get out of these low-barrier-connect states fast without altering the evolution of the system. In this work, all simulations are done on the Loughborough University's High Performance Computing (HPC) services with 48 CPU cores per simulation. It takes about 4 month of calculations for these simulations on HPC.

### 7.1.2 Simulation Results

In this work, we use the OTF-KMC with superbasin method to simulate the growth of CdTe thin films on (111) surfaces. We undertake several individual simulations with different growth conditions. In all simulations, the CdTe molecule is chosen as the deposited cluster. The simulation temperature is $T = 350$ K and the deposition rate is $R_{\text{depo}} = 800\ \text{s}^{-1}$, therefore the corresponding barrier calculated by the Arrhenius Equation for a deposition event is $E_{a,\text{depo}} = 0.701$ eV. Using an effective barrier rather than a rate enables us to compare more easily with the results from the KMC steps. Transitions with barrier lower than $E_{a,\text{depo}}$ will have higher probabilities to be chosen. Since the Arrhenius Equation for rate calculation is an exponential function, small changes to the barriers could result in huge differences in rates.

The growth simulations are undertaken on Cd-terminated (111) surfaces and Te-terminated (111) surfaces. On each surface, we set up several simulations with

deposition energies at 0.1 eV, 1 eV and 10 eV. Starting with several ad-atoms deposited on the surface, the OTF-KMC algorithm is used to determine whether to perform a step of diffusion or deposition.

Despite different deposition energies, all simulations show similar film growth mechanisms for each kind of surfaces. The results show that single atoms and small ad-atom clusters are highly mobile on the surface. Single Cd/Te atoms or small CdTe clusters diffuse rapidly on the surface until they meet other clusters and form a bigger cluster, which is less mobile. The diffusivity is significantly reduced when the clusters contain at least 4 atoms, as we do not observe any movements involving more than four atoms.

The Cd- and Te-terminated (111) surfaces have different ways of growth, and will now be discussed separately.

### 7.1.3 Te-terminated (111) Surfaces

#### 7.1.3.1 Growth Mechanisms

On the Te-terminated (111) surfaces, the deposited CdTe clusters usually stick on the surface without dissociation, thus clusters of ad-atoms on the surface are stoichiometric. When the CdTe clusters are deposited onto the surface, they usually "lie down" on the Te-terminated (111) surfaces, where both the Cd and Te atoms are at the same height. The top view and front view of a deposited cluster deposited on the Te-terminated (111) surface are shown in Figure 7.2. The diffusions of small clusters will be discussed in Section 7.1.3.2.

Bigger clusters are less mobile, and they usually form a zig-zag chain like shape on the surface. These zig-zag clusters are, again, "lying down" on the surface. A top view and front view of zig-zag chains observed in the simulations are shown in Figure 7.3.

Due to the structure of CdTe lattice, the new CdTe surface layers should grow in pairs in [111] direction, i.e. a new layer of Cd and a new layer of Te should be formed together (we call both layers together a double-layer). However, on the Te-terminated (111) surfaces, initially when there are not enough ad-atoms on the surface, all deposited ad-atoms are "lying down" on the surfaces, i.e. we have a mixed layer containing both Cd and Te atoms. We observe zig-zag chains of bigger size on the surface, e.g. the highlighted cluster in Figure 7.4a. Later when the deposited clusters become bigger, a novel mechanism of second layer formation has

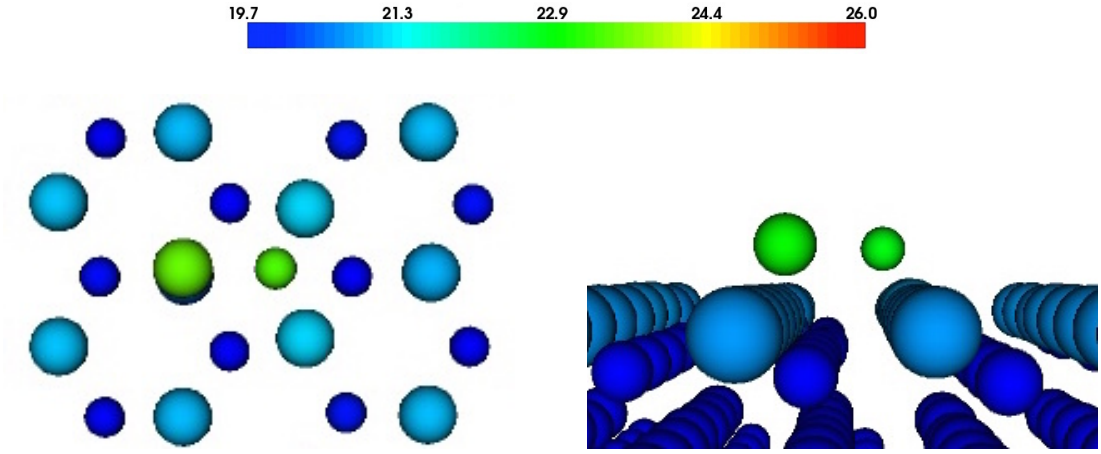


**Figure 7.2:** Top view (left) and front view (right) of a CdTe cluster deposited on the Te-terminated (111) surface. The deposited cluster "lies down" on the surface, i.e. both atoms are at the same height. The Te atom sit directly on the surface Te atom, and the Cd atom sits in the hollow site. Graphs are coloured by height. Bigger spheres represent the Te atoms, and smaller spheres the Cd atoms.

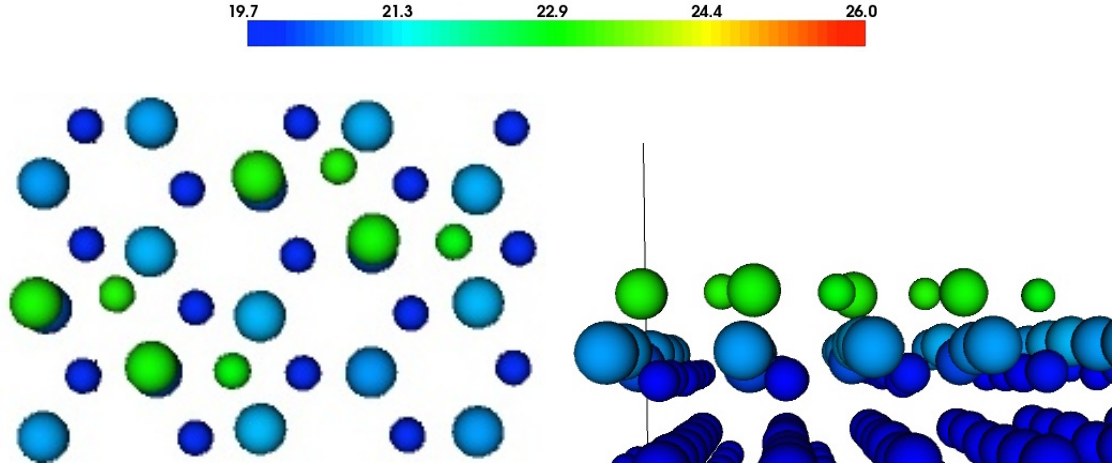


**Figure 7.3:** Top view (left) and front view (right) of zig-zag chain shape clusters on the Te-terminated (111) surface. All ad-atoms in the cluster "lie down" on the surface, i.e. they are at the same height. Graphs are coloured by height. Bigger spheres represent the Te atoms, and smaller spheres the Cd atoms.

been observed where the Te atoms move out of the first new layer to form another new layer. These atoms are highly mobile when they move to this new layer and they dominate the dynamics of the system. Figure 7.4 shows a front and top views of systems without and with the second layer formed. Later in Section 7.1.3.3, The mechanism of second layer formation will be discussed.

Since all simulations are undertaken at the same temperature, and the deposition energy is not high enough to damage the original surface, the diffusions of ad-atoms on the surface are quite similar. The main differences among simulations with different deposition energies are observed during the deposition process. Low deposition energies (0.1 eV and 1 eV) give no significant differences on the depositions. The deposited clusters perform soft landing on the surfaces, thus no significant differences during the growth process. However with high deposition energy (10 eV), we observe that the deposited cluster may penetrate the surface, and create interstitials below the surface layers. Figure 7.5 highlights the interstitials created due to the high deposition energy.

Figure 7.6 shows the CdTe thin film growth on Te-terminated (111) surface after 83 ms of real time. The temperature is 350 K and the deposition energy is 1 eV. There are point defects created on the original surface due to the energetic impacts. Two incomplete new double-layers are formed. In the first new double-layer, most Te atoms still at the same height as Cd atoms. However in the regions where the second new double-layer is formed, Te atoms in the first new double-layer are generally higher than Cd atoms. This indicates that the Te atoms in the first new double-layer will move to their correct heights when the second new double-layer starts to form above them.

#### 7.1.3.2 Small Cluster Diffusions

During the simulations, the deposited clusters diffuse around the surface. When they meet others, they join to be a bigger cluster, and become less mobile. At the early stage of the OTF-KMC simulations, we observe repeatable diffusions of small clusters or single atoms on the surface. These transitions are very important to understand the mechanisms of small cluster diffusions on the surface.

The simulation results show that on the Te-terminated (111) surfaces, the deposited CdTe clusters always stick onto the surface in pairs. And generally, the barriers of diffusive transitions for a single CdTe cluster are much lower than $E_{a,\mathrm{depo}}$,

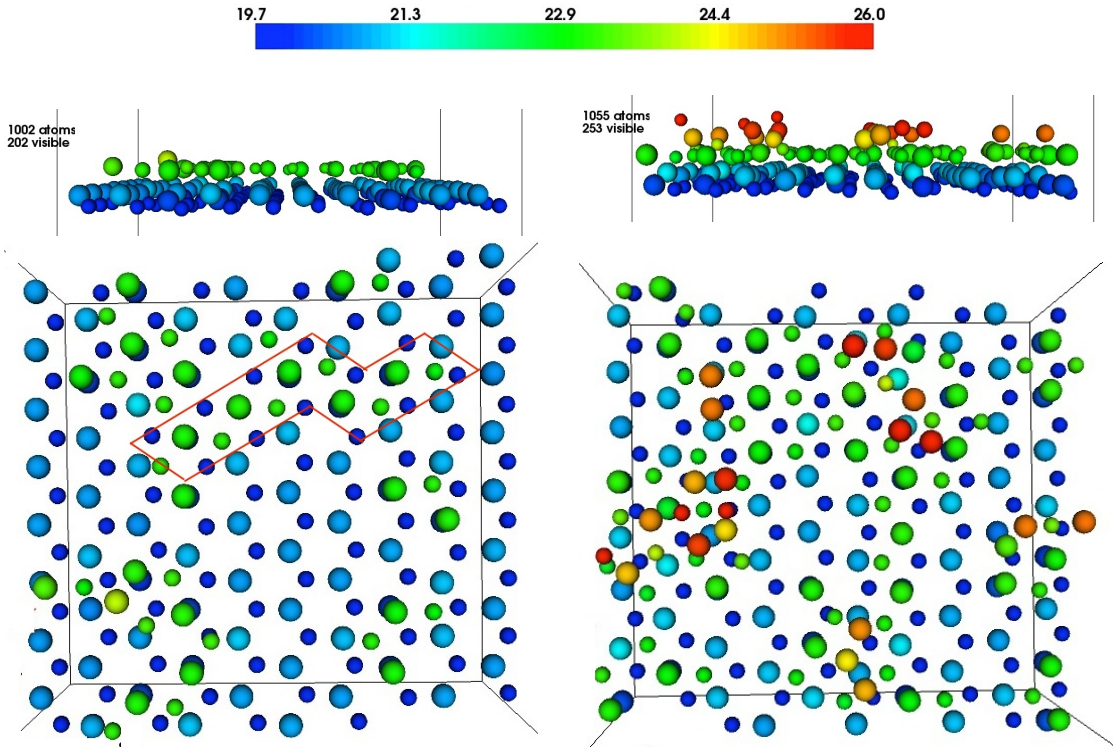


**(a)** A system with 42 ad-atoms on the Te-terminated (111) surface. All ad-atoms stay in the same layer. A cluster of zig-zag shape is highlighted.

**(b)** A system with 95 ad-atoms on the Te-terminated (111) surface. The second new layer starts to be formed.

**Figure 7.4:** Front (upper) and top (lower) views of systems without (left) and with (right) the second layer formed on the Te-terminated (111) surface. The deposited ad-atoms initially "lying down" on the surface. Later with more ad-atoms are deposited on the surface, bigger clusters would push Te/Cd atoms out of the initial layer to form a new layer. Graphs are coloured by height. Bigger spheres represent the Te atoms, and smaller spheres the Cd atoms.

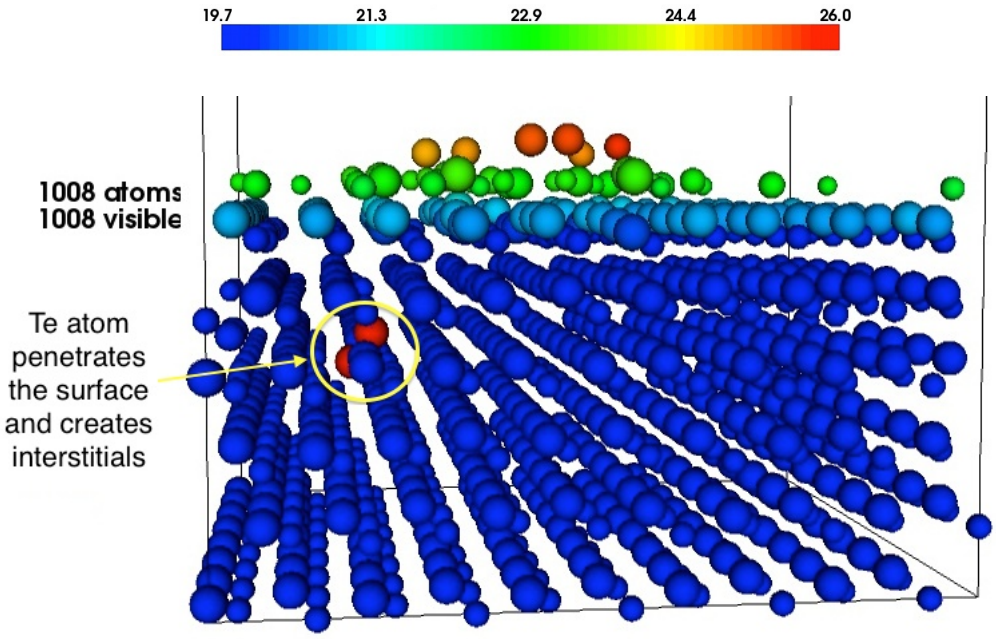


**Figure 7.5:** Deposited cluster with high energy penetrates the surface and create interstitials below the surface layers. Graph is coloured by height with highlighting the interstitials below the surface. The Te atom penetrates the Te-terminated surface with deposition energy of 10 eV, and creates interstitials ∼8 Å below the original surface layer. Bigger spheres represent the Te atoms, and smaller spheres the Cd atoms.

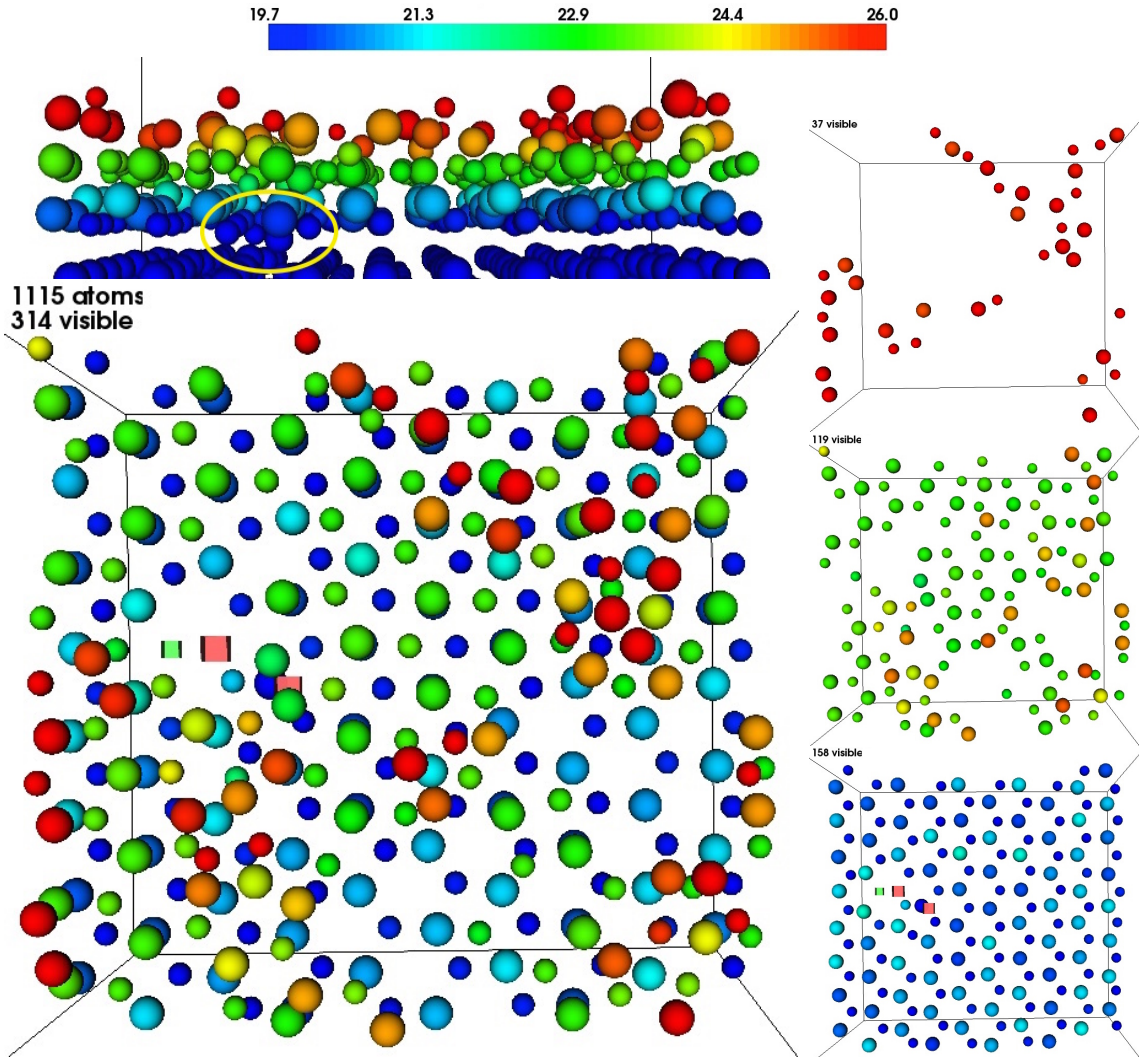


**Figure 7.6:** CdTe thin film growth on Te-terminated (111) surface after 83 ms of real time. The deposition energy is 1 eV. A front view (upper left) and a top view (lower left) of the surface and new double-layers are presented on the left. Three graphs on the right shows the second new double-layer, first new double-layer and the original surface double-layer, respectively. There are 155 ad-atoms on the surface. The circled region in the front view (upper left) of the lattice indicates point defects created due to the energetic impacts. The first new double-layer is incomplete while the second new double-layer starts to form. Most Te atoms in the first new double-layer have the same height as Cd atoms. Graphs are coloured by height. Green and red cubes represent Cd and Te vacancies, respectively. Bigger spheres represent the Te atoms, and smaller spheres the Cd atoms.

which indicate that the diffusions of small clusters occur more rapidly than deposition.

The diffusions of a single CdTe cluster on the Te-terminated (111) surfaces are quite complicated. There are two most common seen sites for the single CdTe cluster to sit. Typical transitions between these sites are shown in Figure 7.7. We notice that in the first transition between Site A and Site B, only the Cd atom is moved, and the barrier is smaller than other transitions involving movement of both the Cd and the Te atoms. Moreover we do not observe transitions where only Te atoms is moved. We deduce that on the Te-terminated (111) surfaces, Cd atoms are less stable than Te atoms.

Small ad-atom clusters will eventually meet other clusters and join together. Once a cluster of 4 or more atoms forms, the cluster would usually stick there with no diffusions, except the possible second layer formations.

#### 7.1.3.3 Second layer Formation

The deposited small CdTe clusters initially "lie down" on the Te-terminated (111) surfaces. When a larger cluster with 4 or more atoms formed, we observe a mechanism of second new layer formation.

The new deposited double-layers should consist of a layer of Cd and a layer of Te above it. Initially, both deposited Cd and Te atoms in the cluster are at the same height, sitting on the original surface. Figure 7.4a shows all deposited clusters stay in the same layer. When a cluster of size 4 or more atoms formed, there might be a novel mechanism where the Te atoms move out of the first layer and form a new layer above it. Figure 7.8 shows an example of second layer formation.

The Te atoms be "pushed" onto the second new layer are very mobile as shown in Figure 7.9. The barrier is lower than most of other transitions, and the corresponding time is much shorter than most of second layer formation transitions and cluster diffusions. These transitions will dominate the simulations.

Even the second layer is formed, if there are not enough Cd atoms in the first layer to "support" them, Te atoms in the second layer can also "drop back" to the first layer. And of course the back-to-first-layer Te atoms can be "pushed" again to the second layer. Figure 7.10 shows an example of these mechanisms.

We noticed that, by combining transitions shown in Figure 7.8 and Figure 7.10a, the shape of deposited cluster can be changed from zig-zag chain to square shape.

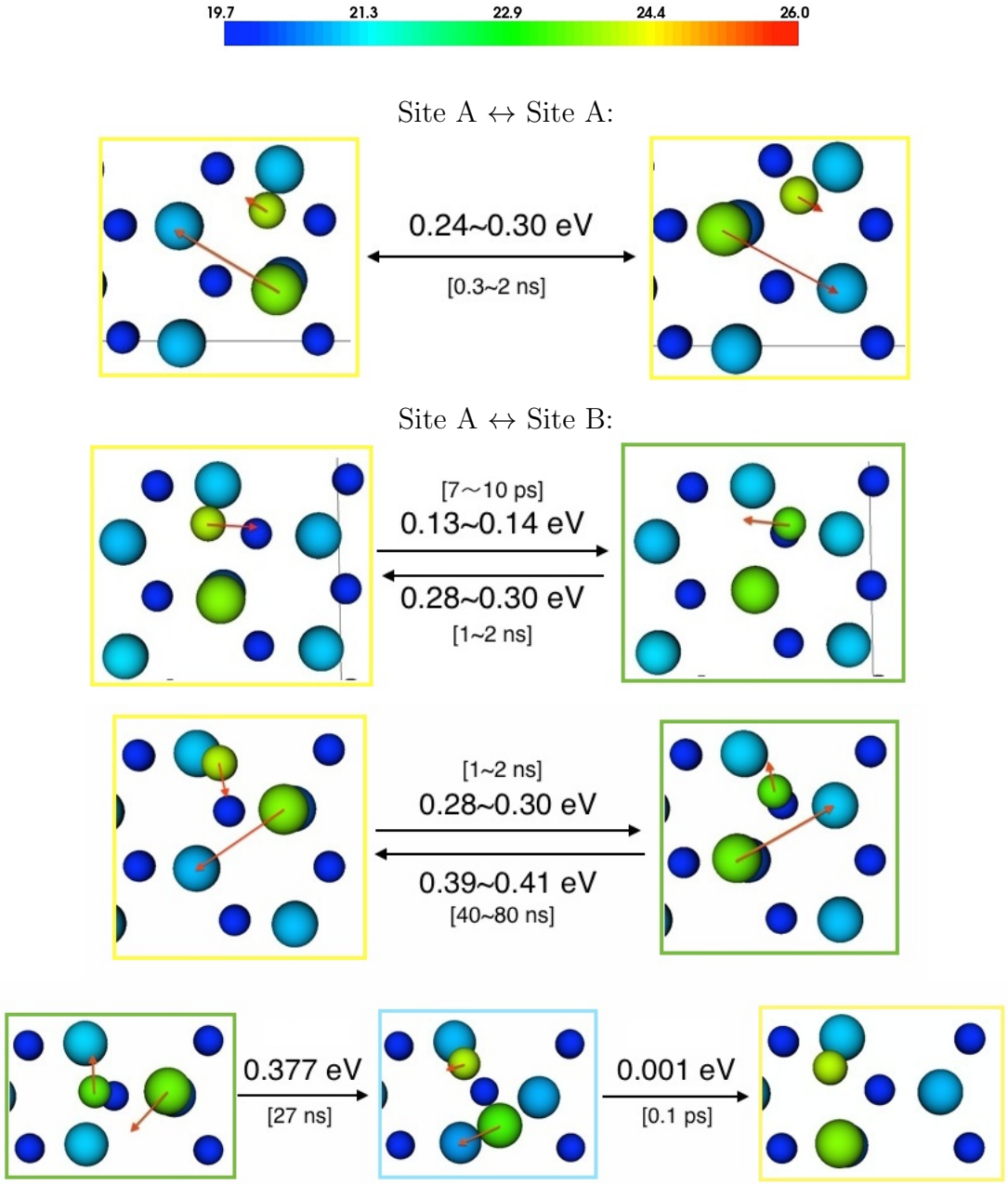


**Figure 7.7:** Transitions of a CdTe cluster on Te-terminated (111) surface. Graphs bounded with the same colour represent symmetrical equivalent sites. Graphs are coloured by height. Bigger spheres represent the Te atoms and smaller spheres the Cd atoms. Red arrows indicate the movements of atoms. Square brackets give the corresponding event time of the transition.

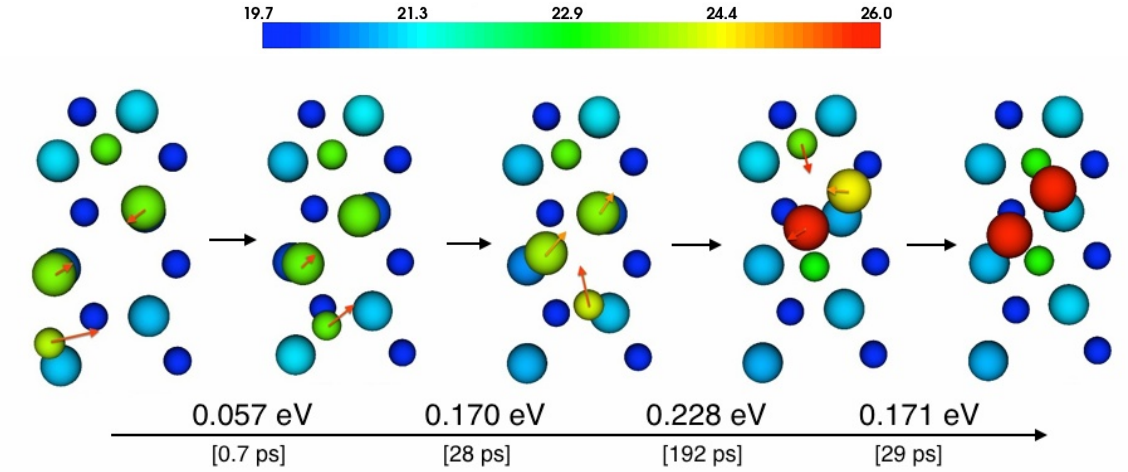


**Figure 7.8:** Mechanism of second layer formation in a cluster of 4 atoms. When two CdTe clusters meet each other, the Te atoms in the middle could be "pushed" out of the first layer to form a new layer. Graphs are coloured by height. Bigger spheres represent the Te atoms, and smaller spheres the Cd atoms. Arrows in the graphs indicate the movement of atoms. The corresponding barriers and event time are given below the graphs.

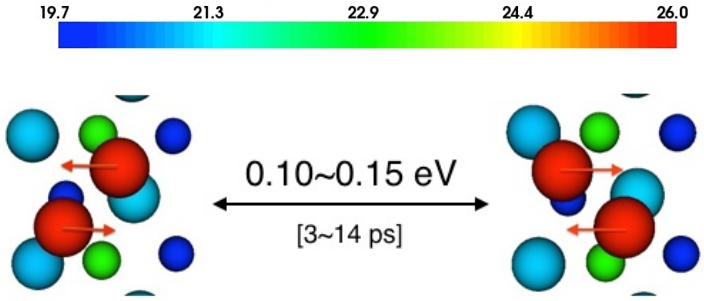


**Figure 7.9:** Te atoms in the second new layer are very mobile. Graphs are coloured by height. Bigger spheres represent the Te atoms, and smaller spheres the Cd atoms. Arrows in the graphs indicate the movement of atoms.

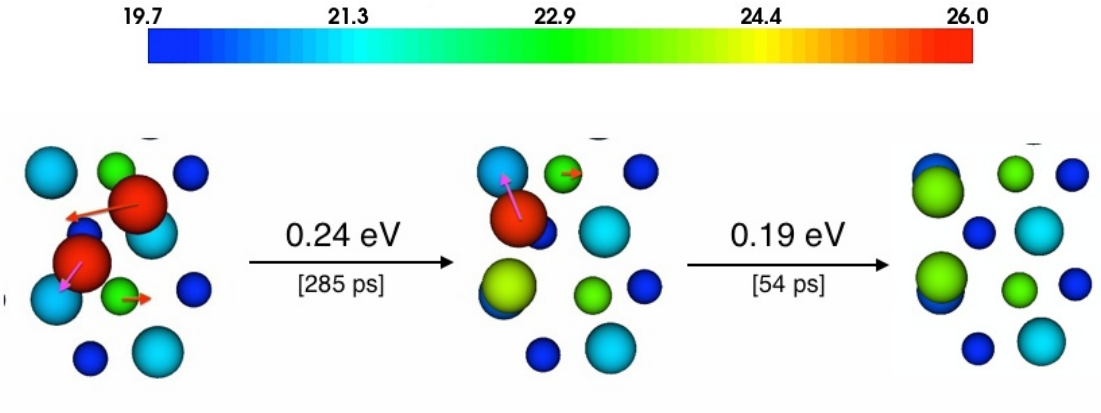


**(a)** Two Te atoms in the second layer are "pulled" back to the first layer.

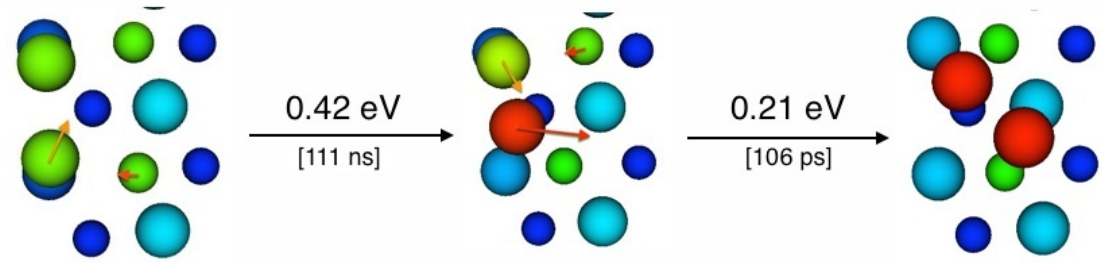


**(b)** Two Te atoms in the first layer are "pushed" onto the second layer.

**Figure 7.10:** An example of Te atoms diffusing between first and second new layers. Graphs are coloured by height. Bigger spheres represent the Te atoms, and smaller spheres the Cd atoms. Arrows in the graphs indicate the movement of atoms.

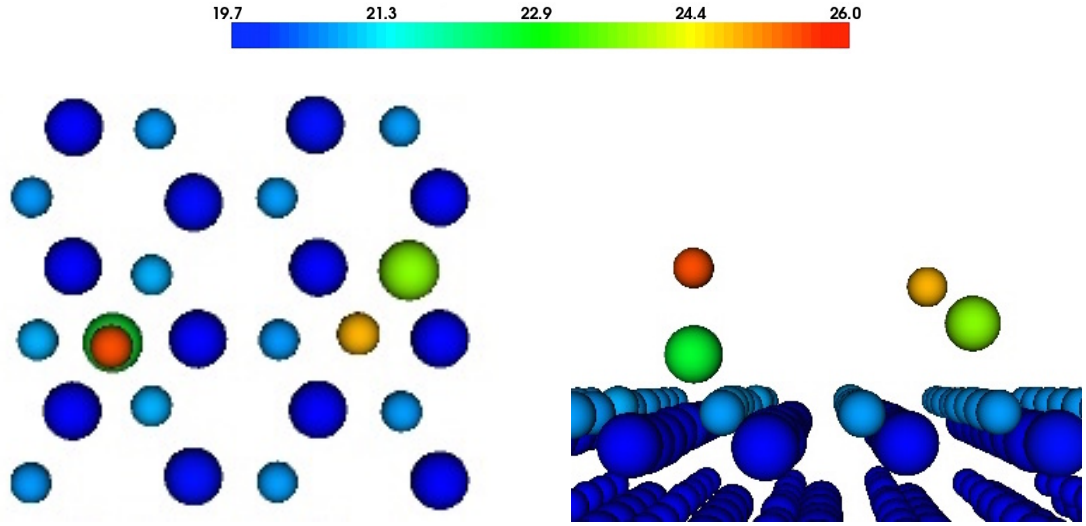


**Figure 7.11:** Top view (left) and front view (right) of a small CdTe cluster deposited on the Cd-terminated (111) surface. The deposited clusters "stand up" on the surface, i.e. Cd and Te atoms are at different heights. There are two positions for a single CdTe cluster sits on the surface: (cluster on the left) the CdTe cluster sits vertically in the hollow site; (cluster on the right) Te atom sits directly above the surface Cd atoms, and Cd atom in the cluster sits in the hollow site with a higher position. Graphs are coloured by height. Bigger spheres represent the Te atoms, and smaller spheres the Cd atoms.

We also observe other more complex mechanisms which transform the deposited clusters to other shapes, such as zig-zag chains and hexagons. These indicate that the shape of deposited clusters could be changed.

### 7.1.4 Cd-terminated (111) Surfaces

#### 7.1.4.1 Growth Mechanisms

The growth mechanism on the Cd-terminated (111) surfaces is different from the Te-terminated ones. One main difference is that the deposited CdTe clusters can dissociate on impacts, thus there are isolated single Cd/Te atoms on the surface and the clusters of ad-atoms can be non-stoichiometric. Another main difference is that the CdTe clusters deposited on the Cd-terminated (111) surfaces "stand up", i.e. the Cd and Te atoms are at different heights as shown in Figure 7.11.

Similarly, once a big cluster with more than 4 atoms formed, there is usually no movements for the cluster. However, unlike zig-zag shape clusters on the Te-

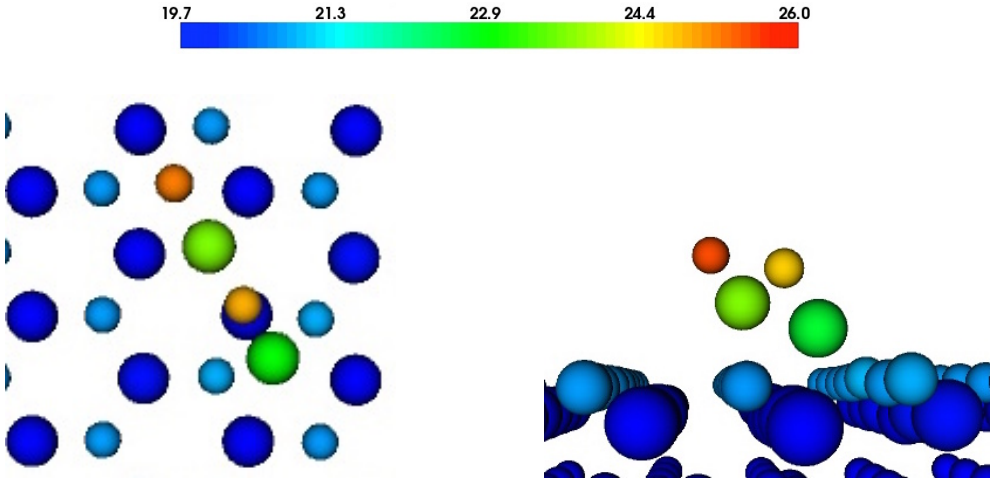


**Figure 7.12:** Top view (left) and front view (right) of straight line shape clusters on the Cd-terminated (111) surface. Cd and Te atoms in the cluster are at different heights. Graphs are coloured by height. Bigger spheres represent the Te atoms, and smaller spheres the Cd atoms.

terminated (111) surfaces, the ad-atom clusters on the Cd-terminated (111) surfaces are usually in straight line shape in the top view as shown in Figure 7.12, where Cd and Te atoms are at different heights.

The growth mechanism on the Cd-terminated (111) surface is simpler than on the Te-terminated ones. Since Cd and Te atoms in the deposited clusters are naturedly at different height, the new double-layer is formed immediately, no second layer formation is needed.

During the simulation, small clusters diffuse around the surface and join other clusters to form a bigger one. The ad-atom-clusters usually form (curved) line shape chains, bigger clusters could form either long line shape chains or double line chains as Figure 7.13 shows. In the simulations, double line chains are observed more often than long single line chains.

Figure 7.14 shows the CdTe thin film growth on Cd-terminated (111) surface after 53 ms of real time. The temperature is 350 K and the deposition energy is 10 eV. We get two incomplete double-layers. There are no defects on the original surface double-layer. The possible defects created during the impacts are recovered due to rapidly diffusions of deposited clusters.

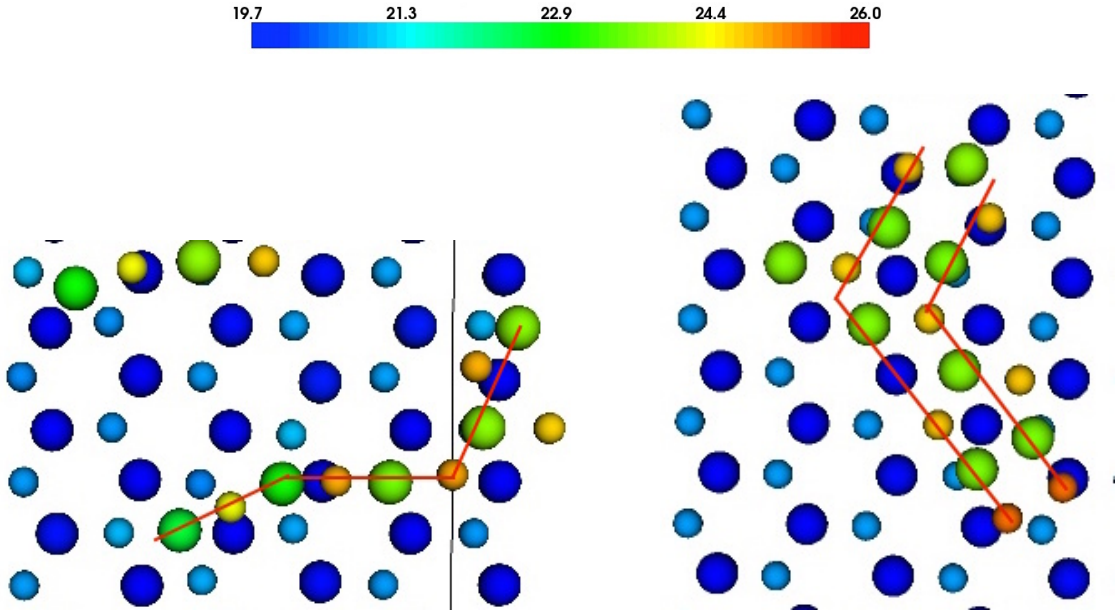


**Figure 7.13:** Clusters on the Cd-terminated (111) surfaces form line shape chains. Left: single line chain. Right: double line chain. Graphs are coloured by height. Bigger spheres represent the Te atoms, and smaller spheres the Cd atoms.

#### 7.1.4.2 Small Cluster Diffusions

On the Cd-terminated (111) surfaces, we observed the dissociation of deposited CdTe clusters, which is not seen on the Te-terminated ones. Thus it worth to investigate the diffusions of single Cd/Te atoms on the surfaces.

On the Cd-terminated surfaces, there are two stable sites for the single Cd atom to stay, and the transitions are shown in Figure 7.15. There are 3 stable sites for the single Te atom to stay on the Cd-terminated surfaces, and the transitions are shown in Figure 7.16. We notice that on the (111) Cd-terminated surfaces, single Cd atom diffuses much more rapidly than single Te atom. The single Te atom prefers to sit in the hollow sites as lower left graph in Figure 7.16 shows. These barriers of transitions explain why we observe the rapidly diffusions of single Cd atom on the surface while the single Te atom barely moves after the dissociation in the simulations.

Figure 7.17 shows the dissociation of a deposited CdTe cluster on the (111) Cd-terminated surfaces. The Cd atom in the vertical CdTe cluster could leave the substrate Te atom. We only observe the dissociation for vertical CdTe clusters, probably because in this case, the force acting on the top Cd atom from the surface is too weak due to the large distance, and the bond between Cd and Te atom is the

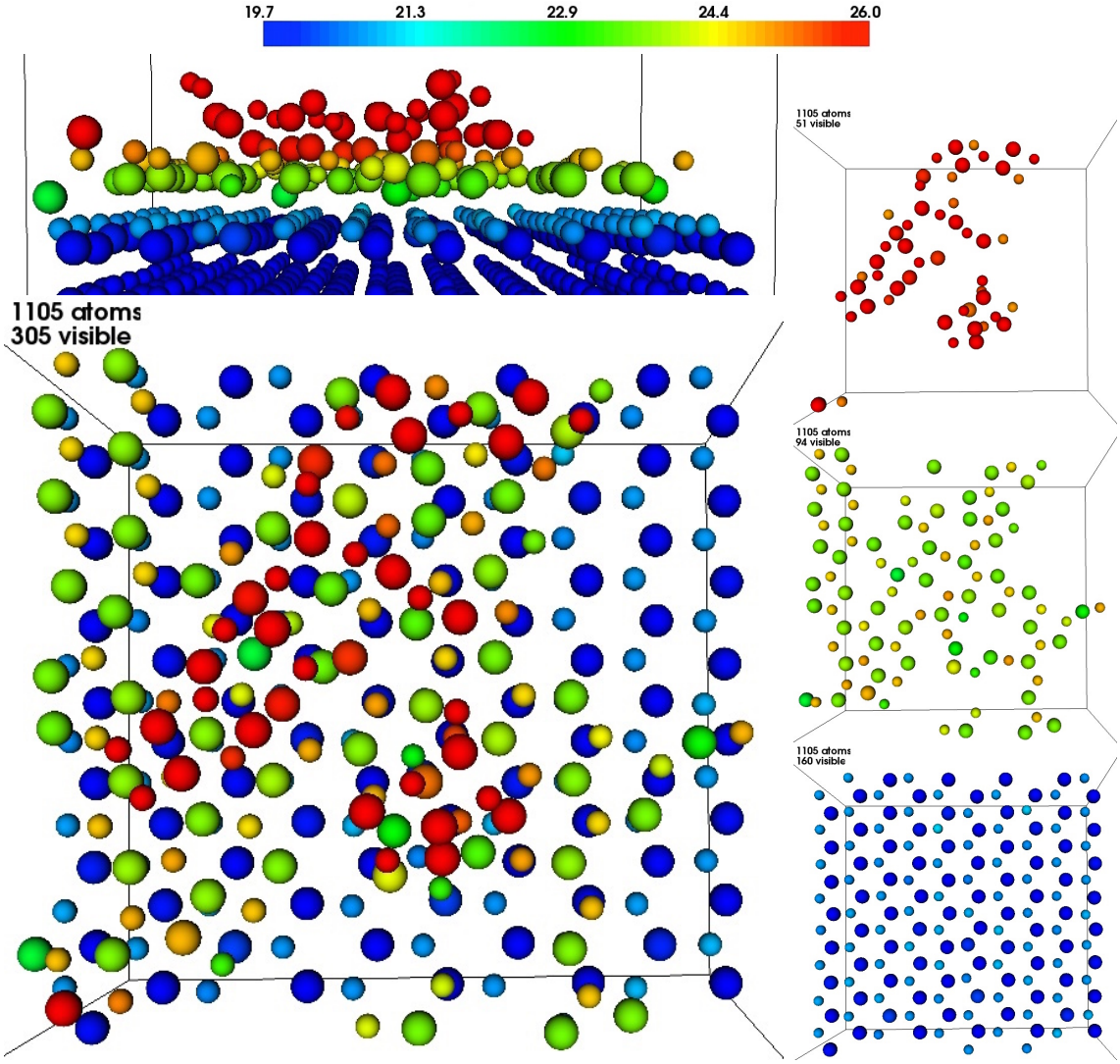


**Figure 7.14:** CdTe thin film growth on Te-terminated (111) surface after 83 ms of real time. The deposition energy is 10 eV. A front view (upper left) and a top view (lower left) of the surface and new double-layers are presented on the left. Three graphs on the right shows the second new double-layer, first new double-layer and the original surface double-layer, respectively. There are 145 ad-atoms on the surface. The first new double-layer is incomplete while the second new double-layer starts to form. Graphs are coloured by height. Green and red cubes represent Cd and Te vacancies, respectively. Bigger spheres represent the Te atoms, and smaller spheres the Cd atoms.

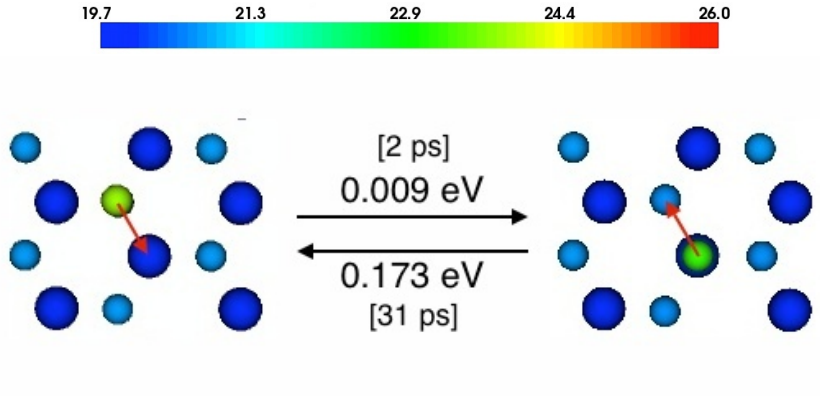


**Figure 7.15:** Transitions of single Cd atom on Cd-terminated (111) surface. Graphs are coloured by height. Bigger spheres represent the Te atoms and smaller spheres the Cd atoms. Red arrows indicate the movements of atoms. Square brackets give the corresponding event time of the transition.

only difficulty to overcome.

The vertical CdTe cluster deposited on the surface could also become "flat" as shown in the upper graph of Figure 7.18. And the "flat" CdTe clusters are able to diffuse around the surface by hopping between three sites as shown in the lower graph of Figure 7.18.

We notice that the transitions of small CdTe clusters on the (111) Cd-terminated surfaces generally have lower barriers than the ones on the (111) Te-terminated surfaces. This means that the diffusions of small CdTe clusters occur more rapidly on the (111) Cd-terminated surfaces than Te-terminated ones. We even observe the diffusions of a 4-atom-cluster on the (111) Cd-terminated surfaces as shown in Figure 7.19. The barriers of these transitions are even lower than ones for a single CdTe cluster. This probably because of the structure of 4-atom-cluster where two Cd atoms sit directly above the Te atoms, far away from the surface, therefore the diffusions of this 4-atom-cluster would be similar to the diffusions of a 2-Te-cluster.

The formation of line chains on the CdTe (111) Cd-terminated surface is similar to the growth of ZnO[120]. As Figure 7.20 shows that, when a single CdTe cluster diffuse near to other cluster, a longer line shape cluster is formed by attaching the single CdTe cluster to the end of other cluster. Alternately, a "Y" shape cluster is formed by attaching the single CdTe cluster to the middle of other cluster. In most cases, a double line shape cluster is formed by attaching both Cd and Te atoms in the CdTe cluster to the other cluster as the last graph in Figure 7.20 shows.

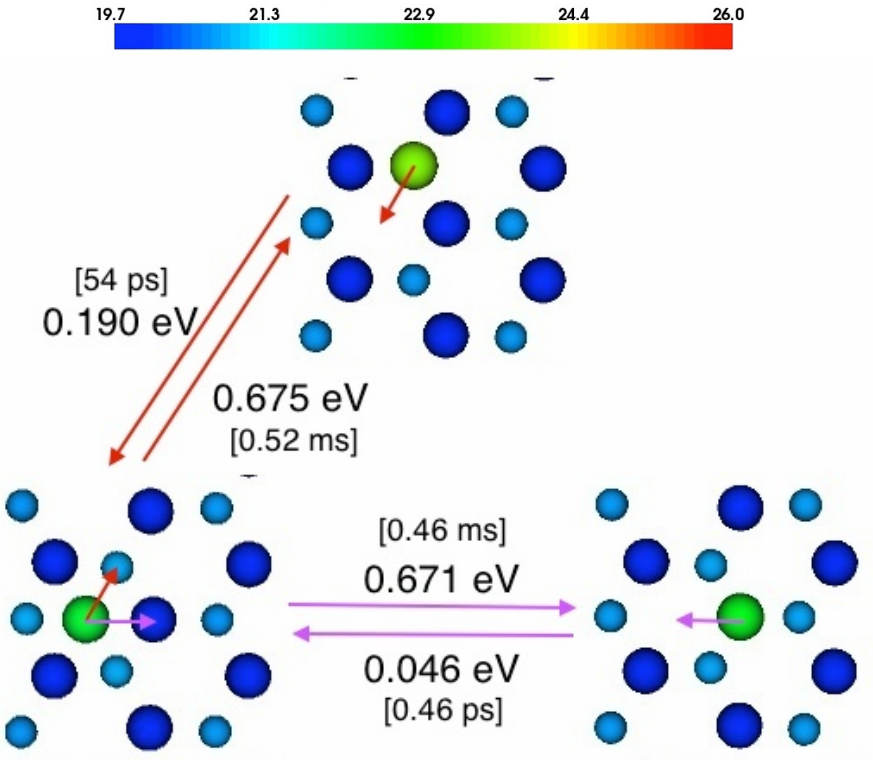


**Figure 7.16:** Transitions of single Te atom on Cd-terminated (111) surface. Graphs are coloured by height. Bigger spheres represent the Te atoms and smaller spheres the Cd atoms. Arrows in the graphs indicate the movements of atoms. Square brackets give the corresponding event time of the transition.

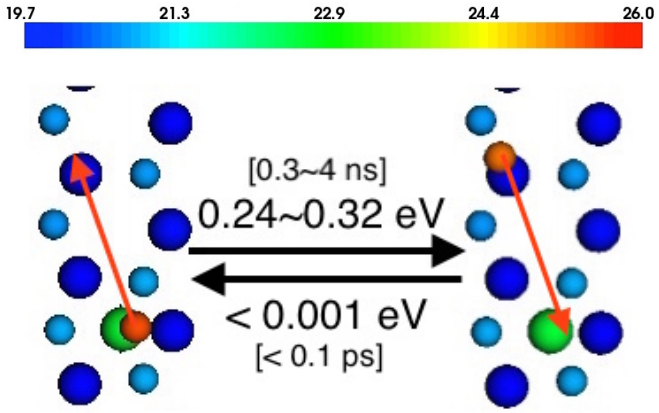


**Figure 7.17:** A single CdTe cluster dissociates on the Cd-terminated (111) surface. Graphs are coloured by height. Bigger spheres represent the Te atoms and smaller spheres the Cd atoms. Arrows in the graphs indicate the movements of atoms. Square brackets give the corresponding event time of the transition.

## 7.2 Growth on (100) Surfaces

### 7.2.1 Introduction

(100) surfaces are another common seen surfaces during the growth of CdTe thin films. We are specially interested in the Te-terminated dimerised (100) surface. As discussed in Section 4.1 on the Te-terminated (100) surfaces, Te atoms in the surface layer are dimerised[102], and the (2×1) dimerisation has a lower energy than c(2×2). Barbara has investigated the dimer opening on a diamond (100) (2×1) surface by using MD in 1992[121]. Since the Te-terminated (100) surface has a similar structure, we are interested in the growth mechanism on the Te-terminated (100) surface, especially how the Te dimers opening during the growth. In this work, we use MD to simulate the thin film growth on the (100) Te-terminated dimerised surface.

The unit cell of zinc-blende CdTe in [100] direction is shown in Figure 7.21. The system is constructed by a layer of Te followed by a layer of Cd, respectively. We refer a double-layer to a pair of Cd and Te layers. The surface Te atoms in the Te-terminated (100) surface will reconstruct as dimers. Figure 7.22 shows a top view of Te-terminated dimerised (100) (2×1) CdTe surface. The surface Te atoms (coloured red) are dimerised, away from their correct sites (coloured dark blue). We are expecting the Te dimers on the surface split and move back to their correct sites

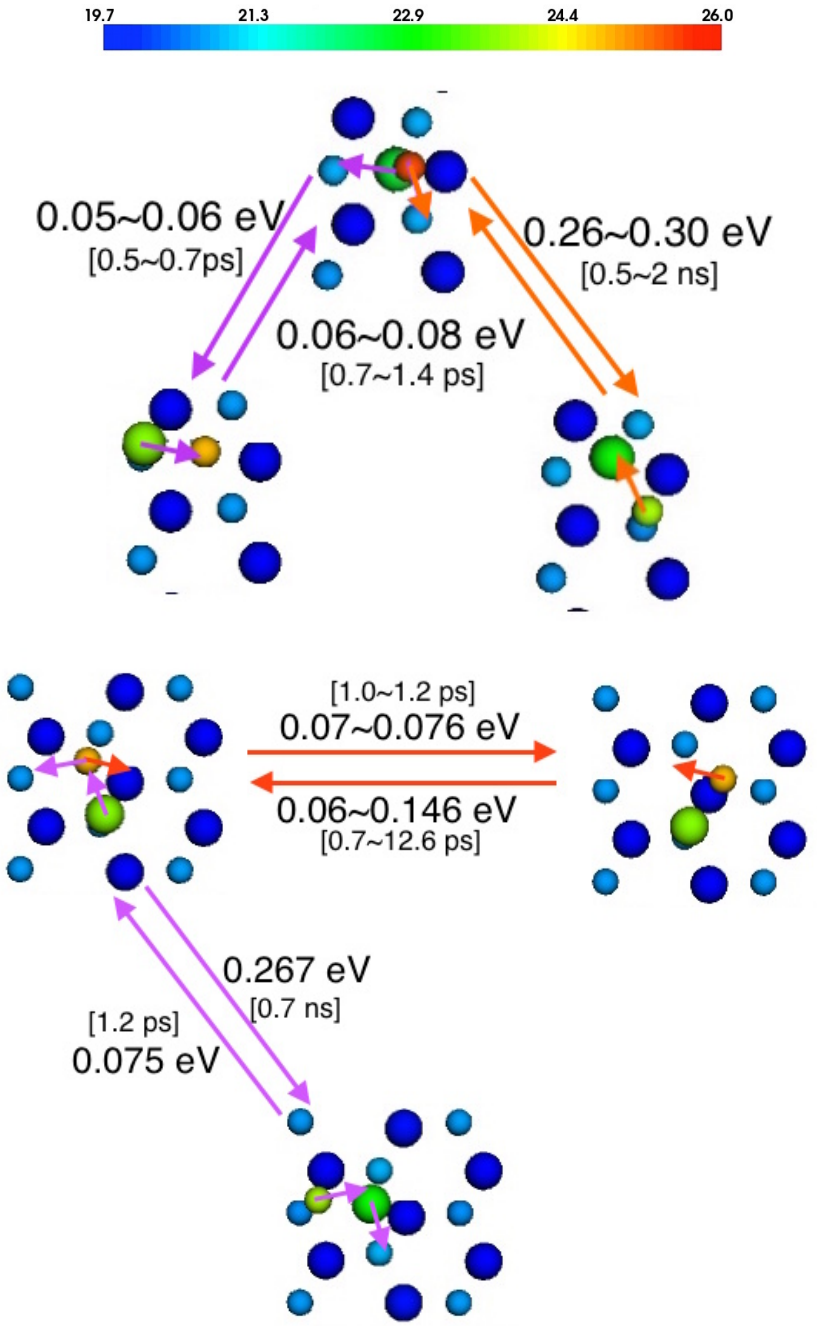


**Figure 7.18:** A single CdTe cluster diffuses on the Cd-terminated (111) surface. Graphs are coloured by height. Bigger spheres represent the Te atoms and smaller spheres the Cd atoms. Arrows in the graphs indicate the movements of atoms. Square brackets give the corresponding event time of the transition.

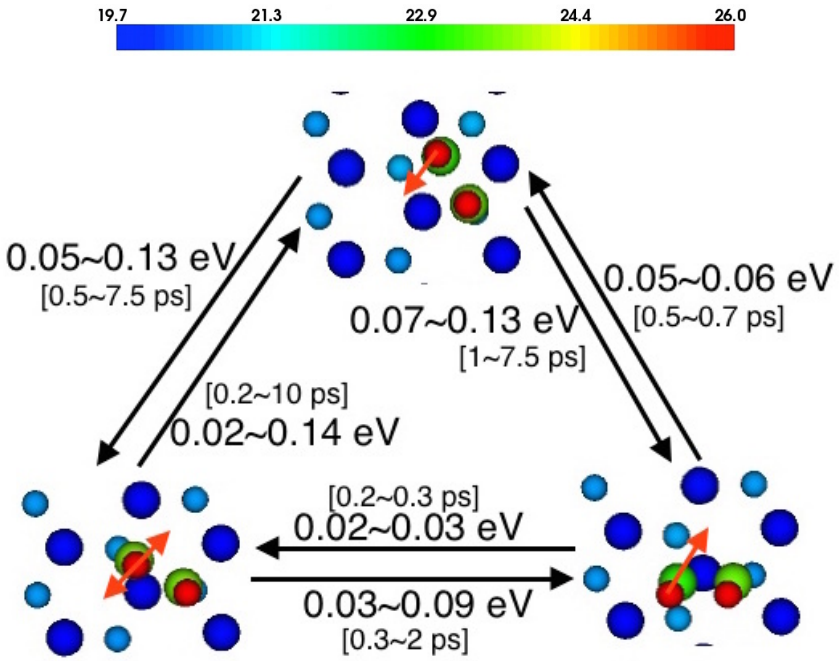


**Figure 7.19:** A 4-atom-CdTe cluster diffuses on the Cd-terminated (111) surface. Graphs are coloured by height. Bigger spheres represent the Te atoms and smaller spheres the Cd atoms. Arrows in the graphs indicate the movements of atoms. Square brackets give the corresponding event time of the transition.

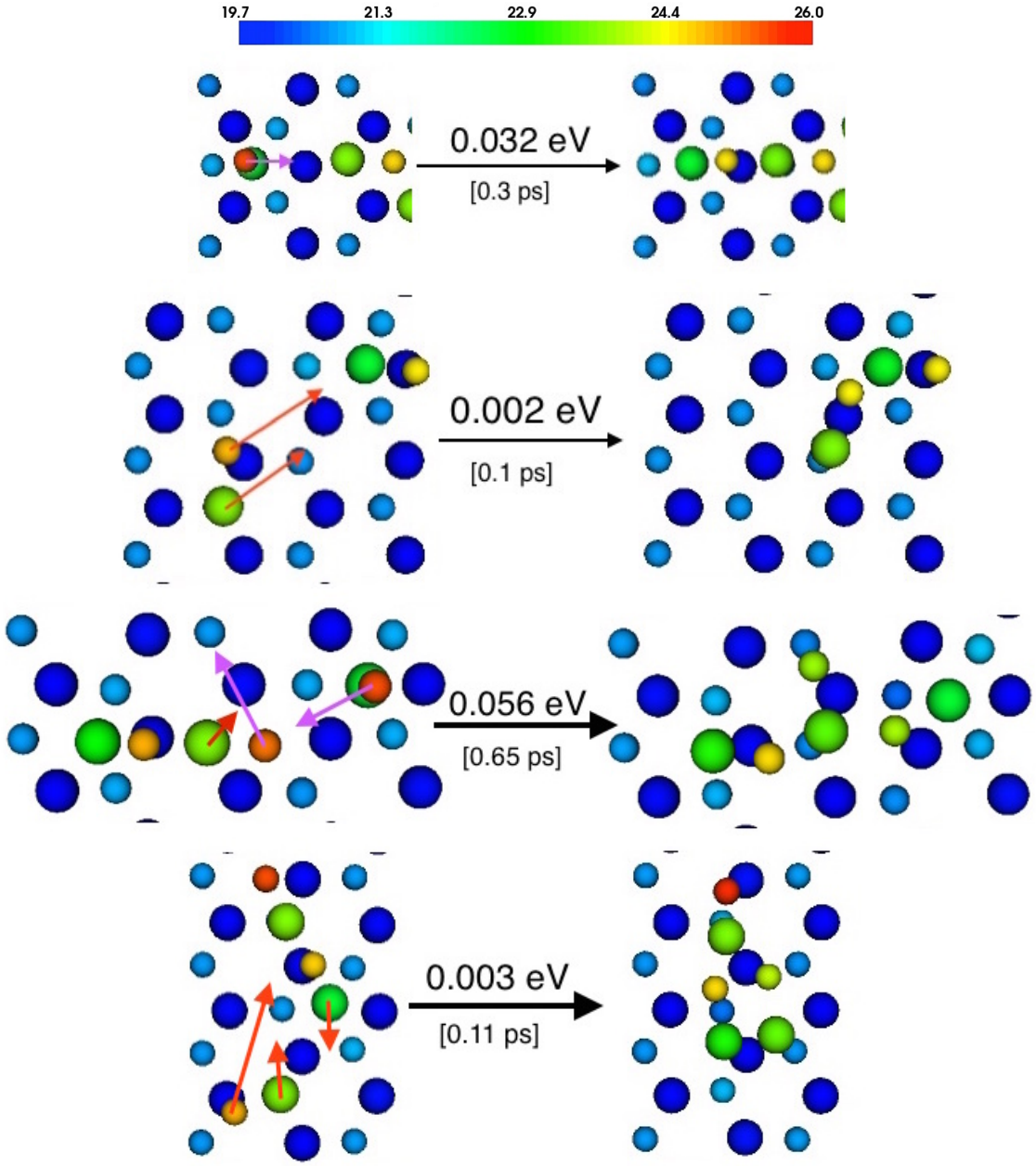


**Figure 7.20:** Formation of chains on the Cd-terminated (111) surfaces. U: A single CdTe cluster diffuses to join the end of a chain, and a longer chain is formed. Lower: A single CdTe cluster diffuses near to an end of a chain, and a "Y" shape cluster is formed by attaching the single CdTe cluster to the middle of line chain. Graphs are coloured by height. Bigger spheres represent the Te atoms, and smaller spheres the Cd atoms. Arrows in the graphs indicate the movements of atoms. Square brackets give the corresponding event time of the transition.

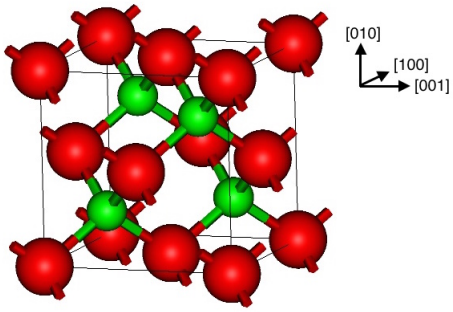


**Figure 7.21:** Unit cell of zinc-blende CdTe in [100] direction. Bigger red spheres represent the Te atoms, and smaller green spheres the Cd atoms.

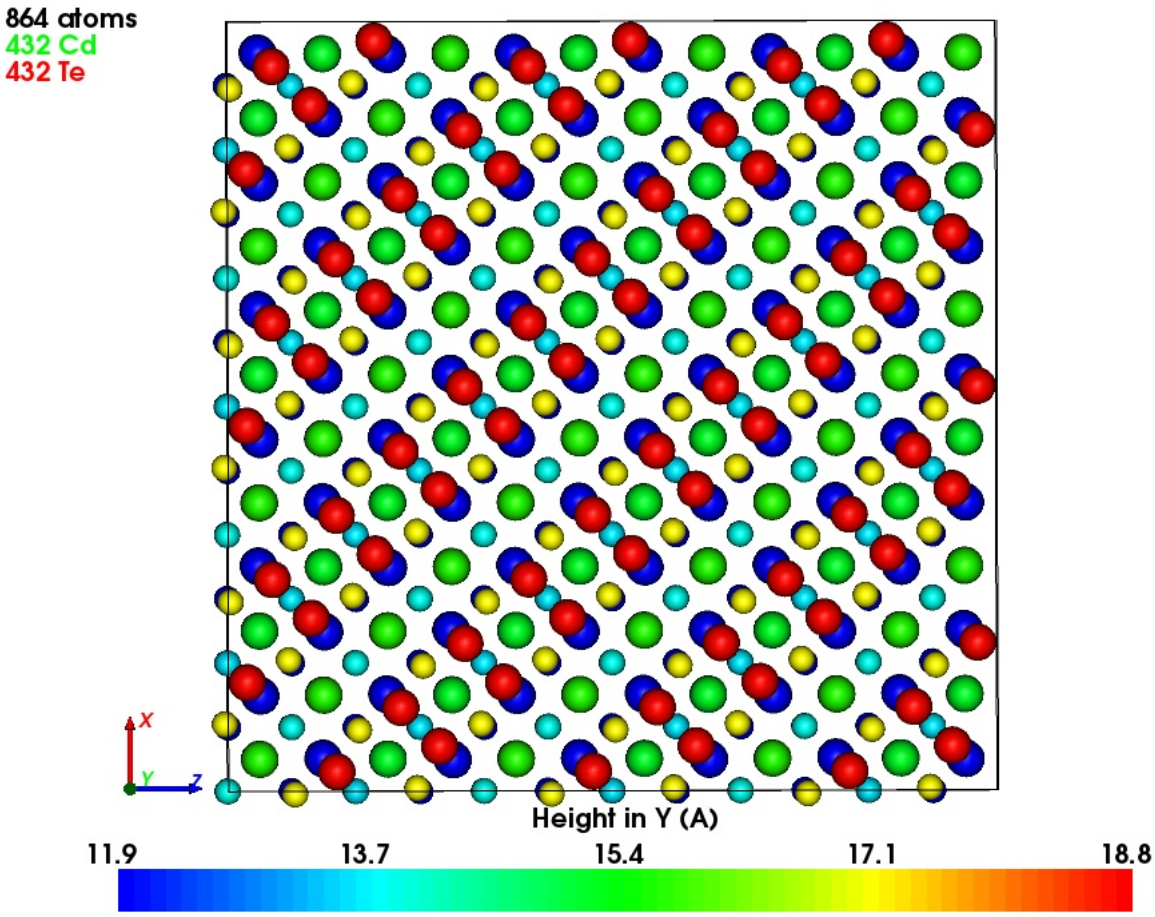


**Figure 7.22:** Top view of the Te-terminated dimerised (100) (2×1) CdTe surface. The surface Te atoms (coloured red) are dimerised, away from their correct sites (coloured dark blue). Graph is coloured by height. Bigger spheres represent the Te atoms, and smaller spheres the Cd atoms.

during the growth.

We try to use OTF-KMC to simulate the growth. However due to the dimerisation of the surface Te layer, all surface Te layer atoms are defects. We use the dimerised positions as the reference to reduce defects during the simulations. But when the surface Te dimer splits to their crystal sites, they will be regarded as defects. Therefore there are far more defects than ones on the (111) surfaces, and we get larger defect volumes on the (100) Te-terminated dimerised surface. As more and more clusters deposited onto the surface, the whole surface become a single big defect volume. The OTF-KMC method we are using searches transitions on each defect volume. Larger the defect volume is, harder the successful transitions to be found. The simulation end up with spending too much time on transition searchings with few depositions. We decide to use MD to simulate the growth on (100) Te-terminated dimerised surfaces.

The attainable simulation time for MD is limited. It is very hard to reach nanoseconds even for a small system. Clearly it is not feasible to simulate the growth over realistic time scales by using MD. We have to use an accelerated deposition rate for the MD simulations. In each step of our simulations, first we heat the whole system for 9 ps to reach the desired temperature, then deposit a CdTe cluster onto the surface and continue MD for 10 ps to finish the impact, and at last relax the system to reach equilibrium.

Because the MD calculations are serial, all simulations are done on a single CPU core per simulation. We end up with a complete new layer and two incomplete layers for two weeks of simulations.

### 7.2.2 Simulation Results

In this work, the thin film growth simulations for the (100) surfaces are undertaken on the Te-terminated dimerised surfaces. During the simulations, the temperature is set to be $T = 350$ K which is the same as the growth simulations for (111) surfaces. We also undertake several simulations with different deposition energies at 0.1 eV, 1 eV and 10 eV, respectively.

Despite different deposition energies, we get similar results from our simulations. The results show that the deposited CdTe clusters usually sit above the original surface. The Te atoms could penetrate to the original surface layer and become interstitials. As more and more atoms be deposited on the surface, a new double-

layer begin to form and the Te dimers underneath split and move to their correct sites. Once the first new double-layer is complete, almost all of the Te dimers on the original surface layer split and move to their correct sites.

Figure 7.23 show the result of CdTe thin film growth on Te-terminated dimerised (100) surface with deposition energy 10 eV at the temperature 350 K. There is a complete new double-layer (coloured green) and two incomplete new double-layers (coloured yellow and red) in the example. The second new double-layer is 70% complete, and there are only 5% of atoms in the third new layer. The result shows that there are a few Te interstitials in the original surface double-layer (coloured blue). Almost all the Te dimers disappear and they move to their correct sites. It is very clear that half of the atoms in the first new double-layer have a clear pattern, which indicates they are at their correct sites. However we do not observe a clear pattern of atoms in the top two new double-layers.

We count the number of defects in each double-layer of the final lattices for each simulation, in order to investigate how the deposition energies affect the CdTe thin film growth. Figure 7.24 shows the results. We focus on the results in the first and second new double-layers, because the first new double-layer is complete and the second one is over 70% filled. However there are too few atoms in the third new layer and we cannot draw conclusions for them. The result shows that, the number of defect decreases as the deposition energy increases. Probably because when the second double-layer begin to form, high deposition energy provide enough energies for the deposited cluster to penetrate the second double-layer to fill vacancies in the first double-layer.

### 7.2.3 Annealing

The post annealing is applied to all the Te-terminated dimerised (100) surface growth simulations. We anneal the system at 500 K, 600 K and 650 K, respectively, for 5 ns. The annealing process is helpful to reduce the defects. We want to find out how the temperature affects the process.

We define the off-site atoms as atoms not sit in their crystal sites, i.e. either interstitials or antisites. We count the number of off-site atoms in each double-layer for all systems pre- and post-annealing. Detail data table is given in Appendix C and a bar chart is shown in Figure 7.25.

During the annealing process, we dump out the system for every 1 ps for analysis

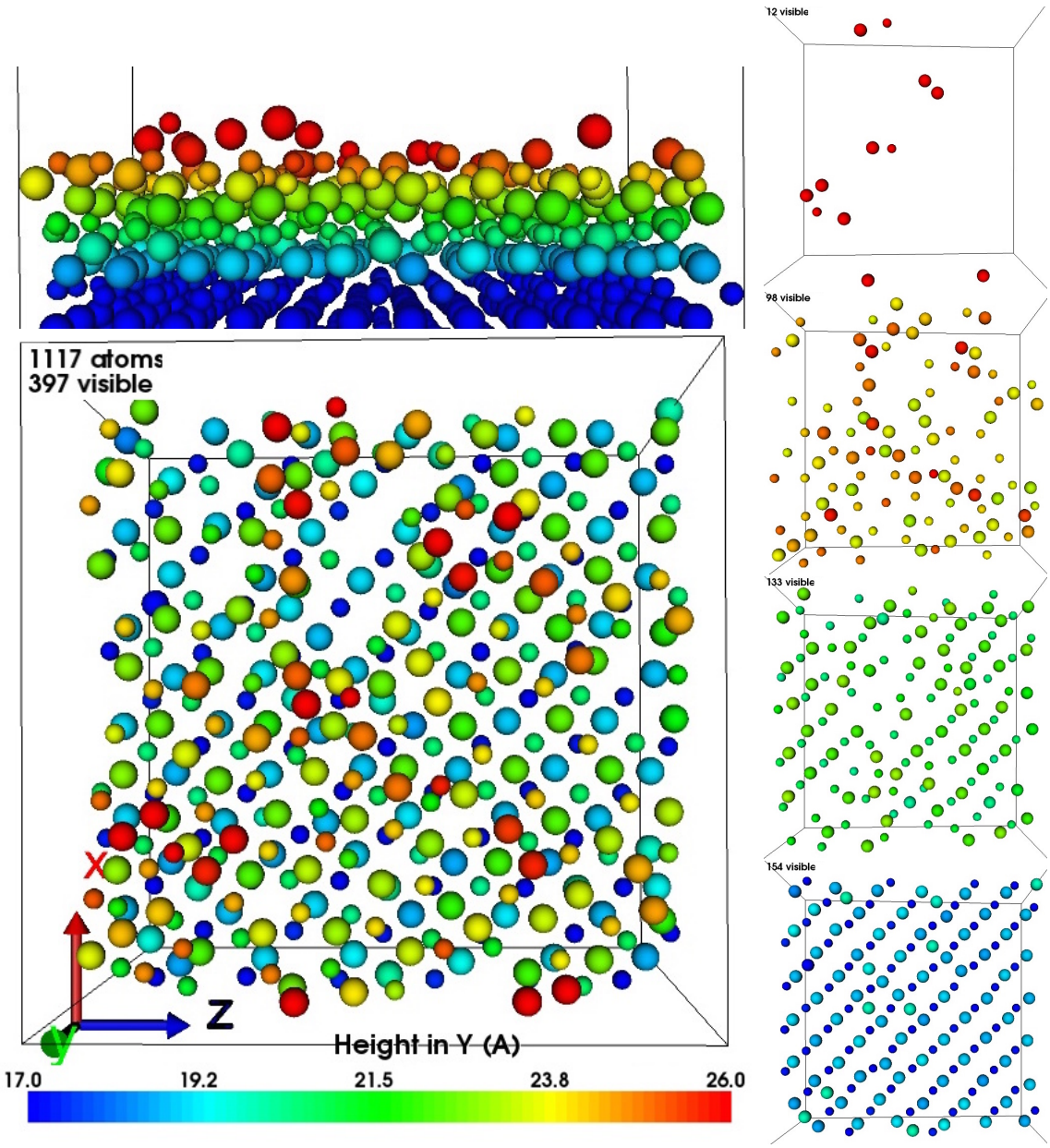


**Figure 7.23:** CdTe thin film growth on Te-terminated dimerised (100) surface. The deposition energy is 10 eV. A front view (upper left) and a top view (lower left) of the surface and new double-layers are presented on the left. Four graphs on the right shows the third new double-layer, the second new double-layer, the first new double-layer and the original surface double-layer, respectively. There are several Te interstitials on the original surface layer (coloured blue) and Te dimers disappear. We get a complete new double-layer (coloured green) with a few defects and two incomplete double-layers (coloured yellow and red). Graphs are coloured by height. Bigger spheres represent the Te atoms, and smaller spheres the Cd atoms.

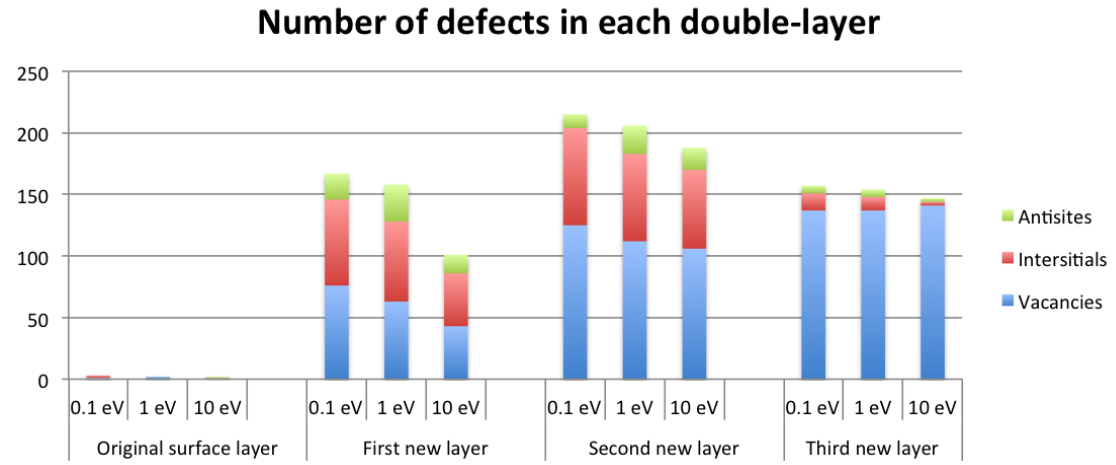


**Figure 7.24:** Number of defects in each double-layer with different deposition energies.

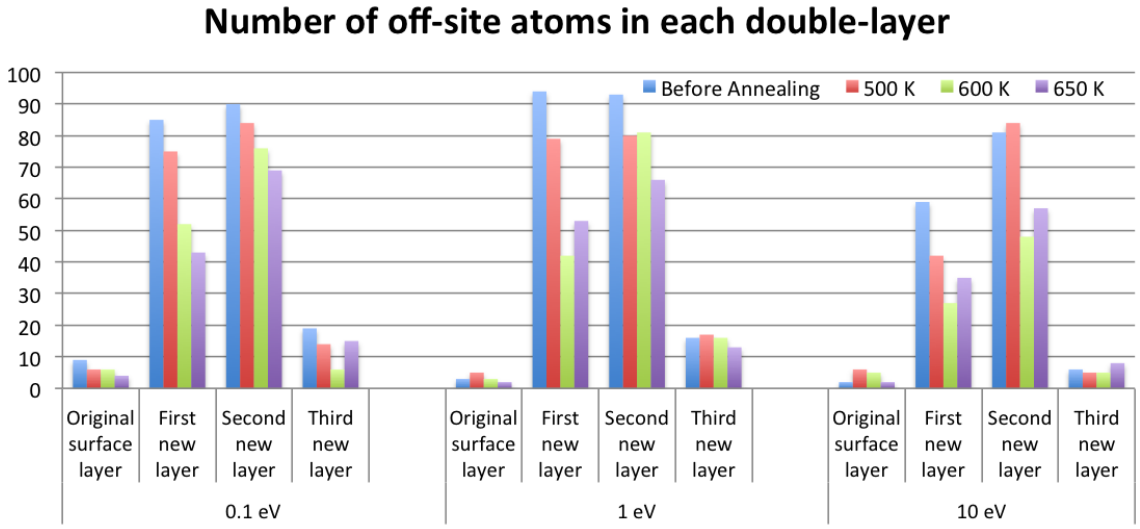


**Figure 7.25:** Number of off-site atoms in each double-layer.

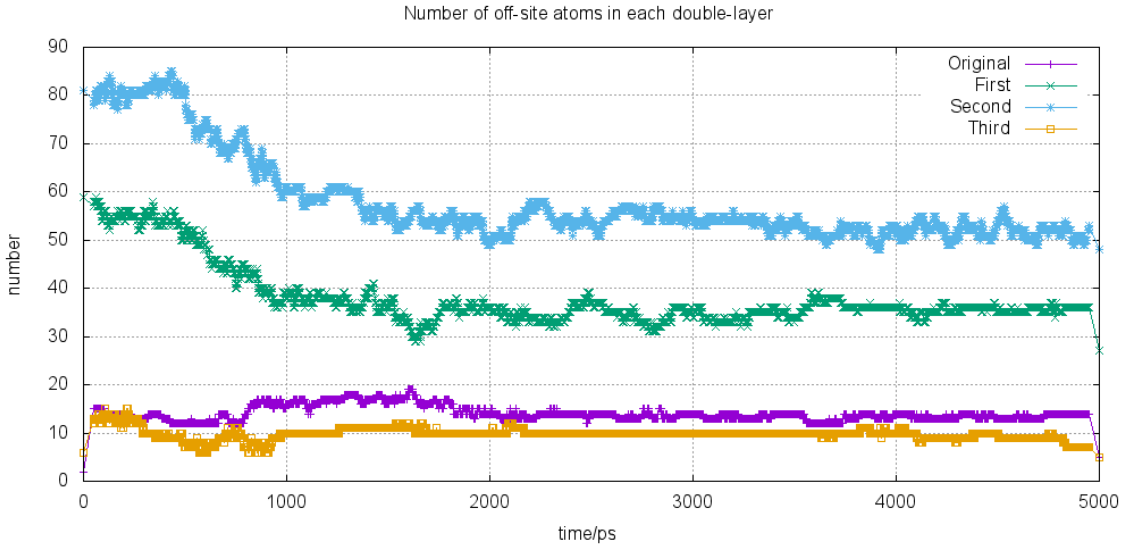


**Figure 7.26:** Number of off-site atoms in each double-layer during annealing. Post-annealing is applied to the system with deposition energy 10 eV at the temperature of 600 K for 5 ns.

and calculate the average positions for every 100 ps to reduce the atomic vibrations. We then apply defect analysis to the averaged systems. Figure 7.26 shows the how the number of off-site atoms in each double-layer changes during the post-annealing process. It is clear that the post-annealing successfully reduces the number of off-site atoms in the first and second new double-layers. If the annealing simulation goes longer, it the number of off-site atoms should be further reduced.

It is not very clear how the annealing temperature affects the number of off-site atoms in each layer, because atoms can diffuse between layers. We therefore look into the total number of off-site atoms for each case. Figure 7.27 shows that, the annealing process reduces the number of off-site atoms. The number of atoms which move back to their crystal sites increases as the temperature increases. For the total number of off-site atoms, there is no huge differences between 600 K and 650 K.

#### 7.2.3.1 Annealing Mechanism

The post annealing process successfully reduces the number of defects in the newly formed double-layers. We are interested in how these defects are removed during the annealing process. After the deposition, there are several Te interstitials in the original surface layer, and the second and third new double-layers are incom-

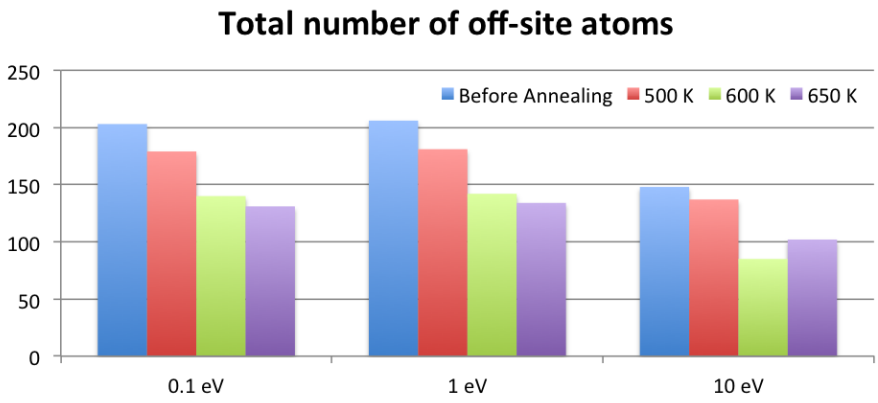


**Figure 7.27:** Total number of off-site atoms.

plete. Therefore we focus on the reduction of defects in the first new double-layer. Figure 7.28 shows the reduction of defects in the first new double-layer before and after annealing.

The result also show that, the defects usually form diagonal chains as highlighted in Figure 7.28b. The defect chains usually consist of several interstitials and vacancies. During the annealing process, the size of this kind of defect chains are reduced. Atoms from other layers, usually from upper layer, drop to fill vacancies, and push a series of interstitials in the diagonal direction to fill corresponding vacancies. We deduce that if we anneal for longer time, the defects will be further reduced.

There are a few Te interstitials in the original surface layer, and some of them are removed during the annealing process. As shown in Figure 7.29, the Te interstitial in the original surface layer pops up to the first new double-layer and becomes an antisites. Then the Te atom diffuses to fill an vacancy near by.

The vacancies in the first new double-layer can also be filled by atoms in the second new double-layer as shown in Figure 7.30. In this example, the Te atom in the second new double-layer drops down to fill the Te vacancy in the first new double-layer. Then the Cd atom in the second new double-layer also drops down the first new double-layer, and then diffuses to fill the Cd vacancy.

The annealing process also reduces antisites. Figure 7.31 shows an example of reduction of antisites. There are several antisites in the highlighted region. The Te and Cd atoms gradually and respectively diffuse away from the antisites to their crystal sites. There is a Te atom from the second new double-layer drops down to fill the Te vacancy due to the reduction of antisite at the same time.

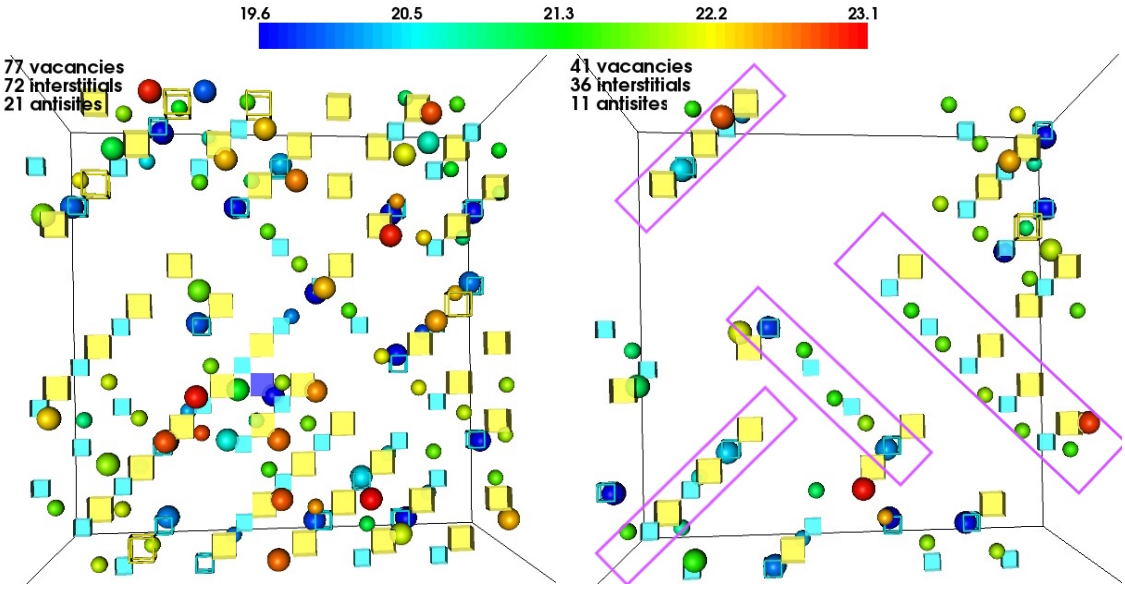


**(a)** Before annealing **(b)** After annealing

**Figure 7.28:** Reduction of defects in the first new double-layer during post-annealing. Deposition energy for the system is 0.1 eV, and the system is annealed at temperature of 650 K for 5 ns. Only defects in the first new double-layer are shown in the graphs. 80 defects are removed during the annealing process. Defects usually form diagonal chains as highlighted in the right graph. Spheres represent interstitials, solid cubes represent vacancies and cube frames represent antisites. Different sizes represent different species, bigger ones represent the Te atoms and smaller ones the Cd atoms. Graphs are coloured by height.

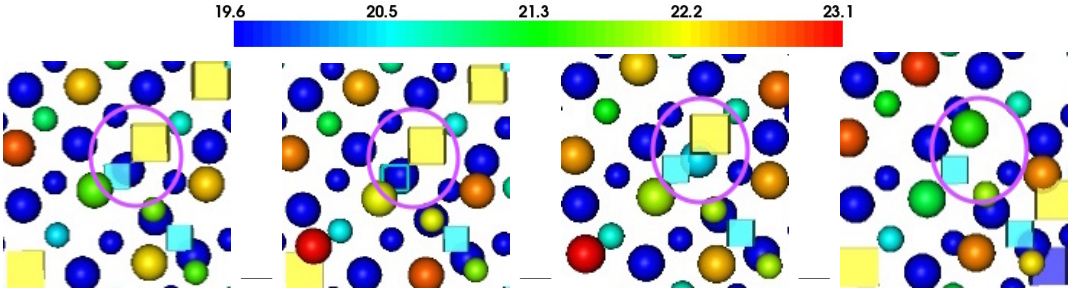


**Figure 7.29:** An Te interstitial in the original layer (bigger dark blue sphere in the highlighted region) pops up and fills an vacancy in the first new double-layer (yellow solid cube in the highlighted region). The barrier calculated by NEB is 0.73 eV. Atoms and defects in the original surface double-layer and the first new double-layer are shown in the graphs. Spheres represent atoms/interstitials, solid cubes represent vacancies and cube frames represent antisites. Different sizes represent different species, bigger ones represent the Te atoms and smaller ones the Cd atoms. Graphs are coloured by height.

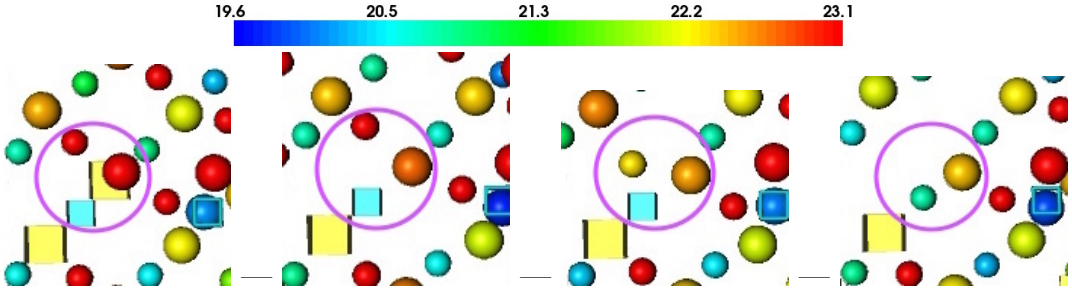


**Figure 7.30:** A CdTe cluster in the second new double-layer (red spheres in the highlighted region) drops down and fills vacancies in the first new double-layer (two solid cubes in the highlighted region). The barrier calculated by NEB is 0.27 eV. Atoms in the first and second new double-layers together with defects in the first new double-layer are shown in the graphs. Spheres represent atoms/interstitials, solid cubes represent vacancies and cube frames represent antisites. Different sizes represent different species, bigger ones represent the Te atoms and smaller ones the Cd atoms. Graphs are coloured by height.

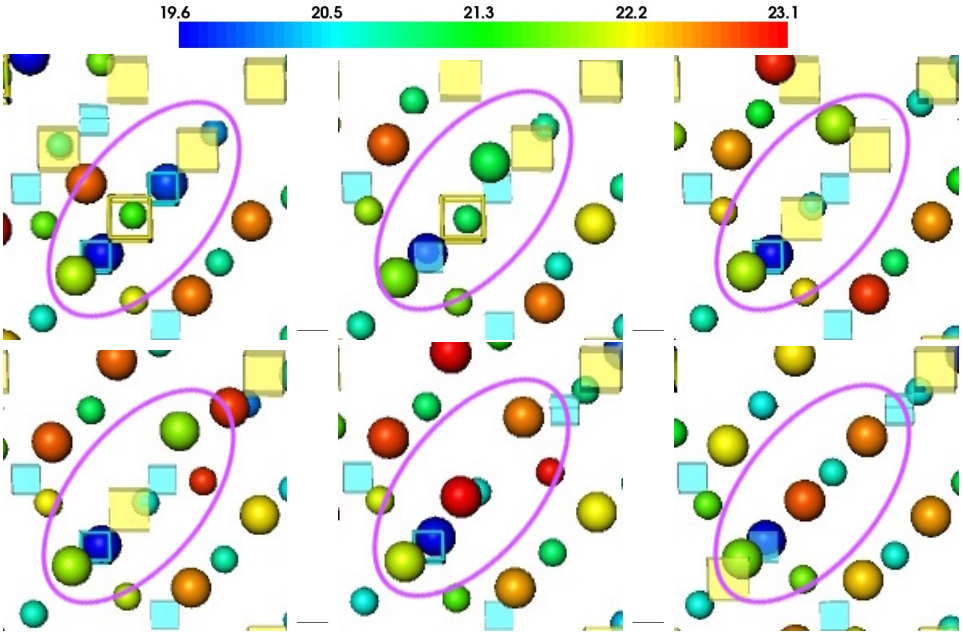


**Figure 7.31:** A series of Cd/Te atoms (in the highlighted region) diffuse from antisites to their crystal sites in the first new double-layer. The barrier calculated by NEB is 1.56 eV. Atoms and defects in the first new double-layer are shown in the graphs. Spheres represent atoms/interstitials, solid cubes represent vacancies and cube frames represent antisites. Different sizes represent different species, bigger ones represent the Te atoms and smaller ones the Cd atoms. Graphs are coloured by height.

## 7.3 Conclusions

With the help basin method to accelerate the OTF-KMC simulations, we get upto half-filled new layers on the (111) surfaces. As the new deposited clusters become bigger and bigger, the defect volume based OTF-KMC algorithm becomes less and less efficiency. Because eventually we will get one single defect volume contains the entire new layers. It's more difficult to search for saddles points in a larger defect volume.

The deposited CdTe cluster usually stick together on the (111) Te-terminated surfaces, while they might dissociate on the Cd-terminated surfaces. Thus the clusters on the (111) Te-terminated surfaces are stoichiometric, but they can be non-stoichiometric on the (111) Cd-terminated surfaces.

The growth process are very similar on both Te- and Cd-terminated (111) surfaces. The small CdTe clusters or Cd/Te atoms diffuse around the surface, until they meet other cluster/atom to form a bigger cluster which is less mobile. Barriers of transitions for single Cd/Te atom and CdTe clusters indicate that, the single Cd atom is more mobile than single Te atom. They also show that clusters on the (111) Cd-terminated surfaces are more mobile than on Te-terminated ones.

On the (111) Te-terminated surfaces, the deposited CdTe clusters "lie down" on the surface, i.e. both Cd and Te atoms are at the same height and they stay in the same layer. The deposited clusters usually in a zig-zag chain shape. In clusters of 4 or more atoms, the Te atoms could move out of the initial layer to form a new layer, therefore forms a double-layer. The atoms being "pushed" to the second layer are so mobile that they may dominate the simulations. Such atoms in the second layer could also "drop" back to the first layer. The simulation results show that atoms above the double-layer is also helpful to "keep" Te atoms in the first double-layer at their correct heights.

On the (111) Cd-terminated surfaces, the deposited CdTe clusters "stand up" on the surface, i.e. Cd and Te atoms are at different heights as expected. The new double-layers are formed with the depositions. Diffusions on the (111) Cd-terminated surfaces are more rapidly than on Te-terminated surfaces. We also observe the dissociation of CdTe clusters, which is not seen on the (111) Te-terminated surfaces. Clusters are usually in (double) line chain shapes.

In conclusion, at the room temperature, the deposition energy (0.1∼10 eV) does not change the film growth mechanism. However the species of surface atoms mat-

ters. The Te layers "attract" deposited clusters more than Cd layers, which causing the differences of growth mechanisms on two surfaces.

We use MD to simulate the CdTe thin film growth on the Te-terminated dimerised (100) surfaces. The results show that Te dimers on the original surface layer split and move to their crystal sites during the growth. While the first new double-layer start to form, the Te dimers underneath are able to split.

The growth simulations on the Te-terminated dimerised (100) surfaces are undertaken with deposition energies vary from 0.1 eV to 10 eV. The results show that, higher the deposition energy is, fewer the defects are in the new formed layers.

We anneal the systems after the depositions at temperature vary from 500 K to 650 K. The annealing process successfully reduces the number of defects in the system, and higher the temperature is, more defects are removed.

# Chapter 8

# Conclusions and Future Work

## 8.1 Summary and Conclusions

The aim of this work is to model the CdTe thin film growth of various conditions over realistic time scales. The magnetron sputtering technique, which is widely used in CdTe thin film production, was modelled in order to understand the role of different experimental conditions on the resulting thin film qualities. Computer simulations are able to optimise experimental conditions without real life experiments, which require time and cost money. Moreover simulations allow a more precise understanding of the effect of different conditions on the resulting thin film growth. This work aimed to provide an understanding of the mechanisms observed during the growth.

The potentials used throughout this work are the analytical bond-order potentials for CdTe. The CdTe lattice properties, such as optimal lattice constants and elastic constants, and defect energies are tested and compared with other potentials. Energy differences causing by the stacking faults are also investigated. The BOPs are good enough to accurately describe the interactions between Cd and Te atoms.

In order to gain understanding of the behaviour of the CdTe surfaces, over a thousand single molecule depositions were performed using MD for each condition. Three different clusters are deposited onto four different CdTe surfaces with deposition energies vary from 1 eV to 40 eV at random positions. The results show that **Cd atoms are more readily sputtered than Te atoms, and the sticking probability is higher for the Te-terminated surfaces than the Cd-terminated ones.** The results also show that increasing the deposition energy typically leads

to an increase in the number of atoms sputtered from the system. It also tends to decrease the number of atoms that sit on or in the surface layer, whilst increasing the number of interstitials observed. The results also show that it is more difficult for the deposited clusters to penetrate the (111) surfaces than the (100) ones. But on the other hand, it is easier to be reflected on the (111) surfaces than the (100) ones. These facts indicate that **the double-layer structure in the (111) surfaces are more stable than the single layer structure in the (100) surfaces**. When the CdTe cluster is deposited, if it sticks on the surface it usually dissociates at higher energies, while it prefers a soft-landing at low energies. When a single Cd/Te atom is deposited on a surface, **the species of surface atoms affect the behaviour of the deposited atoms.** On the surface, the probability to join the 1st layer is larger if we deposit the same species as the surface atoms than a different species. While the probability to sit on the surface is lower if we deposit the same species as the surface atoms than a different species. The single molecule deposition simulations provide an initial insight into the film growth. Later in the thin film growth simulations, the CdTe clusters are chosen to be the deposition cluster.

The mechanisms of CdTe thin film growth on different surfaces are quite different. We simulated the thin film growth on the (111) Cd- and Te-terminated surfaces and the (100) Te-terminated dimerised surfaces. Since the thin film growth occurs over much longer time scales than can be modelled by using traditional MD methods, the OTF-KMC, one of the LTSD techniques, with superbasin method is used to simulate over longer time scales.

The OTF-KMC method is implemented in conjunction with Chris Scott[122] and Tomas Lazauskas[86] using the programming language Python. I implemented the superbasin method, which is proven to be an efficient method to overcome low-barrier transition problems, into the OTF-KMC and I also in charge of the code which allows the OTF-KMC to do depositions using MD. The superbasin method regards states which are connected with low-barrier transitions as a single object – a superbasin – and provide accurate average escaping time, therefore the OTF-KMC simulations can get out of the superbasins quickly without repeated hopping between low-barrier connected states. Colleagues in our group have applied the superbasin method to their OTF-KMC simulations, such as ZnO/Ag film growth and radiation damage in Fe. **The superbasin method successfully speed up their simulations, and they have been shown to provide realistic, accurate results.**

The OTF-KMC with superbasin method is used to simulate CdTe thin film growth on the (111) Cd- and Te-terminated surfaces. The growth simulations started with four/three CdTe clusters being deposited onto the Cd-/Te-terminated surfaces. Despite different deposition energies vary from 0.1 eV to 10 eV, the thin film growth mechanisms are very similar. The results show that single atoms and small ad-atom clusters are highly mobile on the surface. Single Cd/Te atoms or small CdTe clusters diffuse rapidly on the surface until they meet other clusters and form a bigger cluster which is less mobile. The diffusivity is significantly reduced at the size of clusters contain at least 4 atoms, as we do not observe any transitions of movements for more than four atoms. The single Cd atom is more mobile than single Te atom and clusters on the (111) Cd-terminated surfaces are more mobile than on Te-terminated ones. However the detailed growth mechanisms on Cd- and Te-terminated surfaces are different. On the (111) Cd-terminated surfaces, the deposited CdTe clusters stand up on the surface, and the new double-layers are formed together with the depositions. Line chain shape clusters are observed during the simulations. On the other hand, on the (111) Te-terminated surfaces, the deposited CdTe clusters lie down on the surface. Both Cd and Te atoms stay at the same layer, while the double-layer structure is formed later when bigger clusters are formed. Zig-zag chain shape clusters are observed during the simulations. We conclude that at the room temperature, **the deposition energy does not change the thin film growth mechanisms much on the (111) CdTe surfaces**, however the species of surface atoms matters. **The Te layers attract deposited clusters more than Cd layers**, where the single molecule deposition test results also supported.

The OTF-KMC method is not valid when simulating the CdTe thin film growth on the (100) Te-terminated dimerised surfaces, due to the large number of defects created because of the Te dimerisation on the surface. Therefore we use the MD method with accelerated deposition rate to simulate the thin film growth **on the (100) Te-terminated dimerised surfaces**. The deposition energy varies from 0.1 eV to 10 eV. The simulation results show that **higher deposition energy gives better new layers with fewer defects**. Probably because when the second double-layer begin to form, high deposition energy provide enough energies for the deposited cluster to penetrate the second double-layer to fill vacancies in the first double-layer. The results also show that **when the new layers start to form, the Te dimers underneath split and move to their crystal sites**. Once the first new double-layer is complete, almost all of the Te dimers on the original surface

layer split and move to their correct sites. To further reduce defects, post annealing is applied at temperature varies from 500 K to 650 K. **The post annealing successfully reduced the number of off-site atoms in the newly formed layers**. During the annealing process, line chain shape defects are observed. The defects are usually reduced by "attracting" interstitials from other layers to fill the vacancies, and/or "pushing" the interstitials in the same layer along the defect line chain direction to fill the vacancies.

This work has provided an excellent insight into the CdTe thin film growth with different conditions. Single molecule deposition tests explained the reason why the growth mechanisms on Cd- and Te-terminated surfaces are different. OTF-KMC with superbasin method provided a precise understanding of the process during the thin film growth. Specific transitions of the growth mechanisms are studied on each surface to understand how the thin film growths. MD studies on the annealing process provides an insight into the defect reduction. The computer simulations provide the insight of thin film growth mechanisms where the real life experiments cannot do. They become ideal partners with experiments.

## 8.2 Future Work

Though the superbasin method works well in most cases, there are several modifications which is necessary for further improvement of the developed OTF-KMC technique. In the superbasin method, we use the hash key of a defect volume (DV) as a label. Sometimes a small movement of the atoms, especially atoms near the boundary of DVs, can result in different hash keys. In this case, several hash keys are associated with the same configuration of a DV. This will cause a problem in the superbasin method while it trying to translate between superbasin states. Currently in the code, we compare positions of all atoms in the DVs and store the additional hash keys as secondary hash keys. The future improvement may also include storing all transition associated with the secondary hash keys.

Another possible improvement for the superbasin method is to revise and build translations between superbasin states. Currently the superbasin method build reverse transitions for low-barrier transitions to ensure the superbasin states are connected. During the simulations, we sometimes notice that the connectivity is not symmetric. For example, we may have two transitions hopping from superbasin

state 1 to 2, but there may be only one transition hops back. There may be missing transitions or duplicated transitions between superbasin states. Further work on checking superbasin connectivities should be done in the future.

The superbasin method requires several KMC steps to construct and exit the superbasins. Thus the configurations of systems at every end of KMC steps are no longer how the simulations evolve. The process of constructing superbasins is meaningless to the simulations, because we only care about where and how the simulations exit the superbasin. Future improvement can be done by only visualising systems at KMC steps which are not constructing superbasins, and also visualise how the simulations exit the superbasins.

As for the CdTe thin film growth simulations, we still do not get any complete new layers in the simulations of thin film growth on the (111) surfaces. The superbasin method is able to speed up the OTF-KMC simulations, but not enough. We need other techniques to speed up the simulations further.

In this work, our simulations are based on magnetron sputtering technique. There are many other thin film growth techniques such as closed space sublimation (CSS). The OTF-KMC technique have the ability to simulate other deposition techniques by altering the parameters. For example, CSS requires high temperature, and pulsed laser deposition can be simulated by applying short pulses of depositions. In the future, more simulations for different deposition techniques can be undertaken to gain more knowledge of thin film growth. The simulations results are helpful for the experimentalists to know what happened during the growth, and therefore find possible improvements.

# Appendix A

# Research Cell Efficiency Records

Large print of Figure 1.1: Chart of research cell efficiency records over years. Blue curves represent the efficiency records of the crystalline silicon cells, and green curves the efficiency records of the thin-film technologies. Yellow dots with green boundaries represent for the efficiency records of the CdTe thin film cells. The efficiencies improved over the years, but thin-film PVs are still less efficient than crystalline silicon cells. Chart taken from[12].

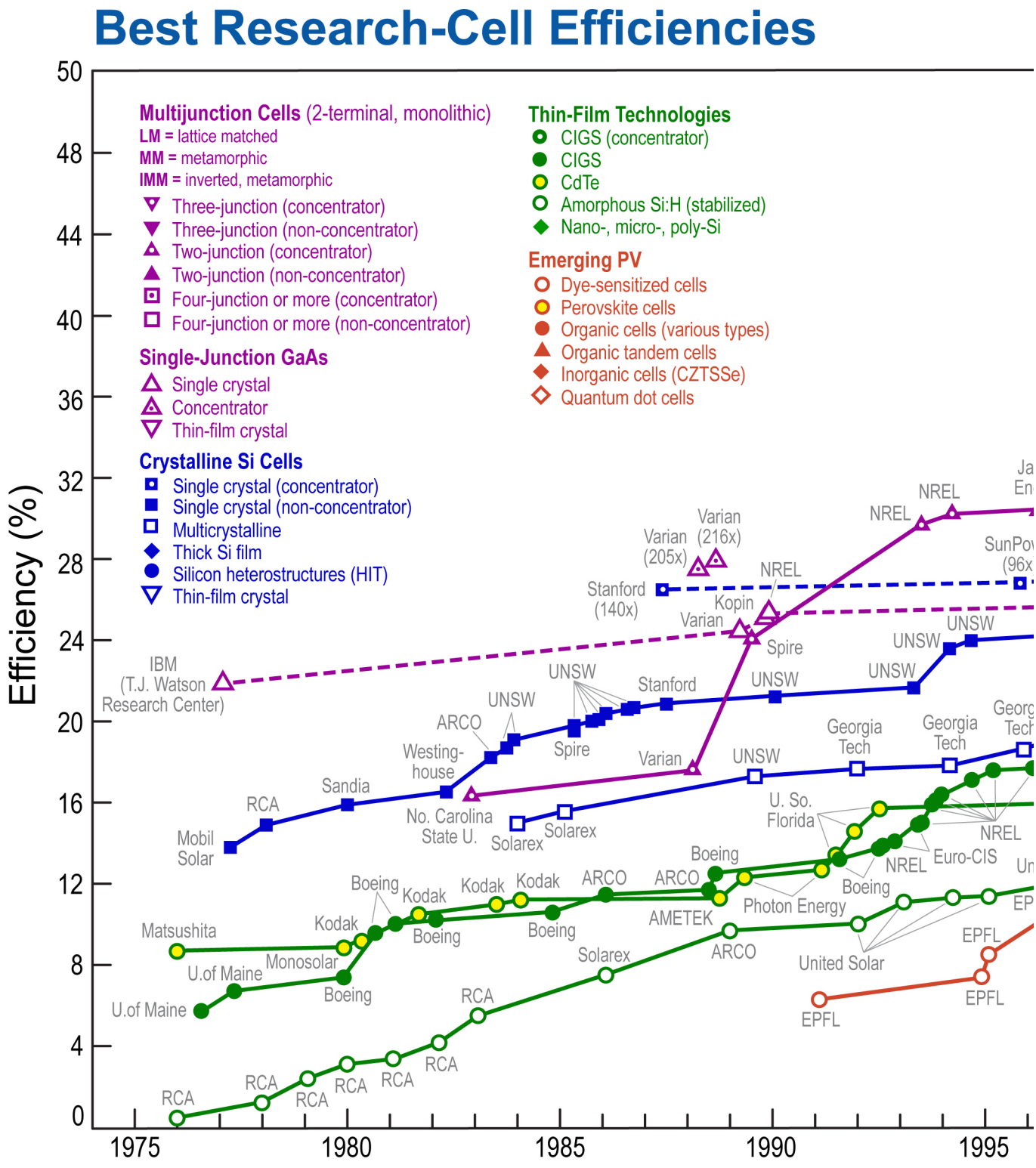
Best Research-Cell Efficiencies
Efficiency (%)
50
48
44
40
36
32
28
24
20
16
12
8
4
0
1975
1980
1985
1990
1995
Multijunction Cells (2-terminal, monolithic)
LM = lattice matched
MM = metamorphic
IMM = inverted, metamorphic
Three-junction (concentrator)
Three-junction (non-concentrator)
Two-junction (concentrator)
Two-junction (non-concentrator)
Four-junction or more (concentrator)
Four-junction or more (non-concentrator)
Single-Junction GaAs
Single crystal
Concentrator
Thin-film crystal
Crystalline Si Cells
Single crystal (concentrator)
Single crystal (non-concentrator)
Multicrystalline
Thick Si film
Silicon heterostructures (HIT)
Thin-film crystal
Thin-Film Technologies
CIGS (concentrator)
CIGS
CdTe
Amorphous Si:H (stabilized)
Nano-, micro-, poly-Si
Emerging PV
Dye-sensitized cells
Perovskite cells
Organic cells (various types)
Organic tandem cells
Inorganic cells (CZTSSe)
Quantum dot cells
IBM (T.J. Watson Research Center)
Mobil Solar
RCA
Sandia
Westing-house
ARCO
UNSW
Spire
Stanford
No. Carolina State U.
Solarex
Varian (205x)
Varian (216x)
Stanford (140x)
Kopin
Varian
NREL
SunPo (96x
Ja En
UNSW
Georgia Tech
Georg Tech
U. So. Florida
Euro-CIS
Boeing
Photon Energy
AMETEK
Matsushita
Monosolar
U.of Maine
Kodak
United Solar
EPFL
Solarex

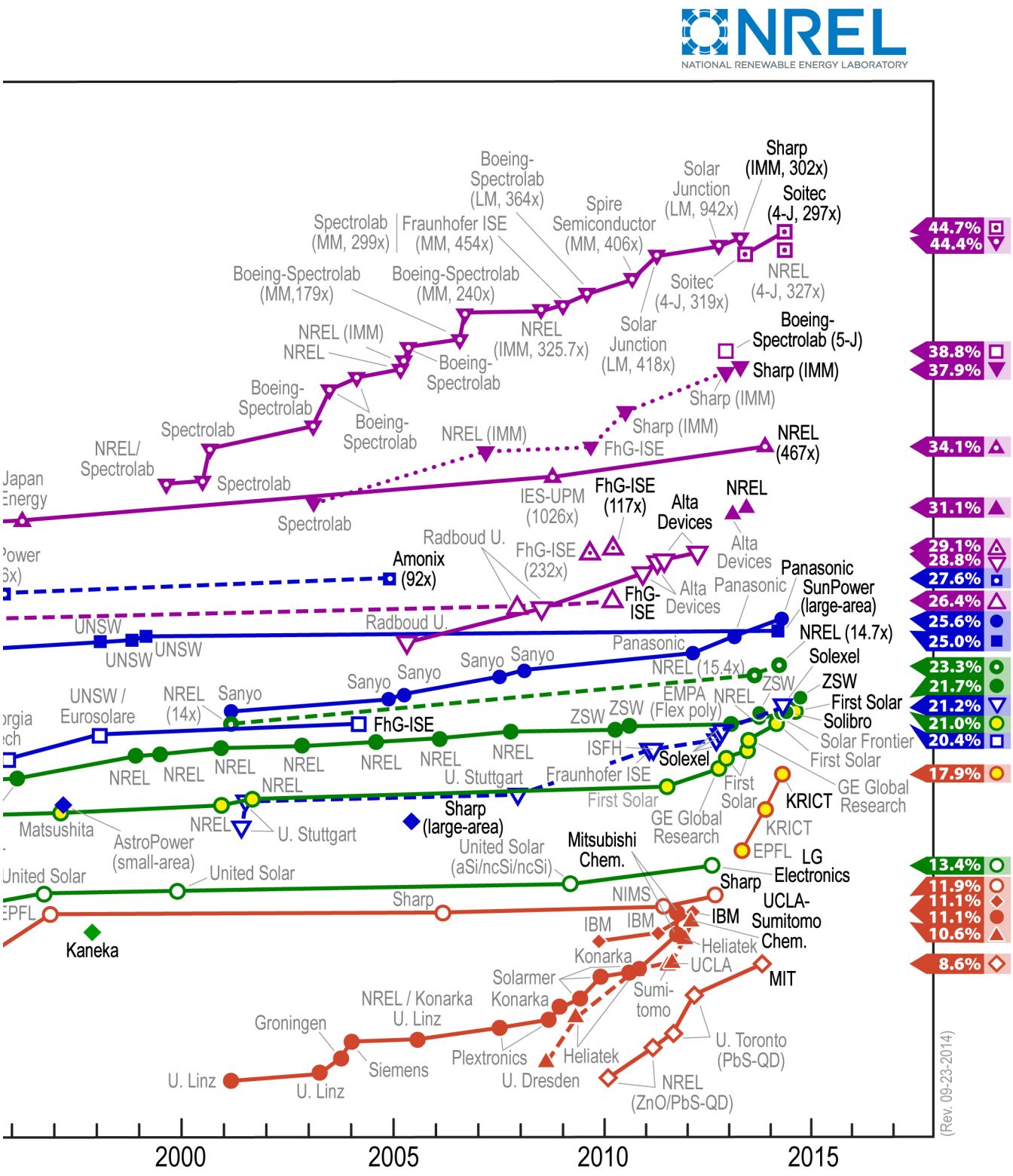
NREL
NATIONAL RENEWABLE ENERGY LABORATORY
Sharp (IMM, 302x)
Soitec (4-J, 297x)
Boeing-Spectrolab (LM, 364x)
Solar Junction (LM, 942x)
Spire Semiconductor (MM, 406x)
Spectrolab (MM, 299x)
Fraunhofer ISE (MM, 454x)
Boeing-Spectrolab (MM,179x)
Boeing-Spectrolab (MM, 240x)
Soitec (4-J, 319x)
NREL (4-J, 327x)
NREL (IMM)
NREL
NREL (IMM, 325.7x)
Solar Junction (LM, 418x)
Boeing-Spectrolab (5-J)
Sharp (IMM)
Boeing-Spectrolab
Boeing-Spectrolab
Sharp (IMM)
Spectrolab
NREL/ Spectrolab
Boeing-Spectrolab
NREL (IMM)
Sharp (IMM)
FhG-ISE
NREL (467x)
Japan Energy
Spectrolab
Spectrolab
IES-UPM (1026x)
FhG-ISE (117x)
Alta Devices
NREL
Radboud U.
Alta Devices
Amonix (92x)
FhG-ISE (232x)
Panasonic
SunPower (large-area)
FhG-ISE
Alta Devices
Panasonic
UNSW
Radboud U.
NREL (14.7x)
UNSW
UNSW
Panasonic
Sanyo
Sanyo
Sanyo
NREL (15.4x)
Solexel
UNSW / Eurosolare
NREL (14x)
Sanyo
Sanyo
ZSW
ZSW
EMPA (Flex poly)
NREL
First Solar
FhG-ISE
ZSW
Solibro
Solar Frontier
First Solar
ISFH
Solexel
NREL
NREL
NREL
NREL
NREL
NREL
NREL
NREL
U. Stuttgart
Fraunhofer ISE
First Solar
First Solar
GE Global Research
KRICT
Matsushita
AstroPower (small-area)
NREL
U. Stuttgart
Sharp (large-area)
GE Global Research
KRICT
EPFL
United Solar
United Solar (aSi/ncSi/ncSi)
Mitsubishi Chem.
LG Electronics
United Solar
United Solar
Sharp
NIMS
Sharp
UCLA-
IBM
IBM
Sumitomo Chem.
Heliatek
Kaneka
Konarka
UCLA
MIT
Solarmer
Konarka
Sumi-tomo
NREL / Konarka
U. Linz
Groningen
U. Toronto (PbS-QD)
Plextronics
Heliatek
Siemens
U. Linz
U. Linz
U. Dresden
NREL (ZnO/PbS-QD)
44.7%
44.4%
38.8%
37.9%
34.1%
31.1%
29.1%
28.8%
27.6%
26.4%
25.6%
25.0%
23.3%
21.7%
21.2%
21.0%
20.4%
17.9%
13.4%
11.9%
11.1%
11.1%
10.6%
8.6%
2000
2005
2010
2015
(Rev. 09-23-2014)

# APPENDIX A. RESEARCH CELL EFFICIENCY RECORDS

# Appendix B

# Single Deposition Result Data

Details of single deposition result data mentioned in Chapter 5 are presented here. All data in the following tables are in percentage. E.g. 19.8±1.1 means 19.8% of the tests fall into this category with standard error 1.1%. Illustration of categories in the following tables is shown in Figure 5.3.

| (100) Cd-terminated surface | | | | | | | | |
|---|---|---|---|---|---|---|---|---|
| Deposited cluster | Cd | | | | Te | | | |
| Deposition energy | 1 eV | 10 eV | 20 eV | 40 eV | 1 eV | 10 eV | 20 eV | 40 eV |
| Reflect | 19.8±1.1 | 14.6±0.9 | 10.9±0.8 | 9.1±0.8 | 1.±0.3 | 0.2±0.1 | 0.3±0.1 | 1.4±0.3 |
| Sputter | 0.±0. | 4.8±0.6 | 17.5±1. | 35.1±1.3 | 0.±0. | 2.8±0.4 | 11.4±0.8 | 32.±1.2 |
| Sit on | 0.4±0.2 | 0.7±0.2 | 0.9±0.3 | 0.8±0.2 | 79.8±1.1 | 23.3±1.1 | 8.2±0.7 | 2.3±0.4 |
| Penetrate | 0.1±0.1 | 23.8±1.1 | 31.5±1.2 | 24.5±1.1 | 0.±0. | 33.7±1.3 | 42.9±1.3 | 36.6±1.3 |
| Join 1st layer | 79.7±1.1 | 55.±1.3 | 32.±1.2 | 17.±1. | 19.2±1.1 | 20.3±1.1 | 10.8±0.8 | 3.8±0.5 |
| Dissociate | 0.±0. | 0.±0. | 0.±0. | 0.±0. | 0.±0. | 0.±0. | 0.±0. | 0.±0. |
| Replace | 0.±0. | 1.1±0.3 | 7.1±0.7 | 13.5±0.9 | 0.±0. | 19.6±1.1 | 26.5±1.2 | 24.±1.1 |

| (100) Te-terminated dimerlized surface (2x1) | | | | | | | | |
|---|---|---|---|---|---|---|---|---|
| Deposited cluster | Cd | | | | Te | | | |
| Deposition energy | 1 eV | 10 eV | 20 eV | 40 eV | 1 eV | 10 eV | 20 eV | 40 eV |
| Reflect | 5.5±0.7 | 13.1±1. | 12.5±1. | 10.±0.9 | 0.±0. | 0.7±0.3 | 2.5±0.5 | 2.1±0.4 |
| Sputter | 0.5±0.2 | 0.7±0.3 | 3.7±0.6 | 21.5±1.3 | 0.±0. | 1.3±0.4 | 5.1±0.7 | 19.7±1.2 |
| Sit on | 66.±1.5 | 52.5±1.5 | 32.8±1.4 | 11.8±1. | 1.6±0.4 | 2.±0.4 | 2.3±0.5 | 1.3±0.4 |
| Penetrate | 21.9±1.3 | 24.2±1.3 | 30.±1.4 | 26.6±1.4 | 8.7±0.9 | 38.6±1.5 | 41.6±1.5 | 31.3±1.4 |
| Join 1st layer | 1.±0.3 | 2.1±0.4 | 1.9±0.4 | 1.3±0.4 | 89.7±0.9 | 46.2±1.5 | 24.2±1.3 | 7.8±0.8 |
| Dissociate | 0.±0. | 0.±0. | 0.±0. | 0.±0. | 0.±0. | 0.±0. | 0.±0. | 0.±0. |
| Replace | 5.1±0.7 | 7.4±0.8 | 19.±1.2 | 28.8±1.4 | 0.±0. | 11.2±1. | 24.2±1.3 | 37.8±1.5 |

| | (111) Cd-terminated surface | | | | | | | |
|---|---|---|---|---|---|---|---|---|
| Deposited cluster | Cd | | | | Te | | | |
| Deposition energy | 1 eV | 10 eV | 20 eV | 40 eV | 1 eV | 10 eV | 20 eV | 40 eV |
| Reflect | 75.3±1.3 | 36.1±1.5 | 21.3±1.2 | 3.3±0.5 | 0.±0. | 0.8±0.3 | 3.1±0.5 | 1.6±0.4 |
| Sputter | 0.±0. | 13.1±1. | 26.±1.3 | 37.2±1.5 | 0.±0. | 1.9±0.4 | 7.7±0.8 | 30.9±1.4 |
| Sit on | 24.7±1.3 | 5.9±0.7 | 6.±0.7 | 1.4±0.4 | 100.±0. | 41.1±1.5 | 29.4±1.4 | 8.3±0.8 |
| Penetrate | 0.±0. | 16.5±1.1 | 12.4±1. | 17.±1.1 | 0.±0. | 11.5±1. | 11.9±1. | 15.2±1.1 |
| Join 1st layer | 0.±0. | 24.1±1.3 | 23.6±1.3 | 13.7±1. | 0.±0. | 9.±0.9 | 15.4±1.1 | 9.3±0.9 |
| Dissociate | 0.±0. | 0.±0. | 0.±0. | 0.±0. | 0.±0. | 0.±0. | 0.±0. | 0.±0. |
| Replace | 0.±0. | 4.4±0.6 | 10.7±0.9 | 27.4±1.3 | 0.±0. | 35.6±1.4 | 32.5±1.4 | 34.7±1.4 |

| | (111) Te-terminated surface | | | | | | | |
|---|---|---|---|---|---|---|---|---|
| Deposited cluster | Cd | | | | Te | | | |
| Deposition energy | 1 eV | 10 eV | 20 eV | 40 eV | 1 eV | 10 eV | 20 eV | 40 eV |
| Reflect | 0.1±0.1 | 13.3±1. | 10.5±0.9 | 11.6±1. | 0.±0. | 0.9±0.3 | 1.3±0.3 | 2.1±0.4 |
| Sputter | 0.±0. | 0.±0. | 1.1±0.3 | 11.2±1. | 0.±0. | 1.±0.3 | 3.1±0.5 | 7.6±0.8 |
| Sit on | 99.9±0.1 | 62.1±1.5 | 31.5±1.4 | 6.9±0.8 | 100.±0. | 34.2±1.4 | 21.2±1.2 | 6.7±0.8 |
| Penetrate | 0.±0. | 8.9±0.9 | 6.3±0.7 | 7.4±0.8 | 0.±0. | 0.6±0.2 | 2.1±0.4 | 8.2±0.8 |
| Join 1st layer | 0.±0. | 2.9±0.5 | 1.±0.3 | 0.3±0.2 | 0.±0. | 2.6±0.5 | 9.±0.9 | 1.4±0.4 |
| Dissociate | 0.±0. | 0.±0. | 0.±0. | 0.±0. | 0.±0. | 0.±0. | 0.±0. | 0.±0. |
| Replace | 0.±0. | 12.8±1. | 49.5±1.5 | 62.6±1.5 | 0.±0. | 60.7±1.5 | 63.3±1.5 | 74.±1.3 |

| | (100) Cd-terminated surface | | | | (100) Te-terminated dimerlized surface (2x1) | | | |
|---|---|---|---|---|---|---|---|---|
| Deposited cluster | CdTe | | | | CdTe | | | |
| Deposition energy | 1 eV | 10 eV | 20 eV | 40 eV | 1 eV | 10 eV | 20 eV | 40 eV |
| Reflect | 2.6±0.4 | 6.7±0.7 | 6.3±0.7 | 5.6±0.6 | 0.4±0.2 | 2.9±0.5 | 6.4±0.8 | 6.9±0.8 |
| Sputter | 0.1±0.1 | 3.6±0.5 | 12.1±0.9 | 28.1±1.2 | 0.±0. | 0.6±0.2 | 2.±0.4 | 9.4±0.9 |
| Sit on | 89.±0.8 | 13.6±0.9 | 2.9±0.4 | 0.6±0.2 | 43.3±1.5 | 7.9±0.8 | 4.4±0.6 | 2.±0.4 |
| Penetrate | 0.±0. | 3.9±0.5 | 13.7±0.9 | 21.7±1.1 | 0.±0. | 15.6±1.1 | 23.4±1.3 | 33.4±1.5 |
| Join 1st layer | 0.2±0.1 | 18.9±1. | 12.6±0.9 | 3.1±0.5 | 4.7±0.7 | 3.8±0.6 | 3.3±0.6 | 1.9±0.4 |
| Dissociate | 7.8±0.7 | 20.±1.1 | 10.6±0.8 | 1.9±0.4 | 47.8±1.5 | 33.1±1.5 | 18.±1.2 | 5.1±0.7 |
| Replace | 0.3±0.1 | 33.2±1.3 | 41.9±1.3 | 38.9±1.3 | 3.9±0.6 | 36.2±1.5 | 42.6±1.5 | 41.3±1.5 |

| | (111) Cd-terminated surface | | | | (111) Te-terminated surface | | | |
|---|---|---|---|---|---|---|---|---|
| Deposited cluster | CdTe | | | | CdTe | | | |
| Deposition energy | 1 eV | 10 eV | 20 eV | 40 eV | 1 eV | 10 eV | 20 eV | 40 eV |
| Reflect | 76.5±1.3 | 48.4±1.5 | 20.7±1.2 | 11.1±0.9 | 0.5±0.2 | 3.2±0.5 | 5.9±0.7 | 9.4±0.9 |
| Sputter | 0.±0. | 1.5±0.4 | 12.3±1. | 20.6±1.2 | 0.±0. | 0.4±0.2 | 1.6±0.4 | 4.9±0.7 |
| Sit on | 23.1±1.3 | 18.6±1.2 | 6.5±0.7 | 0.5±0.2 | 99.5±0.2 | 57.6±1.5 | 17.3±1.1 | 7.5±0.8 |
| Penetrate | 0.±0. | 0.2±0.1 | 4.±0.6 | 9.3±0.9 | 0.±0. | 0.5±0.2 | 3.4±0.5 | 10.6±0.9 |
| Join 1st layer | 0.±0. | 0.±0. | 0.±0. | 0.±0. | 0.±0. | 0.±0. | 0.±0. | 0.±0. |
| Dissociate | 0.4±0.2 | 14.8±1.1 | 19.1±1.2 | 9.5±0.9 | 0.±0. | 26.4±1.3 | 33.8±1.4 | 15.5±1.1 |
| Replace | 0.±0. | 16.5±1.1 | 37.3±1.5 | 49.±1.5 | 0.±0. | 11.9±1. | 38.±1.5 | 52.±1.5 |

# Appendix C

# Post-Annealing Defect Analysis Data

Defect analysis data for Te-terminated dimerised (100) surface post-annealing process mentioned in Chapter 7 is presented here. We have three system to anneal at 500 K, 600 K and 650 K, respectively. We count the number of atoms, off-site atoms, vacancies, interstitials and antisites in each double-layer, namely the original surface double-layer ('+0' in the table), the complete first new double-layer ('+1' in the table), the incomplete second new double-layer ('+2' in the table) and the incomplete third new double-layer ('+3' in the table). Note that there are 144 atoms in each double-layer for a perfect lattice.

| Deposition Energy | | 0.1 eV | | | | | 1 eV | | | | | 10 eV | | | | |
|---|---|---|---|---|---|---|---|---|---|---|---|---|---|---|---|---|
| Which Double-Layer / Number of Atoms/Defects | | +0 | +1 | +2 | +3 | Total | +0 | +1 | +2 | +3 | Total | +0 | +1 | +2 | +3 | Total |
| Before Annealing | Atoms | 152 | 131 | 99 | 20 | 402 | 145 | 144 | 103 | 17 | 409 | 145 | 143 | 103 | 6 | 397 |
| | Off-Sites | 9 | 85 | 90 | 19 | 203 | 3 | 94 | 93 | 16 | 206 | 2 | 59 | 81 | 6 | 148 |
| | Vacancies | 1 | 76 | 125 | 137 | 339 | 2 | 63 | 112 | 137 | 314 | 0 | 43 | 106 | 141 | 290 |
| | Interstitials | 2 | 70 | 79 | 14 | 165 | 0 | 65 | 71 | 11 | 147 | 1 | 43 | 64 | 3 | 111 |
| | Antisites | 0 | 21 | 11 | 6 | 38 | 0 | 30 | 23 | 6 | 59 | 1 | 15 | 18 | 3 | 37 |
| Anneal at 500 K | Atoms | 150 | 138 | 96 | 18 | 402 | 147 | 144 | 99 | 19 | 409 | 148 | 141 | 103 | 5 | 397 |
| | Off-Sites | 6 | 75 | 84 | 14 | 179 | 5 | 79 | 80 | 17 | 181 | 6 | 42 | 84 | 5 | 137 |
| | Vacancies | 0 | 62 | 122 | 140 | 324 | 2 | 53 | 107 | 136 | 298 | 1 | 33 | 111 | 143 | 288 |
| | Interstitials | 3 | 57 | 78 | 12 | 150 | 1 | 58 | 61 | 11 | 131 | 3 | 32 | 70 | 4 | 109 |
| | Antisites | 0 | 18 | 9 | 2 | 29 | 0 | 23 | 21 | 6 | 50 | 1 | 12 | 14 | 1 | 28 |
| Anneal at 600 K | Atoms | 150 | 135 | 111 | 6 | 402 | 145 | 144 | 104 | 16 | 409 | 147 | 144 | 98 | 8 | 397 |
| | Off-Sites | 6 | 52 | 76 | 6 | 140 | 3 | 42 | 81 | 16 | 142 | 5 | 27 | 48 | 5 | 85 |
| | Vacancies | 0 | 41 | 98 | 143 | 282 | 1 | 24 | 103 | 142 | 270 | 1 | 14 | 84 | 137 | 236 |
| | Interstitials | 1 | 37 | 65 | 5 | 108 | 0 | 28 | 61 | 14 | 103 | 2 | 16 | 37 | 2 | 57 |
| | Antisites | 0 | 19 | 12 | 1 | 32 | 0 | 17 | 20 | 2 | 39 | 1 | 13 | 10 | 4 | 28 |
| Anneal at 650 K | Atoms | 148 | 134 | 103 | 17 | 402 | 146 | 140 | 106 | 17 | 409 | 145 | 143 | 97 | 12 | 397 |
| | Off-Sites | 4 | 43 | 69 | 15 | 131 | 2 | 53 | 66 | 13 | 134 | 2 | 35 | 57 | 8 | 102 |
| | Vacancies | 0 | 41 | 97 | 138 | 276 | 0 | 37 | 93 | 139 | 269 | 0 | 24 | 89 | 137 | 250 |
| | Interstitials | 1 | 35 | 56 | 10 | 102 | 1 | 35 | 55 | 11 | 102 | 0 | 24 | 42 | 5 | 71 |
| | Antisites | 0 | 11 | 13 | 5 | 29 | 0 | 19 | 11 | 2 | 32 | 1 | 12 | 14 | 4 | 31 |

# References


[1] Wikipedia. Greenhouse gas. Accessed date, February 2015. http://en.wikipedia.org/wiki/Greenhouse_gas. (Cit. on p. 1)

[2] Wikipedia. Global warming. Accessed date, February 2015. http://en.wikipedia.org/wiki/Global_warming. (Cit. on p. 1)

[3] DECC. Energy trends: June 2014. *Energy Trends*, June 2014. https://www.gov.uk/government/publications/energy-trends-june-2014. (Cit. on p. 1)

[4] H. Spanggaard and F.C. Krebs. A brief history of the development of organic and polymeric photovoltaics. *Solar Energy Materials and Solar Cells*, 2004. (Cit. on p. 1)

[5] EPIA. Global market outlook for photovoltaics 2014-2018. *Global Market Outlook for Photovoltaics*, June 2014. http://www.epia.org/fileadmin/user_upload/Publications/EPIA_Global_Market_Outlook_for_Photovoltaics_2014-2018_-_Medium_Res.pdf. (Cit. on p. 1)

[6] G. Di Marco and L. Palmisano. Thin-Film Photovoltaics. *International Journal of Photoenergy*, **2010**:1–2, 2010. (Cit. on p. 1, 97)

[7] W. Shockley and H.J. Queisser. Detailed Balance Limit of Efficiency of p-n Junction Solar Cells. *Journal of Applied Physics*, **32**[3]:510–519, 1961. (Cit. on p. 2, 3, 57)

[8] M.A. Green. Radiative efficiency of state-of-the-art photovoltaic cells. *Progress in Photovoltaics: Research and Applications*, **20**[4]:472–476, September 2011. (Cit. on p. 2, 3, 57)

[9] J.Y.W. Seto. The electrical properties of polycrystalline silicon films. *Journal of Applied Physics*, **46**[12]:5247–5254, 1975. (Cit. on p. 2, 57, 97)

[10] Wikipedia. Thin film. Accessed date, September 2014. `http://en.wikipedia.org/wiki/Thin_film`. (Cit. on p. 2)

[11] Wikipedia. Solar cell. Accessed date, September 2014. `http://en.wikipedia.org/wiki/Solar_cell`. (Cit. on p. 3)

[12] NREL. Research cell efficiency records, September 2014. `http://www.nrel.gov/ncpv/`. (Cit. on p. 4, 139)

[13] First Solar. First Solar builds the highest efficiency thin film PV cell on record, August 2014. `http://investor.firstsolar.com/releasedetail.cfm?releaseid=864426`. (Cit. on p. 3)

[14] Fraunhofer ISE. ISE photovoltaics report: July 28, 2014. *Photovoltaics Report*, July 2014. `http://www.ise.fraunhofer.de/en/downloads-englisch/pdf-files-englisch/photovoltaics-report-slides.pdf`. (Cit. on p. 3)

[15] Wikipedia. Shockley-queisser limit. Accessed date, February 2015. `http://en.wikipedia.org/wiki/ShockleyQueisser_limit`. (Cit. on p. 3)

[16] Solar Systems & Equipment. The CdTe solar cell. Accessed date, September 2014. `http://www.solar-sse.com/cts.htm`. (Cit. on p. 5)

[17] NREL. Polycrystalline thin films. Accessed date, September 2014. `http://www.nrel.gov/pv/thinfilm.html`. (Cit. on p. 5)

[18] J.M. Walls. Department of Electrical Engineering, Loughborough University, Leicestershire, U.K. private commun. (Cit. on p. 6, 97, 98)

[19] C. Li, J. Poplawsky, Y. Wu, A.R. Lupini, A. Mouti, D.N. Leonard, N. Paudel, K. Jones, W. Yin, M. Al-Jassim, Y. Yan, and S.J. Pennycook. From atomic structure to photovoltaic properties in CdTe solar cells. *Ultramicroscopy*, **134**[C]:113–125, November 2013. (Cit. on p. 7)

[20] D.M. Dobkin and M.K. Zuraw. *Principles of Chemical Vapor Deposition*. What's Going on Inside the Reactor. Springer Science & Business Media, 2003. (Cit. on p. 5)

[21] R.A. Fischer. *Precursor Chemistry of Advanced Materials*. CVD, ALD and Nanoparticles. Springer, September 2005. (Cit. on p. 5)

[22] D. Monsma and J. Becker. The Savannah ALD System - An Excellent Tool for Atomic Layer Deposition. *Material Matters*, **1**:5, 2006. (Cit. on p. 5)

[23] S.K. Young. Sol-Gel Science for Ceramic Materials. *Material Matters*, **1**:8, 2006. (Cit. on p. 8)

[24] F. Caruso. *Colloids and Colloid Assemblies: Synthesis, Modification, Organization and Utilization of Colloid Particles*. John Wiley & Sons, 2006. (Cit. on p. 8)

[25] L.C. Klein. *Sol-gel technology for thin films, fibers, Preforms, Electronics, and Specialty Shapes*. Noyes Publications, 1988. (Cit. on p. 8)

[26] A.C. Pierre. *Introduction to Sol-Gel Processing*. Springer Science & Business Media, 1998. (Cit. on p. 8)

[27] V.P. Balema. Chemical Deposition Techniques in Materials Design. *Material Matters*, **1**:3, 2006. (Cit. on p. 8)

[28] AZoNano. Bubblers and Cylinders for CVD/ALD Precursor Handling, January 2014. `http://www.azonano.com/article.aspx?ArticleID=3423`. (Cit. on p. 9)

[29] F.H. Nicoll. The Use of Close Spacing in Chemical-Transport Systems for Growing Epitaxial Layers of Semiconductors. *Journal of The Electrochemical Society*, **110**[11]:1165–1167, November 1963. (Cit. on p. 9)

[30] R.C. Jaeger. Introduction to Microelectronic Fabrication. Prentice Hall, 2002. (Cit. on p. 9)

[31] S.M. Sze. *Semiconductor devices, physics and technology*. John Wiley & Sons Inc, April 1985. (Cit. on p. 9)

[32] D.B. Chrisey and G.K. Hubler. *Pulsed Laser Deposition of Thin Films*. Wiley-Interscience, June 1994. (Cit. on p. 9)

[33] M. Ohring. *Materials Science of Thin Films*. Academic Press, October 2001. (Cit. on p. 9)

[34] B. Wolf. *Handbook of Ion Sources*. CRC Press, August 1995. (Cit. on p. 9)

[35] W.A. Pinheiro, V.D. Falcão, L.R.d.O. Cruz, and C.L. Ferreira. Comparative study of CdTe sources used for deposition of CdTe thin films by close spaced sublimation technique. *Materials Research*, **9**[1]:47–49, 2006. (Cit. on p. 10)

[36] P.J. Kelly and R.D. Arnell. Magnetron sputtering: a review of recent developments and applications. *Vacuum*, **56**[3]:159–172, March 2000. (Cit. on p. 9)

[37] P.S. McLeod and L.D. Hartsough. High-rate sputtering of aluminum for metallization of integrated circuits. *Journal of Vacuum Science and Technology*, **14**[1]:263–265, January 1977. (Cit. on p. 9)

[38] R.K. Waits. Planar magnetron sputtering. *Journal of Vacuum Science and Technology*, **15**[2]:179–187, March 1978. (Cit. on p. 9)

[39] Euclid Techlabs. Thick film ceramic/dielectric sputtering metallization technology. Accessed date, October 2014. `http://www.euclidtechlabs.com/product/sputtering.php`. (Cit. on p. 11)

[40] LAMMPS. Lammps molecular dynamics simulator. Accessed date, August 2014. `http://lammps.sandia.gov/`. (Cit. on p. 12, 16)

[41] S. Plimpton. Fast Parallel Algorithms for Short-Range Molecular Dynamics. *Journal of Computational Physics*, 1995. (Cit. on p. 12, 16)

[42] L.J. Vernon. Modelling Growth of Rutile TiO2. *PhD thesis*, 2010. (Cit. on p. 12, 36, 44)

[43] A.D. Compaan, A. Gupta, S. Lee, S. Wang, and J. Drayton. High efficiency, magnetron sputtered CdS/CdTe solar cells. *Solar Energy*, 2004. (Cit. on p. 15)

[44] S.N. Alamri. The growth of CdTe thin film by close space sublimation system. *physica status solidi (a)*, **200**[2]:352–360, December 2003. (Cit. on p. 15)

[45] W.C. Swope, H.C. Andersen, P.H. Berens, and K.R. Wilson. A computer simulation method for the calculation of equilibrium constants for the formation of physical clusters of molecules: Application to small water clusters. *The Journal of Chemical Physics*, **76**[1]:637–649, January 1982. (Cit. on p. 15)

[46] H.M. Urbassek. Molecular-dynamics simulation of sputtering. *Nuclear Inst. and Methods in Physics Research, B*, **122**[3]:427–441, 1997. (Cit. on p. 16)

[47] A. Nakano, R.K. Kalia, and P. Vashishta. Growth of pore interfaces and roughness of fracture surfaces in porous silica: Million particle molecular-dynamics simulations. *Physical Review Letters*, 1994. (Cit. on p. 16)

[48] W. Cheong and L.C. Zhang. Molecular dynamics simulation of phase transformations in silicon monocrystals due to nano-indentation. *Nanotechnology*, **11**[3]:173–180, September 2000. (Cit. on p. 16)

[49] W.J. Hehre. Ab initio molecular orbital theory. *Accounts of Chemical Research*, **9**[11]:399–406, November 1976. (Cit. on p. 16)

[50] F.H. Stillinger and T.A. Weber. Computer simulation of local order in condensed phases of silicon. *Physical Review B*, **31**[8]:5262–5271, April 1985. (Cit. on p. 17)

[51] R. Biswas and D. Hamann. New classical models for silicon structural energies. *Physical Review B*, **36**[12]:6434–6445, October 1987. (Cit. on p. 18)

[52] J. Tersoff. New empirical approach for the structure and energy of covalent systems. *Physical Review B*, **37**[12]:6991, 1988. (Cit. on p. 18)

[53] J. Tersoff. Empirical interatomic potential for silicon with improved elastic properties. *Physical Review B*, **38**:9902–9905, 1988. (Cit. on p. 18)

[54] D.K. Ward, X.W. Zhou, B.M. Wong, F.P. Doty, and J.A. Zimmerman. Accuracy of existing atomic potentials for the CdTe semiconductor compound. *The Journal of Chemical Physics*, **134**[24]:244703, 2011. (Cit. on p. 20)

[55] D.G. Pettifor and I.I. Oleinik. Analytic bond-order potentials beyond Tersoff-Brenner. I. Theory. *Physical Review B*, **59**[13]:8487, 1999. (Cit. on p. 20, 21, 22)

[56] I.I. Oleinik and D.G. Pettifor. Analytic bond-order potentials beyond Tersoff-Brenner. II. Application to the hydrocarbons. *Physical Review B*, **59**[13]:8500, 1999. (Cit. on p. 20)

[57] D.K. Ward, X.W. Zhou, B.M. Wong, F.P. Doty, and J.A. Zimmerman. Analytical bond-order potential for the cadmium telluride binary system. *Physical Review B*, **85**[11]:115206, March 2012. (Cit. on p. 20, 22, 24, 60, 61, 62)

[58] D.G. Pettifor, M.W. Finnis, D. Nguyen-Manh, D.A. Murdick, X.W. Zhou, and H.N.G. Wadley. Analytic bond-order potentials for multicomponent systems. *Materials Science and Engineering: A*, **365**[1-2]:2–13, January 2004. (Cit. on p. 20)

[59] L. Goodwin, A.J. Skinner, and D.G. Pettifor. Generating Transferable Tight-Binding Parameters: Application to Silicon. *EPL (Europhysics Letters)*, **9**[7]:701–706, August 1989. (Cit. on p. 21)

[60] C.H.L. Goodman. Bonding in Cadmium Telluride. *Proceedings of the Physical Society*, **74**[4]:489, October 1959. (Cit. on p. 24)

[61] H.J.C. Berendsen, J.P.M. Postma, W.F. van Gunsteren, A. DiNola, and J.R. Haak. Molecular dynamics with coupling to an external bath. *The Journal of Chemical Physics*, **81**[8]:3684, 1984. (Cit. on p. 27, 70)

[62] M.R. Hestenes and E. Stiefel. Methods of conjugate gradients for solving linear systems. *Journal of Research of the National Bureau of Standards*, **49**:409–436 (1953), 1952. (Cit. on p. 28)

[63] T.A. Straeter. On the extension of the davidon-broyden class of rank one, quasi-newton minimization methods to an infinite dimensional hilbert space with applications to optimal control problems. *PhD thesis*, September 1971. (Cit. on p. 28)

[64] R. Fletcher and C.M. Reeves. Function minimization by conjugate gradients. *The computer journal*, **7**[2]:149–154, January 1964. (Cit. on p. 28)

[65] E. Polak and G. Ribiere. Note sur la convergence de méthodes de directions conjuguées. *Rev. Française Informat. Recherche Opérationnelle*, **3**[16]:35–43, 1969. (Cit. on p. 28)

[66] R.H. Byrd, P. Lu, J. Nocedal, and C.Y. Zhu. A limited memory algorithm for bound constrained optimization. *SIAM Journal on Scientific Computing*, **16**[5]:1190–1208, 1995. (Cit. on p. 29)

[67] J.L. Morales and J. Nocedal. Remark on "algorithm 778: L-BFGS-B: Fortran subroutines for large-scale bound constrained optimization". *ACM Transactions on Mathematical Software (TOMS)*, **38**[1]:7–4, November 2011. (Cit. on p. 29)

[68] SciPy.org. scipy.optimize.fmin_l_bfgs_b. Accessed date, August 2014. `http://docs.scipy.org/doc/scipy/reference/generated/scipy.optimize.fmin_l_bfgs_b.html`. (Cit. on p. 30)

[69] POVRay.org. Pov-ray - the persistence of vision raytracer. Accessed date, June 2015. `http://www.povray.org/`. (Cit. on p. 30)

[70] A.F. Voter, F. Montalenti, and T.C. Germann. Extending the time scale in atomistic simulation of materials. *Annual Review of Materials Research*, **32**[1]:321–346, 2002. (Cit. on p. 30, 33, 35)

[71] A. Voter. Hyperdynamics: Accelerated Molecular Dynamics of Infrequent Events. *Physical Review Letters*, **78**[20]:3908–3911, May 1997. (Cit. on p. 33)

[72] A. Voter. Parallel replica method for dynamics of infrequent events. *Physical Review B*, **57**[22]:R13985–R13988, June 1998. (Cit. on p. 33)

[73] M.R. Sorensen and A.F. Voter. Temperature-accelerated dynamics for simulation of infrequent events. *The Journal of Chemical Physics*, **112**[21]:9599–9606, June 2000. (Cit. on p. 33)

[74] Z.Q. Wang, D. Stroud, and A.J. Markworth. Monte Carlo study of the liquid CdTe surface. *Physical Review B*, **40**[5]:3129, 1989. (Cit. on p. 33)

[75] K.A. Fichthorn and W.H. Weinberg. Theoretical foundations of dynamical Monte Carlo simulations. *The Journal of Chemical Physics*, **95**[2]:1090–1096, July 1991. (Cit. on p. 33)

[76] P. Pechukas. Transition state theory. *Annual Review of Physical Chemistry*, 1981. (Cit. on p. 35)

[77] A.F. Voter and J.D. Doll. Transition state theory description of surface self-diffusion: Comparison with classical trajectory results. *The Journal of Chemical Physics*, **80**[11]:5832–5838, June 1984. (Cit. on p. 35)

[78] G. Henkelman and H. Jónsson. Long time scale kinetic Monte Carlo simulations without lattice approximation and predefined event table. *The Journal of Chemical Physics*, **115**[21]:9657, 2001. (Cit. on p. 38)

[79] G. Henkelman and H. Jónsson. A dimer method for finding saddle points on high dimensional potential surfaces using only first derivatives. *The Journal of Chemical Physics*, **111**[15]:7010, 1999. (Cit. on p. 41, 42)

[80] G.T. Barkema and N. Mousseau. Event-based relaxation of continuous disordered systems. *Physical Review Letters*, **77**[21]:4358–4361, 1996. (Cit. on p. 42)

[81] G.T. Barkema and N. Mousseau. Identification of relaxation and diffusion mechanisms in amorphous silicon. *Physical Review Letters*, **81**[9]:1865–1868, 1998. (Cit. on p. 42)

[82] N. Mousseau and G.T. Barkema. Activated mechanisms in amorphous silicon: An activation-relaxation-technique study. *Physical Review B*, **61**[3]:1898, 2000. (Cit. on p. 42)

[83] E. Cancès, F. Legoll, M.C. Marinica, K. Minoukadeh, and F. Willaime. Some improvements of the activation-relaxation technique method for finding transition pathways on potential energy surfaces. *The Journal of Chemical Physics*, **130**[11]:114711, 2009. (Cit. on p. 42)

[84] C.J. Cerjan and W.H. Miller. On finding transition states. *The Journal of Chemical Physics*, 1981. (Cit. on p. 45)

[85] A. Pedersen, S.F. Hafstein, and H. Jónsson. Efficient sampling of saddle points with the minimum-mode following method. *SIAM Journal on Scientific Computing*, **33**[2]:633–652, 2011. (Cit. on p. 45)

[86] T. Lazauskas. Simulating Radiation Effects in Iron with Embedded Oxide Nanoparticles. *PhD thesis*, pages 1–197, 2014. (Cit. on p. 46, 54, 55, 134)

[87] Wikipedia. Lanczos algorithm. Accessed date, August 2014. `http://en.wikipedia.org/wiki/Lanczos_algorithm`. (Cit. on p. 46)

[88] C.C. Paige. Computational variants of the Lanczos method for the eigenproblem. *Journal of the Institute of Mathematics and its Applications*, **10**:373–381, 1972. (Cit. on p. 46)

[89] B.N. Parlett and D.S. Scott. The Lanczos algorithm with selective orthogonalization. *Mathematics of computation*, **33**[145]:217–238, 1979. (Cit. on p. 46)

[90] H. Jnsson, G. Mills, and K.W. Jacobsen. *Classical and Quantum Dynamics in Condensed Phase Simulations*, chapter Nudged Elastic Band Method for Finding Minimum Energy Paths of Transitions, pages 385–404. World Scientific, June 1998. (Cit. on p. 47)

[91] G. Henkelman, B.P. Uberuaga, and H. Jónsson. A climbing image nudged elastic band method for finding saddle points and minimum energy paths. *The Journal of Chemical Physics*, **113**:9901, 2000. (Cit. on p. 47)

[92] G. Henkelman and H. Jónsson. Improved tangent estimate in the nudged elastic band method for finding minimum energy paths and saddle points. *The Journal of Chemical Physics*, **113**:9978, 2000. (Cit. on p. 47, 48)

[93] W. E, W. Ren, and E. Vanden-Eijnden. String method for the study of rare events. *Physical Review B*, **66**[5]:052301, August 2002. (Cit. on p. 50)

[94] B. Peters, A. Heyden, A.T. Bell, and A. Chakraborty. A growing string method for determining transition states: Comparison to the nudged elastic band and string methods. *The Journal of Chemical Physics*, **120**[17]:7877, 2004. (Cit. on p. 50, 51)

[95] W. E, W. Ren, and E. Vanden-Eijnden. Simplified and improved string method for computing the minimum energy paths in barrier-crossing events. *The Journal of Chemical Physics*, **126**[16]:164103, 2007. (Cit. on p. 50)

[96] F. El-Mellouhi, N. Mousseau, and L. Lewis. Kinetic activation-relaxation technique: An off-lattice self-learning kinetic Monte Carlo algorithm. *Physical Review B*, **78**[15]:153202, October 2008. (Cit. on p. 54)

[97] B.D. McKay. Practical graph isomorphism. In *Proceedings of the Tenth Manitoba Conference on Numerical Mathematics and Computing, Vol. I (Winnipeg, Man., 1980)*, pages 45–87, 1981. (Cit. on p. 54)

[98] B.D. McKay. Nauty user's guide (version 2.4). *Computer Science Dept*, 2007. (Cit. on p. 54)

[99] Wikipedia. Cadmium telluride. Accessed date, August 2014. `http://en.wikipedia.org/wiki/Cadmium_telluride`. (Cit. on p. 57)

[100] Wikipedia. Cadmium telluride photovoltaics. Accessed date, August 2014. `http://en.wikipedia.org/wiki/Cadmium_telluride_photovoltaics`. (Cit. on p. 57)

[101] A.R. Barron and C. Smith. Crystal Structure. *OpenStax-CNX*, **16927**:1–18, January 2010. (Cit. on p. 58)

[102] F. Pietrucci, G. Gerra, and W. Andreoni. CdTe surfaces: Characterizing dynamical processes with first-principles metadynamics. *Applied Physics Letters*, **97**[14]:141914, 2010. (Cit. on p. 58, 117)

[103] J.D.H. Donnay and H.M. Ondik. *Crystal data : determinative tables*. US Department of Commerce, National Bureau of Standards and Joint Committee on Powder Diffraction Standards, Washington DC, 3rd edition, 1973. (Cit. on p. 60, 62)

[104] M.J. Mehl, B.M. Klein, and D.A. Papaconstantopoulos. First principles calculations of elastic properties of metals. *Intermetalic Compounds: Principles and Practice*, **1**, 1994. (Cit. on p. 60)

[105] S.Q. Wang and H.Q. Ye. Ab initio elastic constants for the lonsdaleite phases of C, Si and Ge. *Journal of Physics: Condensed Matter*, **15**[30]:5307–5314, 2003. (Cit. on p. 60)

[106] J.M. Rowe, R.M. Nicklow, D.L. Price, and K. Zanio. Lattice dynamics of cadmium telluride. *Physical Review B*, **10**[2]:671, July 1974. (Cit. on p. 61)

[107] B.K. Agrawal and S. Agrawal. Ab initio calculation of the electronic, structural, and dynamical properties of AlAs and CdTe. *Physical Review B*, **45**[15]:8321, April 1992. (Cit. on p. 61)

[108] R.D.S. Yadava, R.K. Bagai, and W.N. Borle. Theory of te precipitation and related effects in CdTe Crystals. *Journal of electronic materials*, **21**[10]:1001–1016, October 1992. (Cit. on p. 61)

[109] C. Szeles. Advances in the crystal growth and device fabrication technology of CdZnTe room temperature radiation detectors. *Nuclear Science, IEEE Transactions on*, **51**[3]:1242–1249, June 2004. (Cit. on p. 61)

[110] S. Zhang and J. Northrup. Chemical potential dependence of defect formation energies in GaAs: Application to Ga self-diffusion. *Physical Review Letters*, **67**[17]:2339–2342, October 1991. (Cit. on p. 61)

[111] J. Northrup and S. Zhang. Dopant and defect energetics: Si in GaAs. *Physical Review B*, **47**[11]:6791–6794, March 1993. (Cit. on p. 61)

[112] L. Vernon, S.D. Kenny, R. Smith, and E. Sanville. Growth mechanisms for TiO2 at its rutile (110) surface. *Physical Review B*, **83**[7]:075412, February 2011. (Cit. on p. 69)

[113] L.J. Vernon, R. Smith, and S.D. Kenny. Modelling of deposition processes on the TiO2 rutile (110) surface. *Nuclear Inst. and Methods in Physics Research, B*, **267**[18]:3022–3024, September 2009. (Cit. on p. 69)

[114] C. Ferekides. Department of Electrical Engineering, University of South Florida, Tampa, U.S.A. private commun. (Cit. on p. 76)

[115] L.K. Béland, P. Brommer, F. El-Mellouhi, J.F. Joly, and N. Mousseau. Kinetic activation-relaxation technique. *Physical Review E*, **84**[4]:046704, October 2011. (Cit. on p. 83, 84)

[116] K.A. Fichthorn and Y. Lin. A local superbasin kinetic Monte Carlo method. *The Journal of Chemical Physics*, **138**[16]:164104, 2013. (Cit. on p. 83, 85)

[117] B. Puchala, M.L. Falk, and K. Garikipati. An energy basin finding algorithm for kinetic Monte Carlo acceleration. *The Journal of Chemical Physics*, **132**[13]:134104, 2010. (Cit. on p. 83)

[118] J.H. Greenberg. P-T-X phase equilibrium and vapor pressure scanning of non-stoichiometry in CdTe. *Journal of crystal growth*, **161**[1-4]:1–11, 1996. (Cit. on p. 97)

[119] C. Ferekides. Thin film CdTe photovoltaics: Past, present and future. presentation, University of South Florida, USA, September 2014. (Cit. on p. 97)

[120] S. Blackwell. Modelling thin film growth over realistic time scales. *PhD thesis*, 2012. (Cit. on p. 100, 115)

[121] H. Defdqed. Molecular Dynamics Simulations of Dimer Opening on a Diamond {001}(2x1) Surface. *Science*, 1992. (Cit. on p. 117)

[122] C.D.J. Scott. A computational study of surface topography arising from energetic particle interactions. *PhD thesis*, 2012. (Cit. on p. 134)